THE FLORIDA STATE UNIVERSITY

FAMU–FSU COLLEGE OF ENGINEERING

MODELING, SIMULATION AND EXPERIMENTAL VALIDATION OF POLYMER ELECTROLYTE MEMBRANE FUEL CELLS AND ALKALINE MEMBRANE FUEL CELLS

By

LAUBER DE SOUZA MARTINS

A Dissertation submitted to the
Department of Mechanical Engineering
in partial fulfillment of the
requirements for the degree of
Doctor of Philosophy

Degree Awarded:
Spring Semester, 2012

Lauber de Souza Martins defended this dissertation on March 19, 2012.

The members of the supervisory committee were:

Juan Carlos Ordonez
Professor Directing Dissertation

Jose Viriato Coelho Vargas
Professor Co-Directing Dissertation

Hui Li
University Representative

Farrukh Alvi
Committee Member

Carl A. Moore
Committee Member

The Graduate School has verified and approved the above-named committee members, and certifies that the dissertation has been approved in accordance with university requirements.

I dedicate this dissertation to

God, my lovely family. My father Laercio, my mother Marlete and my sister Taline.

ACKNOWLEDGEMENTS

“You have to have a dream! Without a dream people perish. Dreams... the gentle, fragile, whispering, touching, enduring, awesome stuff hope is made of, it's the gift of God to every fainting heart!" – Gloria Gaither.

To God be all the glory and praise for my accomplishment. I thank God for being with me all the way during this journey. I believe that nothing happens by chance and I am sure God put special people along the way to help me to make my dream become true.

I thank my family, my father Laercio Martins, for the words of support and encouragement; always making me look forward reminding me that the journey would be long but the battles would be won one by one, one at a time. I thank my mother Marlete Martins for the words of advice, support and comfort, always available to listen to my concerns in moments of uncertainty, reminding me that God is always in control and to Him should go our burdens in prayer. Thanks to my sister Taline, who during all these years was worried about my well being and health. I thank her for her prayers and for her care for my parents.

I thank my high school chemistry teacher, Valeria Zuana, who for the first time explained to me what means to be a Ph.D. and what steps are necessary to take to become one. From that moment on, that was my dream, to be a Ph.D. I would like to thank two more teachers that always supported me in my dream of being a scientist; a special thanks to Janete Gizzi and Maria Alice, my first Physics and English teacher, respectively.

I thank Dr. George Stanescu, who first introduced me to Thermodynamics. He gave me the chance to work in small research projects that later would be published in congresses for mechanical engineering undergraduate students. That experience made me passionate about research.

Under recommendation of Dr. George Stanescu, Dr. Jose Viriato Coelho Vargas accepted me as his undergraduate research assistant. A special thanks for the recommendation and a special thanks to Dr. Vargas whom I have been working for since 1998. I assure that the long hours spent in discussions during all those years have not been in vain, discussions not only about science, but also, relationships and personal issues. I thank him for always believing that I would finish this long race and his personal oat of walking with the students until the finish line. Thank you!

I thank Dr. Juan Ordonez for his advices, words of support and patience during these long years. Dr. Ordonez was always supportive and understanding to my needs, a great lesson

that I bring from him is that a research group should be a team ready to help any of its members, when the primary activity of a member could put aside for a moment to help a teammate, what would promote growth (academic and personal) for both. Thank you!

Dr. Jeferson Avila de Souza and Dr. Alejandro Rivera are my very good friends that were not directly related to my research but were always there to guide me and to give me support; to them, my gratitude.

I also would like to thank all my graduate students friends that helped me along the journey of taking classes and preliminary exams. In special, Mohd Yousuf Ali, Tyler Thomas, Han Zhao, Hang Wen. A very special thanks to Elise Sommer who during the months prior to my defense worked hard by my side helping me with the research, what made her not only a co-worker but very dear friend.

My appreciation for the support given to me from the Center for Advanced Power Systems and its staff, specially Nancy Rainey, Joann Jirak, Steve Ranner, Bianca Trociewitz and Michael Coleman.

I thank the members of my dissertation committee, Dr. Farrukh Alvi, Dr. Carl Moore, Dr. Hui Li, Dr. Juan Ordonez, and Dr. José Vargas for giving me their kind support, expertise, time and recommendations.

I would also like to thank others who have been sources of support, advice and encouragement. I thank Dr. Leon Van Dommelen, Dr. William Oates and Dr. Emmanuel Collins.

TABLE OF CONTENTS

LIST OF TABLES

LIST OF FIGURES

NOMENCLATURE

A	area, m^2
A_c	total gas channel cross-section area, m^2
A_s	unit fuel cell cross-section area, m^2
$\tilde{A}$	dimensionless area
AFC	alkaline fuel cell
AMFC	alkaline membrane fuel cell
B	dimensionless constant [67]
c	specific heat, kJ kg^{-1} K^{-1}
c_p	specific heat at constant pressure, kJ $kg^{-1}K^{-1}$
C	constant, Eq (2.12)
CV	control volume
D	Knudsen diffusion coefficient, m^2s^{-1}
D_h	gas channel hydraulic diameter, m
f	friction factor
F	Faraday constant, 96,500 Ceq^{-1}
h	heat transfer coefficient, W $m^{-2}K^{-1}$
$\tilde{h}$	dimensionless heat transfer coeficient
$H_i(T_i)$	molar enthalpy of formation at temperature T_i of reactants and products, kJ $kmol^{-1}$ of compound i
$\tilde{H}_i(\theta_i)$	dimensionless molar enthalpy of formation at dimensionless temperature θ_i of reactants and products
$i_{o,a}, i_{o,c}$	exchange current densities, A m^{-2}

$i_{Lim,a}, i_{Lim,c}$ limiting current densities, A m^{-2}

I current, A

$\tilde{I}$ dimensionles current

j mass flux, kg m^2 s^{-1}

k thermal conductivity, W $m^{-1}K^{-1}$

K permeability

KOH potassium hydroxyde

$\tilde{k}$ dimensionless thermal conductivity

L control volume length, m

L_c, L_t gas channels internal dimensions as shown in Fig. 1, m

L_x, L_y, L_z fuel cell length, width and height, respectively, m

m mass, kg

$\dot{m}$ mass flow rate, kg s^{-1}

M molar weight, kg $kmol^{-1}$

n equivalent electron per mole of reactant, eq mol^{-1}

$\dot{n}$ molar flow rate, kmol s^{-1}

n_c number of parallel ducts in gas channel

N dimensionless global wall heat trasnfer coefficient

p pressure, N m^{-2}

$\tilde{p}_s$ perimeter of cross-section, m

P dimensionless pressure

PEMFC polymer electrolyte membrane fuel cell

Pr Prandtl number, $\mu c_p / k$

q	tortuosity
Q	reaction quotient
$\dot{Q}$	heat transfer rate, W
$\tilde{Q}$	dimensionless heat transfer rate
r	pore radius, m
R	ideal gas constant, kJ $kg^{-1}K^{-1}$
$\bar{R}$	universal gas constant, 8.314 kJ $kmol^{-1}K^{-1}$
Re_{Dh}	Reynolds number based on D_h, $uD_h\rho/\mu$
S	dimensionless conversion factor, Eq. (2.41)
T	temperature, K
u	mean velocity, ms^{-1}
$\tilde{u}$	dimensionless mean velocity
U	global wall heat transfer coefficient, W $m^{-2}K^{-1}$
U_a	uncertainty of quantity a
V	electrical potential, V
V	volume, m^3
V_T	total volume, m^3
W	weight, N
W	electrical work, J
$\tilde{W}$	dimensionless fuel cell total electrical power
$\tilde{W}_{net}$	dimensionless fuel cell net power
$\tilde{W}_p$	dimensionless required pumping power
x	axial direction, Fig. 1

$[\cdot]$	molar concentration of a substance, mol l^{-1}

Greek Symbols

α_a, α_c	anode and cathode charge transfer coefficients
β	electrical resistance, Ω
δ	gas channel aspect ratio
ε	standard deviation
ΔG	molar Gibbs free energy change, kJ $kmol^{-1}$
$\Delta \tilde{G}$	dimensionless molar Gibbs free energy change
ΔH	molar enthalpy change, kJ $kmol^{-1}H_2$
$\Delta \tilde{H}$	dimensionless molar enthapy change
ΔS	molar entropy change, kJ $kmol^{-1}$
ΔT	temperature change, K
ζ	stoichiometric ratio
η	potential loss, V
η_a, η_c	anode and cathode charge transfer overpotentials, V
$\eta_{d,a}, \eta_{d,c}$	anode and cathode mass diffusion overpotentials, V
η_i	ideal efficiency or maximum theoretical efficiency
η_I	first law efficiency
η_{II}	second law efficiency
η_{net}	net law efficiency

$\tilde{\eta}_a, \tilde{\eta}_c$	dimensionless anode and cathode charge transfer overpotentials
$\tilde{\eta}_{d,a}, \tilde{\eta}_{d,c}$	dimensionless anode and cathode mass diffusion overpotentials
$\tilde{\eta}_{ohm}$	dimensionless fuel cell total ohmic potential loss
θ	dimensionless temperature
λ	ionomer water content
μ	viscosity, kg m^{-1} s^{-1}
υ_i	reaction coefficient
ξ	dimensionless length
ρ	density, kg m^{-3}
σ	electrical conductivity, Ω^{-1} m^{-1}
ϕ	porosity
ψ	dimensionless mass flow rate

Subscripts

a	anode
(aq)	aqueous solution
c	cathode or channel
dry	dry
e	reversible
f	fuel
(g)	gaseous phase
H^+	hydrogen cation
H_2	hydrogen

H_2O	water
i	irreversible
i,a	irreversible at the anode
i,c	irreversible at the cathode
in	control volume inlet
j	particular dimension of fuel cell geometry
load	adjustable electrical load
(l)	liquid phase
memb	electrolyte membrane (solid and liquid parts)
ohm	ohmic
out	control volume outlet
ox	oxidant
O_2	oxygen
p	polymer electroyte membrane
pap	chromatograhpy paper
ref	reference level
s,a	anode solid side
s,c	cathode solid side
sol	solution
t	thickness of the wall of gas channels
w	wall
wet	wetted
0	initial condition
1,...,7	control volume, Fig. 2.1
12	interaction between CV1 and CV2

23	interaction between CV2 and CV3
34	interaction between CV3 and CV4
45	interaction between CV4 and CV5
56	interaction between CV5 and CV6
67	interaction between CV6 and CV7
∞	ambient

Superscript

$\circ$	standard conditions [gases at 1 atm, 25ºC, species in solution at 1 M, where M is the molarity = (moles solute)/(liters solution)]
~	dimensionless varialbe

ABSTRACT

Fuel cell technology is currently a promising alternative for clean energy production due to its high efficiency and minimum environmental impact. A new design and optimization are a natural alternative to reduce cost and make fuel cells increasingly more attractive for power generation. In order to predict the response of fuel cells according to the variation of manufacturing materials, internal structure and external shape, physical properties, operating and design parameters, a reliable simulation model (and computationally fast) is necessary. A simplified and comprehensive mathematical model for a polymer electrolyte membrane fuel cell (PEMFC) is developed and experimentally validated. The computed polarization and power curves are directly compared to the experimentally measured data with good qualitative and quantitative agreement. A mathematical model for a single Alkaline Membrane Fuel Cell (AMFC) with square section and fixed volume is introduced. The model is based on electrochemical principles, conservation of mass, momentum, energy and species; also based on pressure drop in the gas channels and gradient of temperature with respect to space in the flow direction. The pressure drop caused by the gas supply induces considerable power conumption as the operating current increases. Therefore, it must be taken in consideration in fuel cell design. The simulation results comprise temperature, net power, polarization curves and gas channels pressure drop. The computed temperature, polarization and power curves for AMFC are directly compared to the experimentally measured (using a prototype built in laboratory) with good qualitative and quantitative agreement. The model allows the existing trade-offs that determine the internal structure (geometry) aiming minimum thermodynamic losses be investigated. The spatial dependence was obtained knowing the position of the control volume in the fuel cell. Hence, the solution was obtained solivng a system of algebraic equation instead a system of partial differential equations, which would demand higher computational time. Therefore, the model is expected to be a useful tool for PEMFC and AMFC design and optimization.

CHAPTER ONE

INTRODUCTION

Nowadays fuel cell technology is well advanced, with applications in stationary power generation and in vehicles [1-4]. Political efforts to reduce greenhouse gases in the road transport sector are basically in conflict with the ever growing demand for transport services; emissions from internal combustion (IC) engines in the automotive application have already been subject to increasingly tougher statutory limits for quite some time [5].

In recent years, considerable funds and research resources have been invested in developing the fuel cell as a source of electrical energy to power vehicles, simultaneously to achieve the requirements of significant reduction of engine CO_2 emissions and pollutant emission free operation [6,7].

As a promising technology that may successfully supersede the combustion of fossil fuel as the dominant method of energy conversion, hydrogen fuel cells are studied worldwide with an aim to improve the power output, lower the cost and extend the life of operation for widespread applications [8]. Fuel cells are expected to be of practical use because they emit less environmental pollutant and convert more efficiently from chemical energy to electrical energy than other energy resources; especially, polymer electrolyte membrane fuel cell (PEMFC) is expected to be the driving power of vehicles and stationary power supply, because it can work at low temperature and has high power density [9,10].

No other energy generation technology offers the combination of benefits that fuel cells do. In addition to low or zero emissions, benefits include high efficiency, multi-fuel capability, sitting flexibility, durability, and ease of maintenance. Fuel cells are also scalable and can be stacked until the desired power output is reached. Since fuel cells operate silently, they reduce noise pollution as well as air pollution and the waste heat from a fuel cell can be used to provide hot water or space heating for a home or office.

Technically and economically, there are still many hurdles to be overcome in fuel cell development before wide spread application. Modeling and computational simulation in one, two and three dimensions have been developed in academia and industry to assess the effect of materials, geometric and operating design on fuel cell response [9-20]. The results show that

issues as high cost of materials, durability, water management and thermodynamic losses are still far from being appropriately solved.

In order to be competitive economically with other existing power and vehicular systems, the industry needs an efficient methodology for the determination of the optimal project for maximum performance according to desired specifications (e.g., efficiency, power, environmental control). In the context of search for improvement, thermodynamic optimization is one way of lowering costs, associated with performance improvement [10].

In sum, currently, design methodologies seek to find a desirable condition from a group of candidates arbitrarily selected. This study is therefore motivated by the need to develop a methodology that provides a structured process to synthesize fuel cell optimal thermodynamic configurations directly from the physical laws.

In this work a mathematical model is introduced for the single PEMFC and alkaline membrane fuel cell (AMFC), which divides the fuel cell into several control volumes that correspond to the most representative parts of the flow system. All the flow phenomena that are present are taken into account. The result is a model with unidirectional internal flow that contains additional three-dimensional features such as the electrode wetted area, heat transfer between the cell, fuel, oxidant and the surroundings, and pressure drops in the gas channels. The model is simple enough to ensure small computational time requirements, so that it is possible to predict the response of the single fuel cells according to variations of the material physical properties, and operating and design parameters.

1.1 Research Objectives

The main objective of this research is to develop and to validate a reliable model of PEMFC and AMFC that is computationally fast to predict their response to variations of physical properties of the materials, operating and design parameters. The model accounts for pressure drop in the gas channels, all major electrochemical and thermal interactions considering temperature gradient with respect to space in the flow direction and current increase. The computed polarization curves of the PEMFC and AMFC will be directly compared to the experimental results. A commercial PEMFC and an operational prototype of an AMFC built at laboratory scale using membranes made by cellulose (chromatography paper) and potassium hydroxide solution (KOH) as electrolyte will be used to validate and adjust the mathematical

model making possible its future use as a tool for the design of new fuel cells and the optimization of operating fuel cells.

1.2 Literature Review

What defines whether a mathematical modeling is good or bad is its application, so the area of interest has to be determined before start modeling. The modeling of fuel cells can focus on a single fuel cell (gas channels, electrode and membrane), stacks, or on an integrated system where the fuel cell is just one of the components [11].

Rowe and Li investigated various design and operating conditions or a proton exchange membrane fuel cell, modeling thermal response and water management, including membrane hydration, phase change of water in the electrodes with unsaturated reactant gas streams. They concluded that the temperatures distribution is affected by the water phase change in the electrode and that operation on reformed fuel results in a decrease in the performance, since it reduces membrane hydration [12].

Wang *et al.* in 2004, investigated the cathode catalyst layer of an PEMFC considering the kinetics of oxygen reduction, at the catalyst/electrolyte interface, proton transport through the polymer electrolyte network, the oxygen diffusion through gas pore, and the dissolved oxygen diffusion through electrolyte. They concluded that the thickness and the size of the agglomerate should be kept as small as possible to minimize the adverse effects of mass transport at high current density. The thickness and position of the catalyst layer (rather is close to gas diffusion layer or to the membrane) depend on the oxygen diffusion and the proton conductivity. If the oxygen diffusion is very limited relative to the current density, the active region of the catalyst layer may be confined to a narrow region of the catalyst layer close to the gas diffusion layer. If the proton conductivity is the limiting factor, the active part of the catalyst layer may be confined to a narrow region near the membrane side of the catalyst layer associated with a higher effective overpotential [13].

In the same year, Ferguson and Ugursal developed a steady-state model of a PEM cogeneration fuel cell system. The objective was to do integrate the model to existing simulation tools in order to size fuel cells systems for houses and predict their performance. The proposed model was capable of estimating the electricity production, fuel use and cogeneration heat recovery of the fuel cell in response to conditions in the building [14].

Biyikoglu presented the state of the art of fuel cell modeling. He introduced and briefly explained the PEMFC components and its functions. According to Biyikoglu, until 2005, there was no complete computational model for fuel cell stacks including all the phenomena together and the available experimental data and mathematical models have been obtained for restricted and idealizes situations, contemplating just the phenomena investigated. His conclusions point out that future research should focus on the performance and integration of fuel cell stacks and associated sub-systems including fuel storage, reforming and processing, air delivery systems, heat exchangers and thermal integration, humidification and water management, DC power processing, sensor and control [15].

In 2006 Manne *et al.* studied the applications of Buttler-Volmer equations in the modeling of activation polarization of PEMFC. Since many publications use the Buttler-Volmer equations without determination of its applicability, they conducted a study which conclusion is a some recommendations regarding the applicability of those equations [16].

Yan and Wu proposed a model for prediction of the local mass diffusion of a sinlgel catalyst particle in the cathode catalyst layer. The catalyst particle is treated as many small platinum particles (1–10.0 nm) embedded in the larger carbon particle support (30–100 nm). This assembly is surrounded by an ionomer film with thickness ranging from 0.5 nm to 10.0 nm. The modeling results confirm that the platinum particle size, platinum loading and ionomer thickness can each play an important role on local mass and charge transport in the PEM fuel cell catalyst particle agglomerate. The local spherical diffusion, reactant distribution and electrochemical kinetics are strongly influenced by particle size, platinum loading and ionomer thickness. The modeling results show that the better Nafion thickness is not more than 1 nm around the catalyst particle, i.e. no more than 40 wt% [17].

In 2009, Baschuk and Li presented a mathematical model for a isothermal, steady state, two dimensional PEMFC, where the transport of water and hydronium in the polymeric membrane and the transport of electrical current in the solid was included. They concluded that the convective gas velocity facilitates hydrogen transport trough the anode but inhibits oxygen transport. They also show that the water produced at the cathode is not enough to be used at the anode, so the gas needs to be humidified [18].

The alkaline fuel cell has been described since 1902, but just in 1940s F.T. Bacon demonstrated that this type of fuel cell can be a viable power unit. Two units were used, each weighing 113kg, to provide the electrical power, and much of the potable water, for the craft

that took man to the moon, however PEMFC has been used in the first NASA manned aircraft [19].

Figure 1.1: Fuel cell from the Apollo spacecraft. [19].

Alkaline Fuel Cells (AFC) have interesting features as compared to PEMFC, such as lower cost electrolyte (KOH aqueous solution) and mainly, the possibility of using non-noble catalysts (e.g., nickel, silver), since faster kinetics of the reactions is observed in alkaline media than in acid media [3, 4,23,24]. Nickel can be an alternative as a catalyst at the anode instead of Platinum as we can see in Table 1.1 [20,25]; which represents a good advantage when cost is an important issue [26]. Additionally, AFC can work at higher temperatures (100–120 ^{o}C) than PEMFC, which cannot operate above 90 ^{o}C due to the need to hydrate the nafion membrane [22]. The cathode activation overvoltage in an AFC is less than in a PEMFC, at similar temperatures. Unfortunately the reasons why are still poorly understood [27]. The Table 1.2 shows some of the advantages and disadvantages of alkaline fuel cells.

Table 1.1: Standard state (T = 300K, 1 atm) exchange current densities for hydrogen oxidation reaction on various metal surfaces [20,25].

Catalyst	**Electrolyte**	i_0 **[A/cm^2]**
Pt	Acid	10^{-3}
Pt	Alkaline	10^{-4}
Ni	Acid	10^{-5}
Ni	Alkaline	10^{-4}

Recently, a lot of effort is being applied to find new materials and catalyst for the electrodes of the fuel cells in order to improve the kinetics of the electrochemical reaction and make them affordable and competitive regarding to cost of manufacturing. Materials for the membrane have been also investigated since they also play an important role in transport losses [23,28-43].

Table 1.2: Advantages and disadvantages of an alkaline fuel cell

Advantages	**Disadvantages**
• Inexpensive catalysts: - Nickel at the anode - Silver at the cathode • No expensive polymer membrane is necessary – liquid alkaline solution as electrolyte • Liquid electrolyte may enable a simple cooling of the stack • Activation overvoltage is less than with an acid electrolyte	• High corrosivity of the electrolye • Electrolyte must be reconcentrated during long time • Intolerance to CO_2 $CO_2 + 2OH^- \rightarrow CO_3^{2-} + H_2O$ • Must use pure H_2 and O_2

Carbon dioxide poisoning can be a crucial issue when talking about using potassium hydroxide as electrolyte for AFC. Potassium hydroxide reacts with the carbon dioxide that might exist in the air-operated alkaline fuel cell, resulting in a decrease in the fuel cell output, since the electrolyte would not be used as an ionic conductor but a reactant for an unexpected reaction. This reaction has the effect of reducing the number of hydroxyl ions available for reaction at the electrodes, also reducing the ionic conductivity of the electrolyte solution, and could block the pores of the gas diffusion layer (GDL) by the precipitation of K_2CO_3 salt, but

not causing any degradation of the electrodes [44]. As a result, the AFC performance is greatly reduced in air breathing systems, i.e., when the oxidant is air which contains CO_2. For this reason, alkaline fuel cells typically operate on pure oxygen, or at least purified air, and must have built-in mechanisms to clean out as much of the carbon dioxide as is possible.

Because the generation and storage requirements of oxygen make pure-oxygen AFCs expensive, the active development of the technology has not attracted large industrial interest. Although the harmful effects of carbon dioxide poisoning can be partly reduced by several different strategies [22], a permanent solution would increase the possibility of AFC commercialization; however, some publications were released about carbon dioxide tolerance of alkaline fuel cells [37, 45-48].

Shin *et al* conducted a study about the characteristics of Hydrogen oxidation on Raney nickel electrode with carbon black in an alkaline fuel cell, in which was shown that the use of this electrode increased the limiting current density for hydrogen oxidation and the diffusivity of hydroxide ions [49].

Bdaulf *et al* investgated Nickel foam as a potential electrode substrate for alkaline fuel cell electrode because its lower cost compared to nickel mesh. Lower ohmic and charge transfer resistance was obtained in tests made on silver plated nickel foam ($7.9 \times 10^{-2}\Omega$) compared with uncoated nickel foam ($9.3 \times 10^{-2}\ \Omega$). The silver coating enhanced the catalytic activity of the uncoated nickel foam towards the oxygen reaction. The conclusion was that silver plating leads to an increase in the surface roughness of the nickel foam [31]. The Fig. 1.2 shows SEM of Ni foam surfaces.

Stoica *et al* [28] and Sollogub *et al* [29] conducted a study where a polymer electrolyte was prepared and characterized. The measured ionic conductivity was superior to 10^{-2} Scm^{-1}. These studies show the feasibility of an alkaline fuel cell using solid polymeric electrolyte instead a liquid solution electrolyte. The maximum power and current obtained were 100 mW/cm^2 and 270 mA/cm^2, respectively. The catalyst content of the electrodes used is 0.17 mg Pt/cm^2 [29].

Park *et al* conducted an study where various anion exchange membrane were prepared to find out the best configuration for solid alkaline fuel cells operation, which have higher OH^- conductivity and thermal property where the possibility of using non-precious catalyst at cathode was taken in consideration. The ionic conductivity was enhanced when a mixture of mono and diamine and the diamine with longer alkyl chain. The referred anion exchange membrane, when used with Ag/C (at cathode) had results comparable with that using Pt/C. Using electrodes with 0.5 mg/cm^2 Pt/C at the anode and 2.0 mg/cm^2 Ag/C at the cathode,

results comparable to one with 0.5 mg/cm^2 Pt/C at the anode and cathode when using an membrane made of chloromethylation and amination of polysulfone were obtained. The maximum power and current were 28-30 mW/cm^2 and 130 mA/cm^2, respectively [30].

.

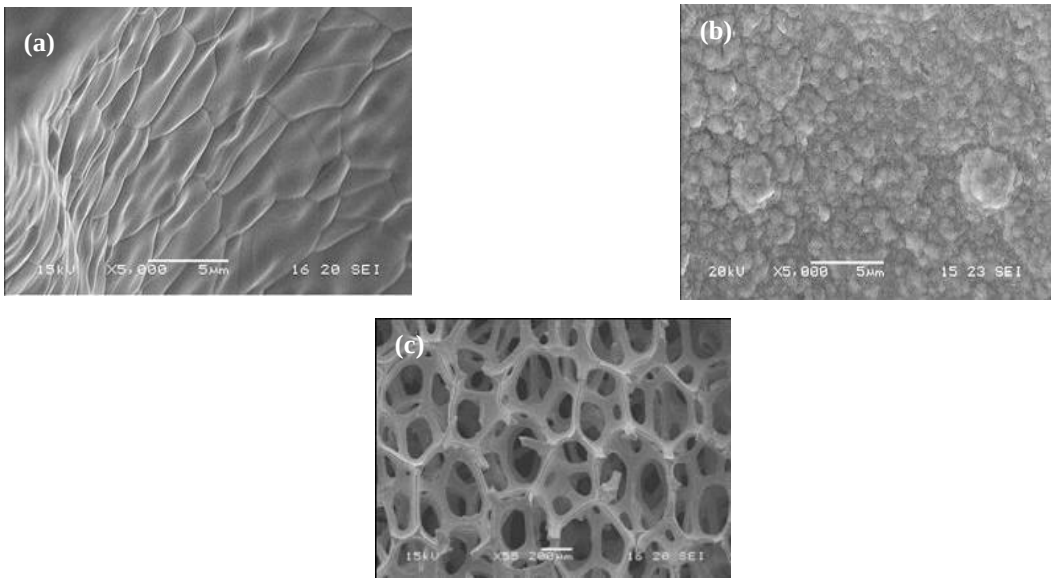

Figure 1.2: Scanning electron microscope (SEM) pictures: (a) the Ni foam surface, (b) the Ni foam surface after silver plating (Silver loading: 11 mg/cm^2), (c) open structure of nickel foam [31].

Ying Wan *et al* studied the performance of a solid polymer electrolyte composite membranes using Chitosan and KOH used as the function ionic source. They tested the membrane in a alkaline fuel cell using electrode which the catalyst content is 1 mg/cm^2 Pt/C. The maximum current obtained was 35 mA/cm^2 [32].

Alkaline fuel cells can be classified according to how the electrolyte is confined between the electrodes.

a) Mobile electrolyte

In this configuration the electrolyte is a liquid solution of KOH, that must be pumped through the fuel cell. Due to continuous flow of a liquid through the fuel cell, it is also a way to cool down the fuel cell and remove the water generated by the electrochemical reaction. The water produced by the fuel cell from the chemical reactions makes the concentration of the solution to decrease; while two mols of water are formed at the anode, just one mol is consumed at the cathode, so the concentration of the solution decreases; what would make the

performance of the fuel cell decrease as well. As a solution for this problem, a control system for the concentration must be design in order to keep it constant during operation time.

b) Static electrolyte

The first case of static electrolyte alkaline fuel cell is the one similar to mobile electrolyte, where the electrolyte is also a liquid solution, but at this time the solution is not pumped but restrained within the porous of a solid material (membrane), in other words, the membrane is soaked with the solution. The membrane is then placed between the electrodes.

Differently of the case above, the second type of static electrolyte fuel cells are those that run using a solid electrolyte. In this case, there is no liquid solution between the electrodes; the membrane allows the migration of the ions from one electrode to the other. It is called Anion Exchange Membrane (AEM). Anion Exchange Membrane is a polymeric material that allows anions to move through its chemical chains. In this research we will focus on the fist kind of static electrolyte, where the electrolyte is kept confined in the porous of the membrane made by cellulose (Fig 1.3). The two possible configurations of alkaline fuel cells are shown in the Fig. 1.4.

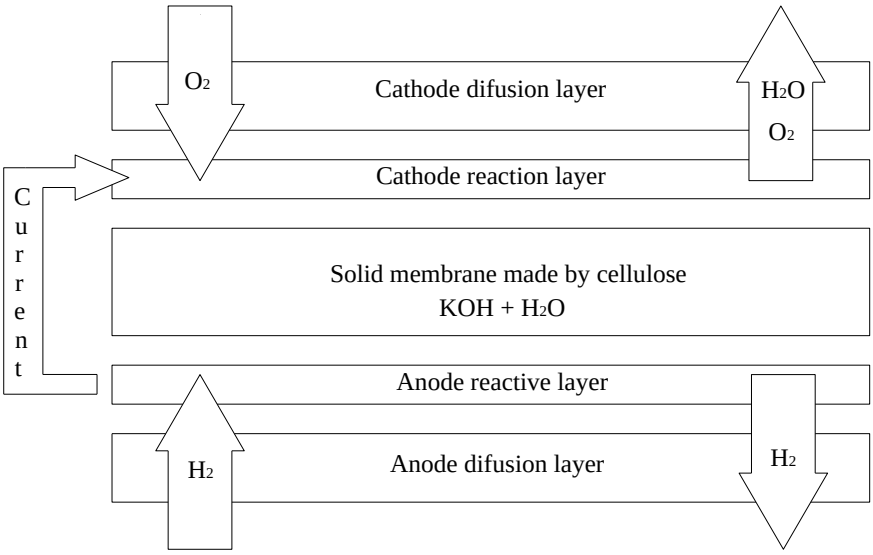

Figure 1.3: Schematic of a single alkaline fuel cell.

Considering static electrolyte cells, the use of asbestos or ammonium-based membranes for commercial applications also bring additional restrictions, based on ammonia potential hazardous effects, such as acute toxicity [50] and Immediately Dangerous to Life or Health

(IDLH) levels [51], and on asbestos being a known carcinogenic agent [52]. Therefore, recently a cellulose-based alkaline membrane fuel cell was proposed by our group [53].

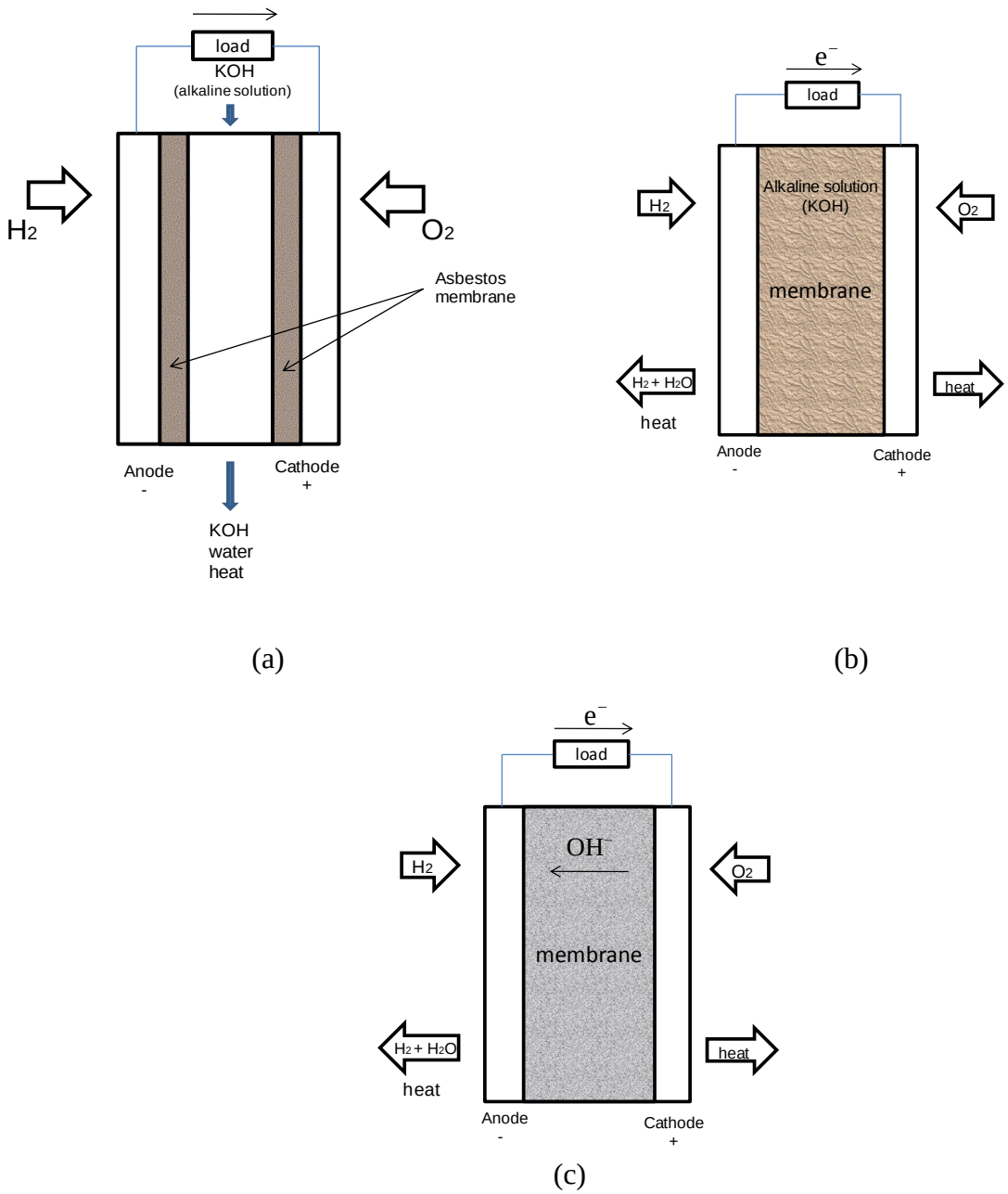

Figure 1.4: Types of Alkaline fuel cells: (a) Mobile electrolyte, (b) and (c) Static electrolyte.

Although promising experimental results were obtained in the laboratory, design and operating parameters need to be optimized for maximum performance, so that a proper assessment can be made for possible future commercialization. For that, mathematical modeling and computational simulation is recommended in order to predict how fuel cell

performance is affected by the variation of operating and geometric parameters [54]. It is also important that the mathematical model accounts for temperature spatial gradients and gas channels pressure drops [54, 55] which significantly affect fuel cell performance. Such desired model features should not lead to the understanding that the more complex the better the model will be. On the contrary, when the model is considered for fuel cell structure optimization, a large number of different configurations tests are needed, then it is desirable for the model to be simple, computationally fast and still able to capture reliably the fuel cell behavior [55,56].

Though very useful refined information can be extracted from spatially dependent models, the two- and three-dimensional models are not suitable for the optimization of flow geometry, because they would require the solving of partial differential equations for flow simulation in a very large number of flow configurations.

Proton exchange membrane fuel cells (PEMFC) and solid oxide fuel cells (SOFCs) are considered the most promising candidates for commercial exploitation, and much attention has been given toward system modeling, including the fluid flows that supply the cells with fuel and oxidant, with the use of computational fluid dynamics (CFD), as pointed out by Young [57] and Ma et al. [58], that recently reviewed the status of three-dimensional fuel cell modeling. On the other hand, there are few previous studies concerning AFC modeling and simulation. Verhaert et al. [59] presented a steady state AFC thermodynamic model without the consideration of possible temperature variation within the cell using a control volume approach, which was validated by experimental data for future fuel cell stack development; Duerr et al. [60] used an isothermal dynamic electrochemical model to predict the effect of several parameters on an AFC stack response during load change events; Mohan and Shrestha [61] investigated the effect of four different electrolyte concentrations and three different anode flow rates on AFC performance experimentally and with an isothermal steady state model, concluding that performance increased as electrolyte concentration increased, and deduced statistically from modeling and statistical analysis optimal electrolyte concentration and anode flow rate for maximum performance, and Weydahl et al. [62] introduced an isothermal, one-dimensional transient model of a porous oxygen electrode in an alkaline medium based on mass balances and flooded-agglomerate theory in order to study time constants, the combined effects of fast potential propagation and slow oxygen diffusion targeting the dynamic improvement of the AFC cathodes without sacrifice of a steady-state response.

In the next chapter we will present the thermodynamic model of Polymer electrolyte fuel cells and alkaline fuel cells. Since we use the same approach to model both fuel cells we

decided to present them in parallel so the difference between both models will be easily discern.

CHAPTER TWO

THERMAL MODELING OF A POLYMER ELECTROLYTE MEMBRANE FUEL CELL (PEMFC) AND ALKALINE MEMBRANE FUEL CELL (AMFC)

The thermal modeling of the fuel cells was done relating steady state thermodynamic and electrochemical model with efficiency, we will expose the details of the model in the following sections.

The fuel cell is divided into seven control volumes that interact energetically with one another. The fuel cells also interact with adjacent fuel cells in a package, and or with the ambient. Additionally, two bipolar plates (interconnects) are presented: these have the function of allowing the electrons produced by the electrochemical oxidation reaction at the anode to flow to the external circuit or to an adjacent cell.

The model consists of the conservation equations for each control volume, and equations accounting for electrochemical reactions, where they are present. The reversible electrical potential and power of the fuel cell are then computed as functions of the temperature and pressure fields determined by the model. The actual electrical potential and power of the fuel cell are obtained by subtracting from the reversible potential the losses due to surface overpotentials (poor electrocatalysis), slow diffusion and all internal ohmic losses through the cell (resistance of individual cell components, including electrolyte layer, interconnects and any other cell components through which electrons flow). These are functions of the total cell current (I), which is directly related to the external load (or the cell voltage); in sum, the total cell current is considered an independent variable in this study. The present analysis is for a steady state fuel cell operation.

2.1 Polymer Electrolyte Membrane Fuel Cell Model

A schematic diagram of the internal structure of a PEMFC is shown in Fig. 2.1. The fuel considered in the analysis is pure hydrogen, but it is possible to use a diluted hydrogen mixture generated from a hydrocarbon reformation process when running a PEMFC. Although pure oxygen is assumed in the analysis, air could be used as the oxidant in the experimental

validation of PEMFC, provided that enough O_2 is supplied to the cell to meet the amount of oxygen required by the hydrogen supplied to the cell for a complete reaction.

The control volumes (CV) are fuel channel (CV1), the anode diffusion-backing layer (CV2), the anode reaction layer (CV3), the polymer electrolyte membrane (CV4), the cathode reaction layer (CV5), the cathode diffusion backing layer (CV6) and the oxidant channel (CV7).

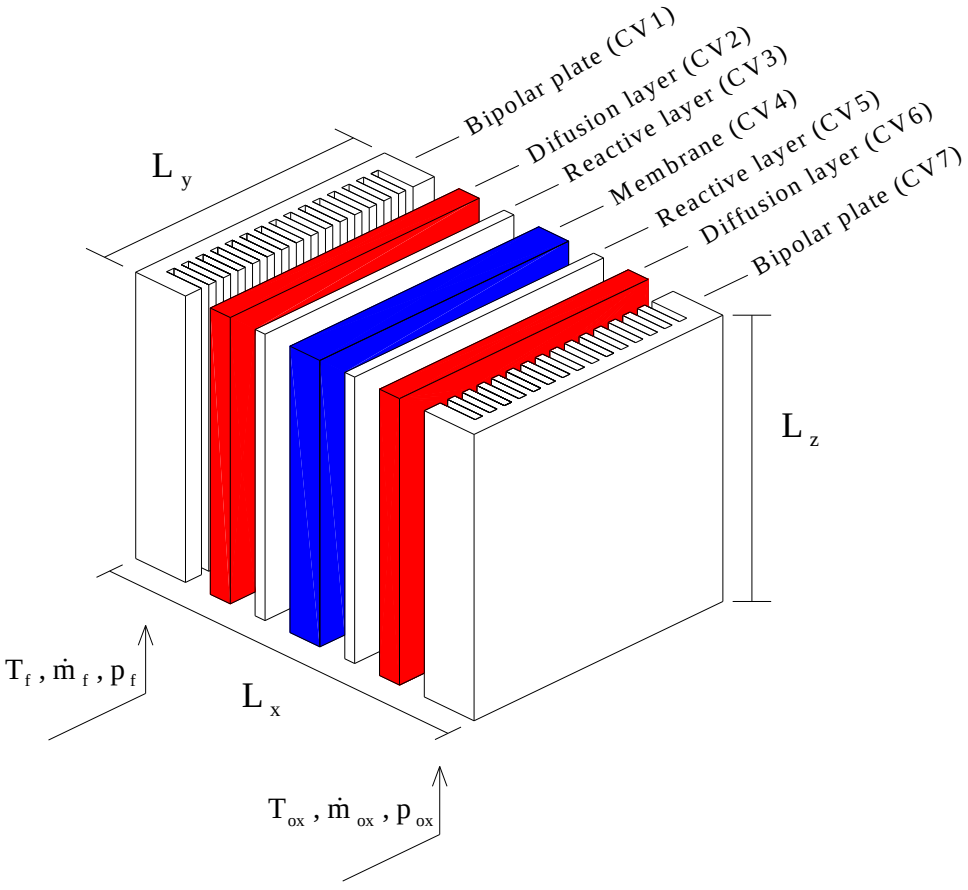

Figure 2.1: Control volume distribution of a single fuel cell unit (PEMFC). The fuel channels (CV1), the anode diffusion layer (CV2), the anode reaction layer (CV3), polymer electrolyte membrane (CV4), the cathode reaction layer (CV5), the cathode diffusion layer (CV6) and the oxidant channel (CV7).

2.1.1 Dimensionless Variables

Dimensionless variables are defined based on the geometric and operating parameters of the system. Dimensionless pressures and temperatures are referenced to ambient conditions $(T_\infty \text{ and } P_\infty)$, $P_i = p_i/p_\infty$ and $\theta_i = T_i/T_\infty$, where subscript i indicates a substance or a location in the fuel cell, P is the dimensionless pressure, p the pressure, Nm^{-2}; θ the dimensionless temperature, T the temperature, K. Other dimensionless variables are defined as:

$$\psi_i = \frac{\dot{m}_i}{\dot{m}_{ref}} \tag{2.1}$$

$$N_i = \frac{U_{wi} V_T^{2/3}}{\dot{m}_{ref} c_{p,f}}, \quad \tilde{A}_i = \frac{A_i}{V_T^{2/3}} \tag{2.2}$$

where i indicates a substance or location in the fuel cell, ψ_i is the dimensionless mass flow rate, $\dot{m}$ the mass flow rate, kg s^{-1}; $\dot{m}_{ref}$ the reference mass flow rate, kg s^{-1}. N the dimensionless global wall heat transfer coefficient; U_w the global wall heat transfer coefficient, $Wm^{-2} K^{-1}$; V_T the total volume of the fuel cell, m^3; $c_{p,f}$ the specific heat at constant pressure of the fuel, kJ $kg^{-1} K^{-1}$; $\tilde{A}$ the dimensionless area and A is the area, m^2.

The fixed length scale $V_T^{1/3}$ is used for the purpose of non-dimensionalizing all the lengths that characterize the fuel cell geometry.

$$\xi_j = \frac{L_j}{V_T^{1/3}} \tag{2.3}$$

where the subscript j indicates a particular dimension of the fuel cell geometry; ξ is the dimensionless length and L the length, m.

Dimensionless heat transfer coefficient $(\tilde{h})$ and thermal conductivity $(\tilde{k})$ are defined as follows:

$$\tilde{h} = \frac{hV_T^{2/3}}{\dot{m}_{ref} c_{p,f}}, \quad \tilde{k} = \frac{kV_T^{1/3}}{\dot{m}_{ref} c_{p,f}} \tag{2.4}$$

where h is the heat transfer coefficient, W m^{-2} K^{-1}; and $\tilde{k}$ is the dimensionless thermal conductivity.

The physics of the fuel cell is described by taking into account the mass conservation and the first law of thermodynamics at each CV. The electrochemical reactions at CV3 and CV5 differ depending on the type of the fuel cell. In this study we will consider PEMFC and AMFC (Chapter 4).

2.1.2 Mass Balance

The Fig. 2.2 shows the upper view of the control volumes of PEMFC. The anode is comprised by the CV2 and CV3 and the cathode is comprised by the CV5 and CV6.

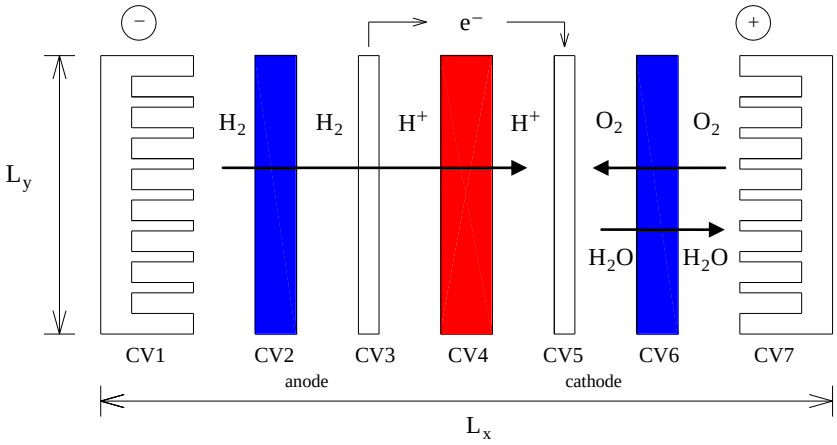

Figure 2.2: Upper view of the control volumes of a single PEMFC.

The hydrogen mass flow rate required for the current (I) dictated by the external load is

$$\dot{m}_{H_2} = \dot{n}_{H_2} M_{H_2} = \frac{I}{nF} M_{H_2} \tag{2.5}$$

Therefore, the oxygen mass flow rate needed for both fuel cells (PEMFC and AMFC) is:

$$\dot{m}_{O_2} = \frac{1}{2}\dot{n}_{H_2} M_{O_2} \tag{2.6}$$

where $\dot{n}$ is the molar flow rate, kmol s^{-1} and M the molar weight, kg $kmol^{-1}$; n the equivalent electron per mole of reactant,$eqmol^{-1}$; I the total current, A; F the Faraday constant, Ceq^{-1}.

2.1.3 Energy Conservation Analysis

The wall heat transfer area of one control volume is $A_{wi} = \tilde{p}_s L_i \quad (2 \le i \le 6)$ and $A_{wi} \cong \tilde{p}_s L_i + L_y L_z$ (i = 1,7; assuming that $L_t << L_c$ in Fig. 2.3), where $\tilde{p}_s = 2(L_y + L_z)$ is the perimeter of the fuel cell cross-section.

The control volumes are $V_j = L_y L_z L_j \quad (2 \le j \le 6)$ and $V_j = n_c L_c L_l L_z$ (j =1, 7), where n_c is the integer part of $L_y/(L_t + L_c)$, i.e., the number of parallel ducts in each gas channel (fuel and oxidant).

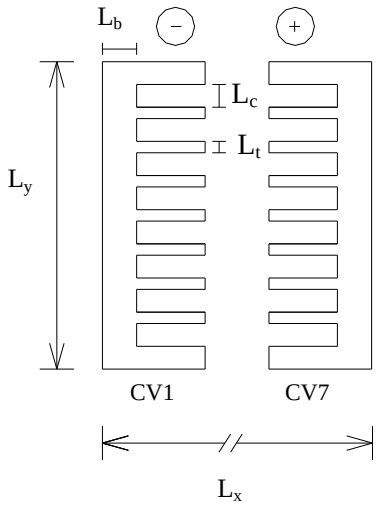

Figure 2.3: Internal dimensions of gas channels (CV1 and CV7).

The fuel pressure (p_f in CV1) and oxidant pressure (p_{ox} in CV7) are assumed known and constant during fuel cell operation. The stoichiometric ratio for an electrode reaction is defined as the provided reactant (mol s^{-1}) divided by the reactant needed for the electrochemical reaction of interest. The fuel enters the fuel cell through the CV1 and the oxidant through the

CV7, as shown in Fig.2.1. The mass and energy balances for CV1 yield the temperature in CV1.

$$\tilde{Q}_{w1} + \psi_f(\theta_f - \theta_1) + \tilde{Q}_{12} + \tilde{Q}_{1ohm} = 0 \tag{2.7}$$

where

$$\tilde{Q}_{wi} = N_i \tilde{A}_{wi}(1-\theta_i),\ \tilde{Q}_{iohm} = I^2 \beta_i \big/ \left(\dot{m}_{ref} c_{p,f} T_\infty\right) \tag{2.8}$$

where $\tilde{Q}_{12} = \tilde{h}_1 \tilde{A}_s (1-\phi_2)(\theta_2 - \theta_1)$, $\tilde{A}_s = L_y L_z \big/ V_T^{2/3}$. Where β is the electrical resistance, Ω; ϕ_i the porosity and $\tilde{A}_s$ the dimensionless cross-section area of the fuel cell. Subscript i represents a location in the cell, i.e., a particular CV.

The dimensionless heat transfer rates for all the compartments are $\tilde{Q}_i = \dot{Q}_i \big/ \dot{m}_{ref} c_{p,f} T_\infty$. The subscript i accounts for any of the heat transfer interactions that are present in the model.

Assuming that the channels are straight and sufficiently slender, the pressure drop in the channels is calculated using the ideal gas model as follows:

$$\Delta P_i = n_c f_i \left(\frac{\xi_z}{\xi_i} + \frac{\xi_z}{\xi_c} \right) \frac{P_j}{\theta_i} \frac{R_f}{R_j} \tilde{u}_i^2 \tag{2.9}$$

where i = 1,7 and j = f, ox, respectively. Here $\tilde{u}_i = (\tilde{u}_{i,in} + \tilde{u}_{i,out})/2$ is the channel dimensionless mean velocity, defined as $\tilde{u} = u/(R_f T_\infty)^{1/2}$, and f the friction factor. According to mass conservation, the dimensionless mean velocities in the gas channels are

$$\tilde{u}_1 = \frac{C\theta_1}{\tilde{A}_{c1} P_f} \left[\psi_f - \frac{\psi_{H_2}}{2} \right] \tag{2.10}$$

$$\tilde{u}_7 = \frac{R_{ox} C\theta_7}{R_f \tilde{A}_{c7} P_{ox}} \left[\psi_{ox} - \frac{\psi_{O_2}}{2} \right] \tag{2.11}$$

$$C = \frac{(R_f T_\infty)^{1/2} \dot{m}_{ref}}{p_\infty V_T^{2/3}} \tag{2.12}$$

where $\tilde{A}_{ci} = n_c L_c L_i / V_T^{2/3}$, i = 1,7 , is the dimensionless total duct cross section area in the fuel cell and oxidant channels and R_f the ideal gas constant of the fuel, kJ kg^{-1} K^{-1}. Eqs (2.9)-(2.12) model the mean velocity and pressure drop on the gas channels in the CV1 and CV7, ΔP_1 and ΔP_7 .

We use the following relations to model the friction factor and the heat transfer coefficients in the gas channels.

For the laminar regime (Re_{D_h} < 2300) [63]:

$$f_i \, Re_{Dh,j} = 24(1 - 1.3553\delta_i + 1.9467\delta_i^{\,2} - 1.7012\delta_i^3 + 0.9564\delta_i^4 - 0.25371\delta_i^5) \tag{2.13}$$

$$\frac{h_i D_{h,i}}{k_i} = 7.541(1 - 2.610\delta_i + 4.970\delta_i^{\,2} - 5.119\delta_i^3 + 2.702\delta_i^4 - 0.548\delta_i^5) \tag{2.14}$$

where $\delta_i = L_c / L_i$, for $L_c \le L_i$ and $\delta_i = L_i / L_c$, for $L_c > L_i$; $D_{h,i} = 2L_c L_i / (L_t + L_c)$ and $Re_{Dh,i} = u_i D_{h,i} \rho_i / \mu_i$ and i = 1,7.

The correlations used for the turbulent regime are [64]:

$$f_i = 0.079 \, Re_{Dh,i}^{-1/4} \qquad (2300 < Re_{Dh,i} < 2x10^4) \tag{2.15}$$

$$\frac{h_i D_{h,i}}{k_i} = \frac{(f_i / 2)(D_{h,i} - 10^3) Pr_i}{1 + 12.7(f_i / 2)^{1/2}(Pr^{2/3} - 1)} \qquad (2300 < Re_{Dh,i} < 5x10^6) \tag{2.16}$$

The CV2 is the diffusion-backing layer; although this control volume is considered part of the electrode the electrochemical reaction does not occur here, the gas reacts just in the CV3 (reacting layer), where the three phase boundary (catalyst, reacting gas and electrolyte) is present.

Since the mass of fluid in CV2 can be considered negligible when compared with the solid mass of the electrode, just the later is taken into account in the energy balance.

The net heat transfer rates at CV2 are $\tilde{Q}_2 = -\tilde{Q}_{12} + \tilde{Q}_{w2} + \tilde{Q}_{23} + \tilde{Q}_{2ohm}$, where $\tilde{Q}_{23} = \tilde{k}_{s,a}(1-\phi_2)\tilde{A}_s(\theta_2 - \theta_3)/[(\xi_2 + \xi_3)/2]$, where dual-porosity electrodes have been considered, as shown in Fig. 2.4.

The pores are approximated as parallel tubes with an average diameter of the same order as the square root of the porous medium permeability, $K^{1/2}$. Therefore, the wetted area for each porous control volume is $A_{j,wet} = 4\phi_j L_j K_j^{-1/2} A_s$ where K_j is the permeability.

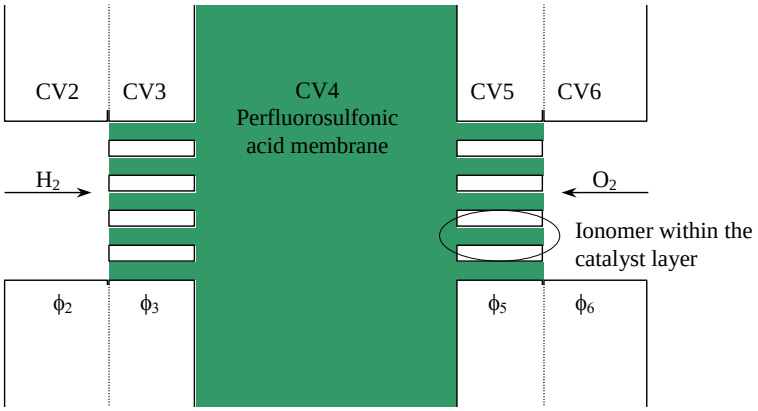

Figure 2.4: Cross-section details of dual-porosity electrodes and the internal structure.

Assuming diffusion to be the dominant transport mechanism across the diffusion and catalyst layer [65], the fuel and oxidant mass fluxes are given by

$$j_i = -[D(\rho_{out} - \rho_{in})/L]_i \qquad (2.17)$$

Where ρ is the density, kg m^{-3}; $D = B\{r[8\overline{R}T/\pi M]^{1/2}\phi^q\}$, is the Knudsen diffusion coefficient, , B the dimensionless constant [66]; r the porous radius, m; $\overline{R}$ the universal gas constant, kJ $kmol^{-1}$ K^{-1},q the tortuosity [67-68]; Therefore ,

$$P_{i,out} = P_{i,in} - \frac{j_i R_k T_\infty L_i \theta_i}{D_i p_\infty}, \quad i = 2,6; \; k = f,ox \tag{2.18}$$

where $j_2 = \dot{m}_{H_2} / A_{3,wet}$ and $j_6 = \dot{m}_{o_2} / A_{5,wet}$, and $A_{3,wet}$ and $A_{5,wet}$. The average pressures in CV2 and CV6 are estimated as

$$P_i = \frac{1}{2}(P_{i,in} + P_{i,out}), \; i = 2,6 \tag{2.19}$$

The energy balance delivers the CV2 temperature,

$$(\theta_1 - \theta_2) + \frac{\tilde{Q}_2}{\psi_{H_2}} = 0 \tag{2.20}$$

The electrical current is generated by the electrochemical reaction in the anode reaction layer (CV3). The water content of the polymeric membrane (Nafion 117, considered as the electrolyte for PEMFC) needs to be taken into account when we evaluate its electrical conductivity. In PEMFC analysis, the CV3 is composed by the electrode, the solid electrolyte (Nafion 117) and a liquid solution, however, in the thermal analysis just the solid is considered, since the mass of fluid in CV3 is also negligible in comparison with the mass of solid. The electrochemical reaction at the anode for PEMFC is:

$$H_{2(g)} \rightarrow 2H^+_{(aq)} + 2e^- \tag{2.21}$$

The dimensionless enthalpy of formation is defined by $\tilde{H}_i = \dot{n}_i H_i / (\dot{m}_{ref} c_{p,f} T_\infty)$, where the subscript i refers to a substance or a control volume. The enthalpy change due to the anode reaction is given by $\Delta H_3 = \sum_{products}[\upsilon_i H_i(T_i)] - \sum_{reactants}[\upsilon_i H_i(T_i)]$ and $W_{e3} = -\Delta G_3$, where ΔH_3 is the CV3 reaction enthalpy change, kJ/kmol; υ_i the stoichiometric coefficients; $H_i(T_i)$ the molar enthalpy of formation (kJ/kmol) at a temperature T_i of reactants and products i, ΔG_3 the CV3 reaction Gibbs free energy change, kJ/kmol; and W_{e3} is the maximum electrical work

generated due to the reaction at the anode, kJ/kmol. The enthalpy of formation are obtained from tabulated values [69-70] at T_2 for $H_{2(g)}$ and T_3 for $H^+_{(aq)}$ at 1 atm.

The reaction Gibbs free energy change, ΔG, is a function of temperature, pressure and concentrations, [70]

$$\Delta G = \Delta G^0 + \bar{R}T \ln Q \tag{2.22}$$

where $\Delta G^0 = \Delta H^0 - T\Delta S^0$. Where Q is the reaction quotient expressed as $Q_3 = \left[H^+_{(aq)}\right]^2 / p_{H_2}$, where $\left[H^+_{(aq)}\right]^2$ is the molar concentration of the acid solution, (mol l^{-1}), and $p_{H_2} = p_{2,out}$.

The dimensionless net heat transfer in CV3 is given by $\tilde{Q}_3 = -\tilde{Q}_{23} + \tilde{Q}_{w3} + \tilde{Q}_{34} + \tilde{Q}_{3ohm}$ The heat transfer rate between CV3 and CV4 (the polymer electrolyte) is dominated by conduction, therefore $\tilde{Q}_{34} = -(1-\phi_3)(\theta_3 - \theta_4)\tilde{A}_s 2\tilde{k}_{s,a}\tilde{k}_p / (\xi_4 \tilde{k}_{s,a} + \xi_3 \tilde{k}_p)$, where $\tilde{k}_p$ is the dimensionless thermal conductivity of the polymer electrolyte.

The mass balances for CV3 together with the anode reaction equation (Eq. 2.21) deliver the relations $\dot{n}_{H_2} = \dot{m}_{H_2} / M_{H_2}$, $\dot{n}_{H^+} = 2\dot{n}_{H_2}$, $\dot{m}_{H^+} = 2\dot{n}_{H_2} M_{H^+}$. The energy balance for the CV3 is:

$$\tilde{Q}_3 - \Delta\tilde{H}_3 + \Delta\tilde{G}_3 = 0 \tag{2.23}$$

where, $(\Delta\tilde{H}_3, \Delta\tilde{G}_3) = \dot{n}_{H_2}(\Delta H_3, \Delta G_3) / \left(\dot{m}_{ref} c_{p,f} T_\infty\right)$.

In the cathode reaction layer (CV5) of a PEMFC, the following reaction occurs

$$\frac{1}{2} O_{2(g)} + 2e^- + 2H^+_{(aq)} \rightarrow H_2O_{(l)} \tag{2.24}$$

The dimensionless net heat transfer in CV4 is obtained from $\tilde{Q}_4 = -\tilde{Q}_{34} + \tilde{Q}_{w4} + \tilde{Q}_{45} + \tilde{Q}_{4ohm}$ where $\tilde{Q}_{45} = -(1-\phi_5)(\theta_4 - \theta_5)\tilde{A}_s 2\tilde{k}_{s,c}\tilde{k}_p / (\xi_4 \tilde{k}_{s,c} + \xi_5 \tilde{k}_p)$. The CV4 temperature is obtained from

$$\tilde{Q}_4 + \tilde{H}(\theta_3)_{H^+_{(aq)}} - \tilde{H}(\theta_4)_{H^+_{(aq)}} = 0 \qquad (2.25)$$

The analysis in the cathode reaction layer (CV5) is analogous to what we previously presented in the anode reaction layer (CV3) analysis. The CV5 dimensionless temperature is obtained by

$$\tilde{Q}_5 - \Delta\tilde{H}_5 + \Delta\tilde{G}_5 = 0 \qquad (2.26)$$

where $(\Delta\tilde{H}_5, \Delta\tilde{G}_5) = \dot{n}_{O_2}(\Delta H_5, \Delta G_5)/\left(\dot{m}_{ref} c_{p,f} T_\infty\right)$.

Similarly, the dimensionless net heat transfer rate flowing in CV5 is given by $\tilde{Q}_5 = -\tilde{Q}_{45} + \tilde{Q}_{w5} + \tilde{Q}_{56} + \tilde{Q}_{5ohm}$, with $\tilde{Q}_{56} = -\tilde{k}_{s,c}(1-\phi_6)\tilde{A}_s(\theta_5 - \theta_6)/\left[(\xi_5 + \xi_6)/2\right]$.

The enthalpy change during cathode reaction is $\Delta H_5 = \sum_{products}\left[\upsilon_i H_i(T_i)\right] - \sum_{reactants}\left[\upsilon_i H_i(T_i)\right]$, while $W_{e5} = -\Delta G_5$. The enthalpy of formation are obtained from tabulated values [54-55] at T_6 for $O_{2(g)}$ and T_4 for $H^+_{(aq)}$ and T_5 for $H_2O_{(l)}$ at 1 atm (Eq. 2.24).

The change of Gibbs free energy ΔG_5 for the reaction of Eq. (2.24) is calculated by using Eq. (2.22), where the CV5 reaction quotient is $Q_5 = \left\{\left[H^+_{(aq)}\right]^2 p_{O_2}^{1/2}\right\}^{-1}$, where $p_{O_2} = p_{6,out}$.

The dimensionless net heat transfer rate in CV6 result from $\tilde{Q}_6 = -\tilde{Q}_{56} + \tilde{Q}_{w6} + \tilde{Q}_{67} + \tilde{Q}_{6ohm}$, with $\tilde{Q}_{67} = \tilde{h}_7\tilde{A}_s(1-\phi_6)(\theta_7 - \theta_6)$, $\tilde{h}_7 = h_7 V_T^{2/3}/\left(\dot{m}_{ref} c_{p,f}\right)$. The dimensionless temperature for CV6 is given by

$$\tilde{Q}_6 + \psi_{O_2}\frac{c_{p,ox}}{c_{p,f}}(\theta_7 - \theta_6) + \tilde{H}(\theta_5)_{H_2O} - \tilde{H}(\theta_6)_{H_2O} = 0 \qquad (2.27)$$

The dimensionless net heat transfer rate in CV7 is $\tilde{Q}_7 = -\tilde{Q}_{67} + \tilde{Q}_{w7} + \tilde{Q}_{7ohm}$.

$$\tilde{Q}_7 + \psi_{ox}\frac{c_{p,ox}}{c_{p,f}}(\theta_{ox} - \theta_7) + \tilde{H}(\theta_6)_{H_2O} - \tilde{H}(\theta_7)_{H_2O} = 0 \qquad (2.28)$$

2.1.4 Electrochemical Model

Based on the electrical conductivities and geometry of each compartment, the electrical resistances, $\beta(\Omega)$, are given by:

$$\beta_i = \frac{\xi_i}{\tilde{A}_s V_T^{1/3} \sigma_i (1-\phi_i)}, \qquad i = 1,2,6,7 \tag{2.29}$$

$$\beta_i = \frac{\xi_i}{\tilde{A}_s V_T^{1/3} \sigma_i \phi_i}, \qquad i= 3, 4, 5, \ (\phi_4 = 1) \tag{2.30}$$

The ionic conductivity, $\sigma(\Omega^{-1}m^{-1})$, of Nafion 117 as a function of temperature is given by the following empirical formula [71]:

$$\sigma_i(\theta) = \exp\left[1268\left(\frac{1}{303} - \frac{1}{\theta_i T_\infty}\right)\right](0.5139\lambda_i - 0.326), \ i = 3,4,5 \tag{2.31}$$

The conductivities of the catalyst layers are given by $\sigma_3\phi_3$ and $\sigma_5\phi_5$, according to Eqs. (2.30) and (2.31). The conductivities of the diffusive layer, σ_2 and σ_6, are the carbon-phase conductivities [72]. Finally, the conductivities of CV1 and CV7, σ_1 and σ_7, are given by the electrical conductivity of the bipolar plate material.

In polymer electrolyte membrane, the water content λ, is described as the ratio of the number of water molecules to the number of chargers sites, meaning, the number of ions $SO_3^- H^+$. Usually, the anode water content in the anode is different from the cathode [73]; therefore for assumed values of λ_a (anode water content) and λ_c (cathode water content), and by assuming a linear variation of the water content along the membrane thickness, the average water content in the membrane is defined as

$$\lambda = \frac{\lambda_a + \lambda_c}{2} \tag{2.32}$$

Eq. (2.32) allows for the calculation of $\left[H^{+}_{(aq)}\right]$ as a function of λ, namely $\left[H^{+}_{(aq)}\right] \cong \rho_{H_2O}/(\lambda M_{H_2O})$ for a dilute water solution.

The appropriate figure of merit for evaluating the performance of a fuel cell is the polarization curve, i.e., the fuel cell total potential as a function of current. The dimensionless potential ($\tilde{V}$) and the dimensionless overpotential ($\tilde{\eta}$) are defined in terms of a given reference voltage, V_{ref}, namely $\tilde{V} = V/V_{ref}$ and $\tilde{\eta} = \eta/V_{ref}$. The dimensionless actual potential $\tilde{V}_i$ is an accumulated result of dimensionless irreversible anode electrical potential $\tilde{V}_{i,a}$, dimensionless irreversible cathode electrical potential $\tilde{V}_{i,c}$, and the dimensionless ohmic loss $(\tilde{\eta}_{ohm})$ in the space from CV1 to CV7, i.e.,

$$\tilde{V}_i = \tilde{V}_{i,a} + \tilde{V}_{i,c} - \tilde{\eta}_{ohm} \tag{2.33}$$

The ohmic loss $\tilde{\eta}_{ohm}$ is estimated by

$$\tilde{\eta}_{ohm} = \frac{I}{V_{ref}} \sum_{i=1}^{7} \beta_i \tag{2.34}$$

The reversible electrical potential at the anode is given by the Nernst equation [55],

$$V_{e,a} = V^{o}_{e,a} - \frac{\bar{R}T_3}{nF} \ln Q_3 \tag{2.35}$$

where $V_{e,a} = \Delta G_3/(-nF)$ and $V^{o}_{e,a} = \Delta G^{o}_{3}/(-nF)$; n is the equivalent electron per mole of reactant, eq mol^{-1} and F the Faraday constant. At the anode there are two mechanisms for potential losses; (i) charge transfer, and (ii) mass diffusion. The potential loss (η_a) due to charge transfer is obtained implicitly from the Butler-Volmer equation for a given current I [74-75]

$$\frac{I}{A_{3,wet}} = i_{o,a}\left\{\exp\left[\frac{(1-\alpha_a)\eta_a F}{\bar{R}T_3}\right] - \exp\left[-\frac{\alpha_a \eta_a F}{\bar{R}T_3}\right]\right\} \tag{2.36}$$

where α_a is the anode charge transfer coefficient, and $i_{o,a}$ is the anode exchange current density (function of catalyst type and layer morphology). At thermodynamic equilibrium, the current at the anode (forward) and at the cathode (reverse) must balance so there is no net current density, this is what is called *anode exchange current density ($i_{o,a}$)*. The anode charge transfer coefficient (α_a) represents how the change in the electrical potential across the reaction interface (anode) changes the sizes of the forward (oxidation) versus reverse (reduction) activation barrier.

The potential loss due to mass diffusion is [74-75]:

$$\eta_{d,a} = \frac{\bar{R}T_3}{nF}\ln\left(1-\frac{I}{A_{3,wet}i_{Lim,a}}\right) \tag{2.37}$$

where, from Eq. (2.18):

$$i_{lim,a} = \frac{p_f D_2 nF}{M_{H_2} L_2 R_f \theta_2 T_\infty} \tag{2.38}$$

The limiting current density at the anode ($i_{Lim,a}$) occurs when the gas is completely depleted in the very thin active catalyst layer fraction situated at the interface with the gas diffuser, meaning $P_{2,out}$=0.

The resulting electrical potential at the anode is $\tilde{V}_{i,a} = \tilde{V}_{e,a} - \tilde{\eta}_a - \left|\tilde{\eta}_{d,a}\right|$, where we have taken the absolute value of $\eta_{d,a}$ because $\eta_{d,a} < 0$.

The methodology in estimating the anode potential is valid in building the cathode potential correlations. Similarly , the actual cathode potential is $\tilde{V}_{i,c} = \tilde{V}_{e,c} - \tilde{\eta}_c - \left|\tilde{\eta}_{d,c}\right|$ and the reversible electrical cathode potential is $V_{e,c} = V^o_{e,c} - \left(\bar{R}T_5/nF\right)\ln Q_5$, where $Q_5 = \left\{\left[H^+_{(aq)}\right]^2 p^{1/2}_{O_2}\right\}^{-1}$ and $V^o_{e,c} = \Delta G^o_5/(-nF)$. The Butler-Volmer equation for calculating the cathode side overpotential η_c is $I/A_{5,wet} = i_{o,c}\left[\exp\left((1-\alpha_c)\eta_c F/\left(\bar{R}T_5\right)\right) - \exp\left(-\alpha_c\eta_c F/\left(\bar{R}T_5\right)\right)\right]$. The cathode mass

diffusion depleting overpotential is $\eta_{d,c} = \{\overline{R}T_5/(nF)\}\ln\left(1-I/\left(A_{5,wet}\, i_{Lim,c}\right)\right)$, and the cathode limiting current density is $i_{lim,c} = 2p_{ox}D_6nF/\left(M_{O_2}L_6R_{ox}\theta_6T_\infty\right)$.

2.1.5 Fuel Cell Net Power Output and Efficiency

The pumping power $\tilde{W}_p$ is required to supply the fuel cell with fuel and oxidant. Therefore the total net power (available for utilization) of the fuel cell is

$$\tilde{W}_{net} = \tilde{W} - \tilde{W}_p \tag{2.39}$$

where $\tilde{W} = \tilde{V}_i\tilde{I}$, and $\tilde{I} = I/I_{ref}$ is the total fuel cell electrical power output , and

$$\tilde{W}_p = \psi_f S_f \frac{\theta_1}{P_1}\Delta P_1 + \psi_{ox}S_{ox}\frac{\theta_7}{P_7}\Delta P_7 \tag{2.40}$$

$$S_i = \frac{m_{ref}T_\infty R_i}{V_{ref}I_{ref}}, \quad i = f,ox \tag{2.41}$$

The ideal efficiency or maximum theoretical efficiency is expressed as

$$\eta_i = \frac{W_{e3} + W_{e5}}{\Delta H_3 + \Delta H_5} \tag{2.42}$$

Using the dimensionless variables we can re-write the ideal efficiency as

$$\eta_i = \frac{\Delta\tilde{G}_3 + \Delta\tilde{G}_5}{\Delta\tilde{H}_3 + \Delta\tilde{H}_5} \tag{2.43}$$

The first law efficiency is given as

$$\eta_I = E\frac{\tilde{W}}{\Delta\tilde{H}_3 + \Delta\tilde{H}_5} \tag{2.44}$$

where $E = \dfrac{V_{ref}I_{ref}}{\dot{m}_{ref}c_{p,f}T_\infty}$.

The second law efficiency is defined as the ratio of the actual power to the reversible power of the fuel cell and can be expressed as

$$\eta_{II} = E\frac{\tilde{W}}{\Delta\tilde{G}_3 + \Delta\tilde{G}_5} \tag{2.45}$$

The net efficiency of the fuel cell is

$$\eta_{net} = E\frac{\tilde{W}_{net}}{\Delta\tilde{H}_3 + \Delta\tilde{H}_5} \tag{2.46}$$

2.2 Alkaline Membrane Fuel Cell Model

In the Chapter 1 we described two possible configurations of alkaline fuel cells according to how the electrolyte is confined between the electrodes; mobile or static electrolyte. We will focus our study in static electrolyte alkaline fuel cell, in which the electrolyte is a liquid alkaline solution confined in a porous medium called membrane.

A schematic diagram of the internal structure of a PEMFC is shown in Fig. 2.1, the same diagram is suitable for AMFC, where the membrane (CV4) is an alkaline membrane.

Differently of PEMFC, air is not recommended to be used as oxidant for AMFC. The carbon monoxide present in the air reacts with hydroxyl (Eq.2.47) consuming OH^- generating water and making the efficiency of the fuel cell to decrease. For that reason we will consider pure oxygen for the mathematical model and the experimental validation of AMFC.

$$CO_2 + 2OH^- \rightarrow CO_3^{2-} + H_2O \tag{2.47}$$

Likewise the model for PEMFC, the AMFC model consists of applying conservation and electrochemical equations for the control volumes. The reversible electrical potential and power of the fuel cell are functions of the temperature and pressure fields. The actual electrical potential and power of the fuel cell are obtained by subtracting from the reversible potential the losses due to surface overpotentials, slow diffusion and all internal ohmic losses through the cell. These are functions of the total cell current (I), which is directly related to the external

load (or the cell voltage). The total cell current is also considered an independent variable in this study. The present analysis is also for steady state fuel cell operation.

The control volumes (CV) are fuel channel (CV1), the anode diffusion-backing layer (CV2), the anode reaction layer (CV3), alkaline membrane (CV4), the cathode reaction layer (CV5), the cathode diffusion backing layer (CV6) and the oxidant channel (CV7).

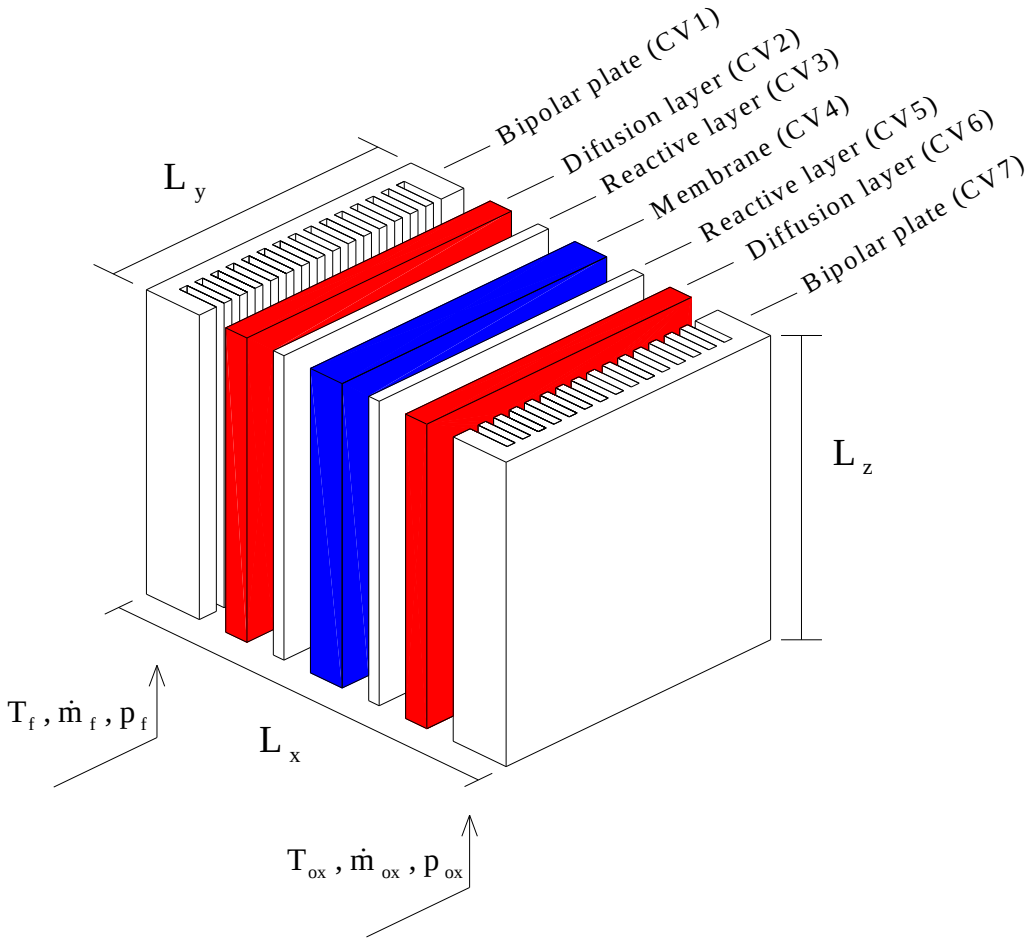

Figure 2.5: Control volume distribution of a single fuel cell unit (AMFC). The fuel channels (CV1), the anode diffusion layer (CV2), the anode reaction layer (CV3), alkaline membrane (CV4), the cathode reaction layer (CV5), the cathode diffusion layer (CV6) and the oxidant channel (CV7).

2.2.1 Dimensionless Variables and Mass Balance

The dimensionless variables and the mass balance defined previously in the section 2.1.1 and section 2.1.2 respectively are the same for AMFC model. Therefore, the Eq. 2.1-2.6 are valid for both fuel cells, PEMFC and AMFC.

The Fig. 2.6 show the upper view of the control volumes defined for the AMFC. A close comparison between the Fig. 2.6 and Fig. 2.2 will show that the flow indicated by the arrows on the figure indicate that the reactions in the electrodes are not the same for both fuel cells.

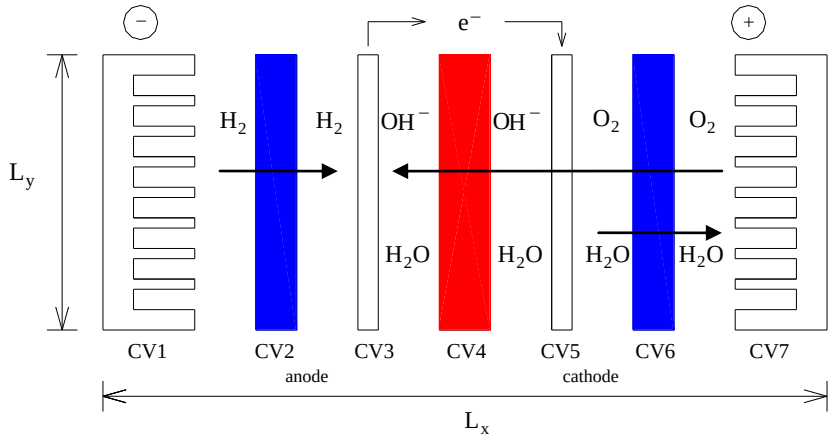

Figure 2.6: Upper view of the control volumes of a single AMFC.

2.2.2 Energy Conservation Analysis

The geometric parameters presented in the section 2.1.3 and the internal dimension of gas channels are also valid for AMFC model. The wall heat transfer area of one control volume is

$$A_{wi} = \tilde{p}_s L_i \ (2 \le i \le 6) \ ; \ A_{wi} \cong \tilde{p}_s L_i + L_y L_z \ (i = 1,7) \qquad (2.48)$$

where $\tilde{p}_s = 2(L_y + L_z)$ is the perimeter of the fuel cell cross-section.

The control volumes are $V_j = L_y L_z L_j \ (2 \le j \le 6)$ and $V_j = n_c L_c L_l L_z \ (j = 1, 7)$, where n_c is the integer part of $L_y/(L_t + L_c)$.

Since the AMFC and PEMFC have the same energy interaction for the control volumes where the electrochemical reactions are not present, the fuel and oxidant channels (CV1 and

CV7) and the anode and cathode diffusion layer (CV2 and CV6) have the same formulation for energy analysis for both fuel cells. For simplicity, we decided to group them according to their similarity.

2.2.2.1 Fuel and Oxidant Channels (CV1 and CV7)

The energy balance for the CV1 states that:

$$\tilde{Q}_{w1} + \psi_f(\theta_f - \theta_1) + \tilde{Q}_{12} + \tilde{Q}_{1ohm} = 0 \tag{2.49}$$

where

$$\tilde{Q}_{wi} = N_i \tilde{A}_{wi}(1-\theta_i),\ \tilde{Q}_{iohm} = I^2\beta_i \Big/ \left(\dot{m}_{ref} c_{p,f} T_\infty\right) \tag{2.50}$$

$$\tilde{Q}_{12} = \tilde{h}_1 \tilde{A}_s(1-\phi_2)(\theta_2 - \theta_1),\ \tilde{A}_s = L_y L_z \Big/ V_T^{2/3} \tag{2.51}$$

The energy balance for the CV7 states that:

$$\tilde{Q}_7 + \psi_{ox}\frac{c_{p,ox}}{c_{p,f}}(\theta_{ox} - \theta_7) + \tilde{H}(\theta_6)_{H_2O} - \tilde{H}(\theta_7)_{H_2O} = 0 \tag{2.52}$$

where

$$\tilde{Q}_7 = -\tilde{Q}_{67} + \tilde{Q}_{w7} + \tilde{Q}_{7ohm} \tag{2.53}$$

$$\tilde{Q}_{67} = \tilde{h}_7 \tilde{A}_s(1-\phi_6)(\theta_7 - \theta_6) \tag{2.54}$$

$$\tilde{H}_i = \dot{n}_i H_i \Big/ \left(\dot{m}_{ref}\, c_{p,f}\, T_\infty\right) \tag{2.55}$$

The same assumptions considered for the pressure drop analysis for PEMFC are considered for the pressure drop analysis for AMFC, (the channels are straight and sufficient

slender). Therefore, the Eqs. (2.9-2.16) are valid for AMFC as well. The pressure drop and the velocity in the gas channels are, respectively

$$\Delta P_i = n_c f_i \left(\frac{\xi_z}{\xi_i} + \frac{\xi_z}{\xi_c} \right) \frac{P_j}{\theta_i} \frac{R_f}{R_j} \tilde{u}_i^2 \tag{2.56}$$

where i = 1,7 and j = f, ox, respectively. Here $\tilde{u}_i = (\tilde{u}_{i,in} + \tilde{u}_{i,out})/2$ is the channel dimensionless mean velocity, defined as $\tilde{u} = u/(R_f T_\infty)^{1/2}$, and f the friction factor. According to mass conservation, the dimensionless mean velocities in the gas channels are

$$\tilde{u}_1 = \frac{C\theta_1}{\tilde{A}_{c1} P_f} \left[\psi_f - \frac{\psi_{H_2}}{2} \right] \tag{2.57}$$

$$\tilde{u}_7 = \frac{R_{ox} C\theta_7}{R_f \tilde{A}_{c7} P_{ox}} \left[\psi_{ox} - \frac{\psi_{O_2}}{2} \right] \tag{2.58}$$

$$C = \frac{(R_f T_\infty)^{1/2} \dot{m}_{ref}}{p_\infty V_T^{2/3}} \tag{2.59}$$

where $\tilde{A}_{ci} = n_c L_c L_i / V_T^{2/3}$, i=1,7, is the dimensionless total duct cross section area in the fuel cell and oxidant channels and R_f the ideal gas constant of the fuel, kJ kg^{-1} K^{-1}. Eqs (2.56)-(2.59) model the mean velocity and pressure drop on the gas channels in the CV1 and CV7, ΔP_1 and ΔP_7.

The relations to model the friction factor and the heat transfer coefficient in the gas channel for AMFC is also the same demonstrated for PEMFC. Therefore the Eqs.(2.13-2.16) are also still valid.

For the laminar regime (Re_{D_h} < 2300) [63]:

$$f_i \, Re_{Dh,j} = 24(1 - 1.3553\delta_i + 1.9467\delta_i^2 - 1.7012\delta_i^3 + 0.9564\delta_i^4 - 0.25371\delta_i^5) \tag{2.60}$$

$$\frac{h_i D_{h,i}}{k_i} = 7.541(1 - 2.610\delta_i + 4.970\delta_i^{\,2} - 5.119\delta_i^3 + 2.702\delta_i^4 - 0.548\delta_i^5) \qquad (2.61)$$

where $\delta_i = L_c/L_i$, for $L_c \le L_i$ and $\delta_i = L_i/L_c$, for $L_c > L_i$; $D_{h,i} = 2L_cL_i/(L_t + L_c)$ and $Re_{Dh,i} = u_i D_{h,i}\rho_i/\mu_i$ and i = 1,7.

The correlations used for the turbulent regime are [64]:

$$f_i = 0.079\,Re_{Dh,i}^{-1/4} \qquad (2300 < Re_{Dh,i} < 2x10^4) \qquad (2.62)$$

$$\frac{h_i D_{h,i}}{k_i} = \frac{(f_i/2)(D_{h,i} - 10^3)\,Pr_i}{1 + 12.7(f_i/2)^{1/2}(Pr^{2/3} - 1)} \qquad (2300 < Re_{Dh,i} < 5x10^6) \qquad (2.63)$$

2.2.2.2 Anode and Cathode Diffusion Layer (CV2 and CV6)

The purpose of diffusion layer is to uniformly provide gas to the reactive layer and remove the byproducts of the reactions. The diffusion layer is made hydrophobic to avoid the electrolyte solution to go to the gas stream. Therefore, we considered that there is only hydrogen in the anode diffusion layer (CV2) and oxygen and water in the cathode diffusion layer (CV6).

We assume diffusion being the dominant mass transfer mechanism in the CV2, CV3, CV5 and CV6, so we write the mass flux of fuel and oxidant as

$$j_i = -\left[D(\rho_{out} - \rho_{in})/L\right]_i \qquad (2.64)$$

Where ρ is the density, kg m^{-3}; $D = B\left\{r\left[8\overline{R}T/\pi M\right]^{1/2}\phi^q\right\}$, the Knudsen diffusion coefficient, where B the dimensionless constant; r the porous radius, m; $\overline{R}$ is the universal gas constant, kJ $kmol^{-1}$ K^{-1}; q the tortuosity [67-68]; Therefore ,

$$P_{i,out} = P_{i,in} - \frac{j_i R_k T_\infty L_i \theta_i}{D_i p_\infty}, \quad i = 2,6;\ k = f,ox \qquad (2.65)$$

where $j_2 = \dot{m}_{H_2} / A_{3,wet}$ and $j_6 = \dot{m}_{o_2} / A_{5,wet}$, and $A_{3,wet}$ and $A_{5,wet}$. The average pressures in CV2 and CV6 are estimated as

$$P_i = \frac{1}{2}(P_{i,in} + P_{i,out}),\ i = 2,6 \tag{2.66}$$

Only the mass of the solid part of the diffusive layers is take into considerations for the energy balance of CV2 and CV6. Since these layers are hydrophobic we make the assumption that mass of fluid is negligible compared to the mass of solid. Hydrogen diffuses through the CV2 and CV3 and oxygen and water vapor diffuse through the CV5 and CV6.

The energy balance for the CV2 and CV6 are, respectively

$$(\theta_1 - \theta_2) + \frac{\tilde{Q}_2}{\psi_{H_2}} = 0 \tag{2.67}$$

$$\tilde{Q}_6 + \psi_{O_2} \frac{c_{p,ox}}{c_{p,f}}(\theta_7 - \theta_6) + \tilde{H}(\theta_5)_{H_2O} - \tilde{H}(\theta_6)_{H_2O} = 0 \tag{2.68}$$

where $\tilde{Q}_2 = -\tilde{Q}_{12} + \tilde{Q}_{w2} + \tilde{Q}_{23} + \tilde{Q}_{2ohm}$, $\tilde{Q}_{23} = \tilde{k}_{s,a}(1-\phi_2)\tilde{A}_s(\theta_2 - \theta_3)/[(\xi_2 + \xi_3)/2]$, $\tilde{Q}_6 = -\tilde{Q}_{56} + \tilde{Q}_{w6} + \tilde{Q}_{67} + \tilde{Q}_{6ohm}$ and $\tilde{Q}_{56} = -\tilde{k}_{s,c}(1-\phi_6)\tilde{A}_s(\theta_5 - \theta_6)/[(\xi_5 + \xi_6)/2]$.

2.2.2.3 Anode and Cathode Catalyst Layer (CV3 and CV5)

These are the control volumes where the electrochemical reactions occur. These layers are also porous and less hydrophobic than the diffusion layers.

The anode (CV3) is composed by the porous electrode, fuel (hydrogen) and electrolyte solution (KOH) that is present in the pores of the electrode. The electrons released by the oxidation of the hydrogen [Eq.(2.69)] in the CV3 pass through an external circuit and are used as reactants for the reduction of the oxygen in the CV5 [Eq. (2.70)]. The cathode (CV5) is also porous and less hydrophobic than the diffusion layers. The CV5 is composed by the porous electrode, oxygen and the electrolyte.

The Hydrogen Oxidation Reaction (HRO)

$$H_2 + 2OH^-_{(aq)} \rightarrow 2H_2O_{(l)} + 2e^- \quad (2.69)$$

The Oxygen Reduction Reaction (ORR)

$$\frac{1}{2}O_{2(g)} + H_2O_{(l)} + 2e^- \rightarrow 2OH^- \quad (2.70)$$

On thermal analysis of CV3 and CV5, the mass of liquid contained in these CVs is also neglected compared to the solid mass of the electrode. CV3 and CV5 interact thermally with the adjacent control volumes by conduction and to the ambient by convection. Heat is generated by the electrochemical reactions and by the irreversible mechanisms (ohmic resistance, activation and concentration overpotentials losses) [76].

In the present model, we include the heat generation due to activation overpotential losses (η_a) and concentration overpotential losses ($\eta_{d,a}$). However the ohmic heat generated in the CV3, CV4 and CV5 due to the ion transport resistance of the solution and the electric resistance of their solid components has been previously considered for the PEMFC model. The calculation of the overpotential losses (η_a, $\eta_{d,a}$ and η_{ohm}) are discussed later in the electrochemical model section.

The energy balance for the CV3 is

$$\tilde{Q}_3 - \Delta\tilde{H}_3 + \Delta\tilde{G}_3 = 0 \quad (2.71)$$

where

$$\tilde{Q}_3 = -\tilde{Q}_{23} + \tilde{Q}_{w3} + \tilde{Q}_{34} + \tilde{Q}_{3ohm} + \tilde{Q}_{3,act} + \tilde{Q}_{3,dif} \quad (2.72)$$

$$\tilde{Q}_{34} = -(1-\phi_3)(\theta_3 - \theta_4)\tilde{A}_s 2\tilde{k}_{s,a}\tilde{k}_{memb} / (\xi_4\tilde{k}_{memb} + \xi_3\tilde{k}_{memb}) \quad (2.73)$$

$$\tilde{Q}_{3,act} = \frac{\eta_a I}{\dot{m}_{ref} c_{p,f} T_\infty}, \quad \tilde{Q}_{3,dif} = \frac{\eta_{d,a} I}{\dot{m}_{ref} c_{p,f} T_\infty}$$

(2.74)

The energy balance for the CV5 is

$$\tilde{Q}_5 - \Delta\tilde{H}_5 + \Delta\tilde{G}_5 = 0 \tag{2.75}$$

where

$$\tilde{Q}_5 = -\tilde{Q}_{45} + \tilde{Q}_{w5} + \tilde{Q}_{56} + \tilde{Q}_{5ohm} + \tilde{Q}_{5,act} + \tilde{Q}_{5,dif} \tag{2.76}$$

$$\tilde{Q}_{45} = -(1-\phi_5)(\theta_4 - \theta_5)\tilde{A}_s 2\tilde{k}_{s,c}\tilde{k}_{memb} / (\xi_4\tilde{k}_{s,c} + \xi_5\tilde{k}_{memb}) \tag{2.77}$$

$$\tilde{Q}_{5,act} = \frac{\eta_a I}{\dot{m}_{ref} c_{p,f} T_\infty}, \quad \tilde{Q}_{5,dif} = \frac{\eta_{d,a} I}{\dot{m}_{ref} c_{p,f} T_\infty}$$

(2.78)

where $\tilde{k}_{memb} = k_{memb} V_T^{1/3} / \dot{m}_{ref} c_{p,f}$, $k_{memb} = k_{sol}\phi_4 + k_{pap}(1-\phi_4)$, k_{sol} is the thermal conductivity of the KOH solution, W m^{-1} K^{-1} [77]; k_{pap} is the thermal conductivity of the chromatography paper (material of the membrane), W m^{-1} K^{-1}.

The dimensionless molar enthalpy change and dimensionless Gibbs free energy change for CV3 and CV5 are $(\Delta\tilde{H}_3, \Delta\tilde{G}_3) = \dot{n}_{H_2}(\Delta H_3, \Delta G_3) / \left(\dot{m}_{ref} c_{p,f} T_\infty\right)$ and $(\Delta\tilde{H}_5, \Delta\tilde{G}_5) = \dot{n}_{O_2}(\Delta H_5, \Delta G_5) / \left(\dot{m}_{ref} c_{p,f} T_\infty\right)$.

The enthalpy change during anode and cathode reaction are given by respectively, by $\Delta H_3 = \sum_{products}\left[\upsilon_i H_i(T_i)\right] - \sum_{reac\,tan\,ts}\left[\upsilon_i H_i(T_i)\right]$ while $W_{e3} = -\Delta G_3$ and $\Delta H_5 = \sum_{products}\left[\upsilon_i H_i(T_i)\right] - \sum_{reactants}\left[\upsilon_i H_i(T_i)\right]$ while $W_{e5} = -\Delta G_5$.

The enthalpy of formation are obtained from tabulated values [69-70] at T_2 for $H_{2(g)}$, T_4 for $OH^-_{(aq)}$ and T_3 $H_2O_{(l)}$ (Eq. 2.69); T_6 for $O_{2(g)}$ and T_4 for the reactant $H_2O_{(l)}$ and T_5 for $OH^-_{(aq)}$ (Eq. 2.7), both cases at 1 atm.

The Gibbs free energy change is defined $\Delta G = \Delta G^0 + \bar{R}T \ln Q$ where $\Delta G^0 = \Delta H^0 - T\Delta S^0$. The reaction quotient Q is given by $Q_3 = \left\{ \left[OH^-\right]^2 p_{H_2} \right\}^{-1}$ and $Q_5 = \left[OH^-\right]^2 / p_{O_2}^{1/2}$, where $p_{H_2} = p_{2,out}$ and $p_{O_2} = p_{6,out}$.

2.2.2.4 Electrolyte and Membrane (CV4)

In our study, the electrolyte is an alkaline solution of KOH and the membrane is made by cellulose (chromatography paper). The molar concentration of KOH, [KOH], can be obtained from the weight percentage of KOH in solution, y.

$$[KOH] = \frac{(y/100)\rho_{sol}}{M_{KOH}} \tag{2.79}$$

where ρ_{sol} is the density of the solution in terms of y [78] and M_{KOH} the KOH molecular weight.

The energy balance for the CV4 is

$$\tilde{Q}_4 + \tilde{H}(\theta_5)_{OH^-} - \tilde{H}(\theta_4)_{OH^-} + \tilde{H}(\theta_3)_{H_2O} - \tilde{H}(\theta_4)_{H_2O} = 0 \tag{2.80}$$

where $\tilde{Q}_4 = -\tilde{Q}_{34} + \tilde{Q}_{w4} + \tilde{Q}_{45} + \tilde{Q}_{4ohm}$.

2.2.3 Electrochemical Model, Power and Efficiency

Based on the electrical conductivities and geometry of each compartment the electrical resistances $\beta(\Omega)$, are given by

$$\beta_i = \frac{\xi_i}{\tilde{A}_s V_T^{1/3} \sigma_i (1-\phi_i)}, \qquad i = 1,2,6,7 \ (\phi_1, \phi_7 = 0) \tag{2.81}$$

$$\beta_i = \frac{\xi_i}{\tilde{A}_s V_T^{1/3} \sigma_i \phi_i}, \qquad i= 3, 4, 5, \ (\phi_4 = 1) \tag{2.82}$$

where $\sigma_i = \sigma_{sol}$ for i =3,4 and 5.

Similarly the PEMFC model, the appropriate figure of merit for evaluating the performance of a fuel cell is the polarization curve, i.e., the fuel cell total potential as a function of current. The dimensionless potential ($\tilde{V}$) defined previously for PEMFC are also valid for AMFC analysis. The dimensionless actual potential $\tilde{V}_i$ is an accumulated result of dimensionless irreversible anode electrical potential $\tilde{V}_{i,a}$, dimensionless irreversible cathode electrical potential $\tilde{V}_{i,c}$, and the dimensionless ohmic loss $(\tilde{\eta}_{ohm})$ in the space from CV1 to CV7, i.e.,

$$\tilde{V}_i = \tilde{V}_{i,a} + \tilde{V}_{i,c} - \tilde{\eta}_{ohm} \tag{2.83}$$

The ohmic loss $\tilde{\eta}_{ohm}$ is estimated by

$$\tilde{\eta}_{ohm} = \frac{I}{V_{ref}} \sum_{i=1}^{7} \beta_i \tag{2.84}$$

The reversible electrical potential at the anode is given by the Nernst equation [55],

$$V_{e,a} = V_{e,a}^{o} - \frac{\bar{R}T_3}{nF} \ln Q_3 \tag{2.85}$$

where $V_{e,a} = \Delta G_3 / (-nF)$ and $V_{e,a}^{o} = \Delta G_3^{o} / (-nF)$; n is the equivalent electron per mole of reactant, eq mol^{-1} and F the Faraday constant. The potential loss (η_a) due to charge transfer is obtained implicitly from the Butler-Volmer equation for a given current I [58-59]

$$\frac{I}{A_{3,wet}} = i_{o,a} \left\{ \exp\left[\frac{(1-\alpha_a)\eta_a F}{\bar{R}T_3} \right] - \exp\left[-\frac{\alpha_a \eta_a F}{\bar{R}T_3} \right] \right\} \tag{2.86}$$

where α_a is the anode charge transfer coefficient, and $i_{o,a}$ is the anode exchange current density. The potential loss due to mass diffusion is [74-75]:

$$\eta_{d,a} = \frac{\bar{R}T_3}{nF}\ln\left(1 - \frac{I}{A_{3,wet} i_{Lim,a}}\right) \tag{2.87}$$

where, from Eq. (2.65):

$$i_{lim,a} = \frac{p_f D_2 nF}{M_{H_2} L_2 R_f \theta_2 T_\infty} \tag{2.88}$$

The resulting electrical potential at the anode is $\tilde{V}_{i,a} = \tilde{V}_{e,a} - \tilde{\eta}_a - \left|\tilde{\eta}_{d,a}\right|$, where we have taken the absolute value of $\eta_{d,a}$ because $\eta_{d,a} < 0$.

Similarly, the actual cathode potential is $\tilde{V}_{i,c} = \tilde{V}_{e,c} - \tilde{\eta}_c - \left|\tilde{\eta}_{d,c}\right|$ and the reversible electrical cathode potential is $V_{e,c} = V^o_{e,c} - \left(\bar{R}T_5/nF\right)\ln Q_5$, where and $V^o_{e,c} = \Delta G^o_5/(-nF)$. The Butler-Volmer equation for calculating the cathode side overpotential η_c is $I/A_{5,wet} = i_{o,c}\left[\exp\left((1-\alpha_c)\eta_c F/\left(\bar{R}T_5\right)\right) - \exp\left(-\alpha_c \eta_c F/\left(\bar{R}T_5\right)\right)\right]$. The cathode mass diffusion depleting overpotential is $\eta_{d,c} = \left\{\bar{R}T_5/(nF)\right\}\ln\left(1 - I/\left(A_{5,wet} i_{Lim,c}\right)\right)$, and the cathode limiting current density is $i_{lim,c} = 2p_{ox} D_6 nF/\left(M_{O_2} L_6 R_{ox} \theta_6 T_\infty\right)$.

The pumping power $\tilde{W}_p$ is required to supply the fuel cell with fuel and oxidant. Therefore the total net power (available for utilization) of the fuel cell is

$$\tilde{W}_{net} = \tilde{W} - \tilde{W}_p \tag{2.89}$$

where $\tilde{W} = \tilde{V}_i \tilde{I}$ is the total fuel cell electrical power output , and

$$\tilde{W}_p = \psi_f S_f \frac{\theta_1}{P_1}\Delta P_1 + \psi_{ox} S_{ox} \frac{\theta_7}{P_7}\Delta P_7 \tag{2.90}$$

$$S_i = \frac{m_{ref} T_\infty R_i}{V_{ref} I_{ref}}, \quad i = f,ox \tag{2.91}$$

The ideal efficiency or maximum theoretical efficiency is expressed as

$$\eta_i = \frac{W_{e3} + W_{e5}}{\Delta H_3 + \Delta H_5} \tag{2.92}$$

Using the dimensionless variables we can re-write the ideal efficiency as

$$\eta_i = \frac{\Delta \tilde{G}_3 + \Delta \tilde{G}_5}{\Delta \tilde{H}_3 + \Delta \tilde{H}_5} \tag{2.93}$$

The first law efficiency is given as

$$\eta_I = E \frac{\tilde{W}}{\Delta \tilde{H}_3 + \Delta \tilde{H}_5} \tag{2.94}$$

where $E = \frac{V_{ref} I_{ref}}{\dot{m}_{ref} c_{p,f} T_\infty}$.

The second law efficiency is defined as the ratio of the actual power to the reversible power of the fuel cell and can be expressed as

$$\eta_{II} = E \frac{\tilde{W}}{\Delta \tilde{G}_3 + \Delta \tilde{G}_5} \tag{2.95}$$

The net efficiency of the fuel cell is

$$\eta_{net} = E \frac{\tilde{W}_{net}}{\Delta \tilde{H}_3 + \Delta \tilde{H}_5} \tag{2.96}$$

CHAPTER THREE

NUMERICAL RESULTS AND EXPERIMENTAL VALIDATION OF POLYMER ELECTROLYTE MEMBRANE FUEL CELL (PEMFC) MODEL

An experimental rig was built in the laboratory to produce the necessary experimental data to perform the experimental validation of the numerical results obtained with the mathematical model presented in the Chapter 2. Figure 3.1 shows two photos of the experimental set of single PEMFC's utilized in this study. Ten low power (1 – 2 W) single PEMFC's manufactured by Schatz Energy Research Center, SERC [79] were assembled on equally spaced supports, as shown in Fig. 3.1.

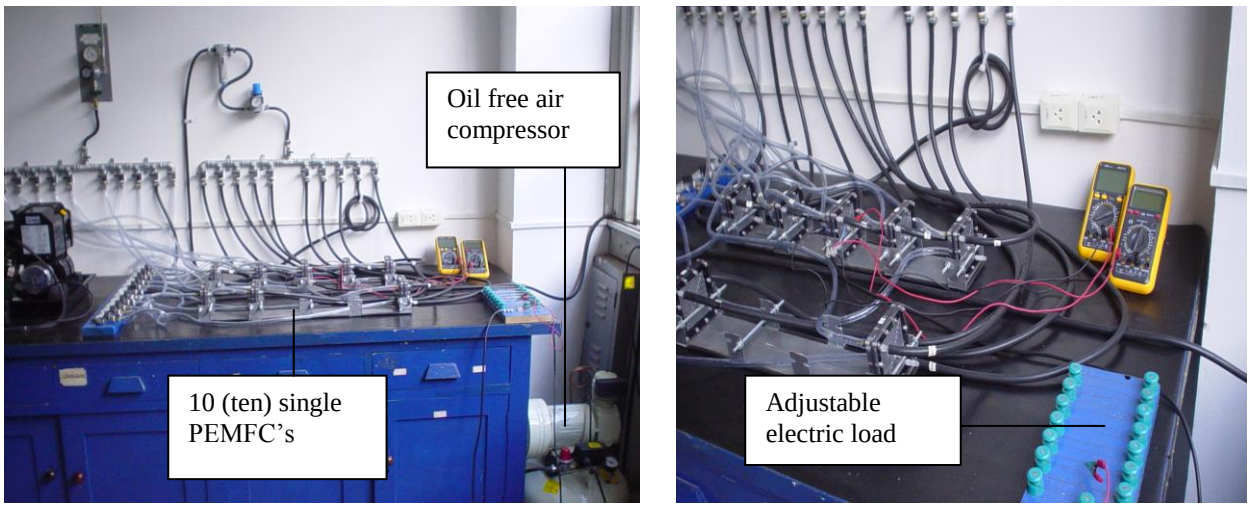

(a) (b)

Figure 3.1: (a) ten single PEMFC's experimental setup and air compressor, and (b) single PEMFC detail and adjustable electric load.

On the inferior right side of Fig. 3.1a, it is shown the dental oil free air compressor utilized to feed the system. The H_2 and air feed systems with respective manometers were placed on the wall, and from them a system of hoses and valves distribute the fuel and oxidant supply to the cells. An adjustable low power electric load was built with nickel-chrome alloy wire, as shown in Fig. 3.1b.

The SERC single fuel cell internal structure was characterized through direct measurements of the length, width, and thickness of the internal parts. L_1 = 1.55mm, L_2 = 0.45 mm, L_3 = 0.005 mm, L_4 = 0.045mm, L_5 = 0.005 mm, L_6 = 0.45mm, L_7 = 1.55mm. The dimensionless

parameters were then calculated for the SERC single PEMFC, obtaining $\xi_1/\xi_x = \xi_7/\xi_x = 0.38$, $\xi_2/\xi_x = \xi_6/\xi_x = 0.111$, $\xi_3/\xi_x = \xi_5/\xi_x = 0.0025$, $\xi_4/\xi_x = 0.013$, $\xi_x = 0.1504$, $\xi_y = 2.5783$ and $\xi_z = 2.5783$, $\xi_t = 0.00258$, $\xi_c = 1.2891$, with $V_T = 1.95867 \times 10^{-5} m^3$. A schematic of the experimental set up is shown in the Fig. 3.2.

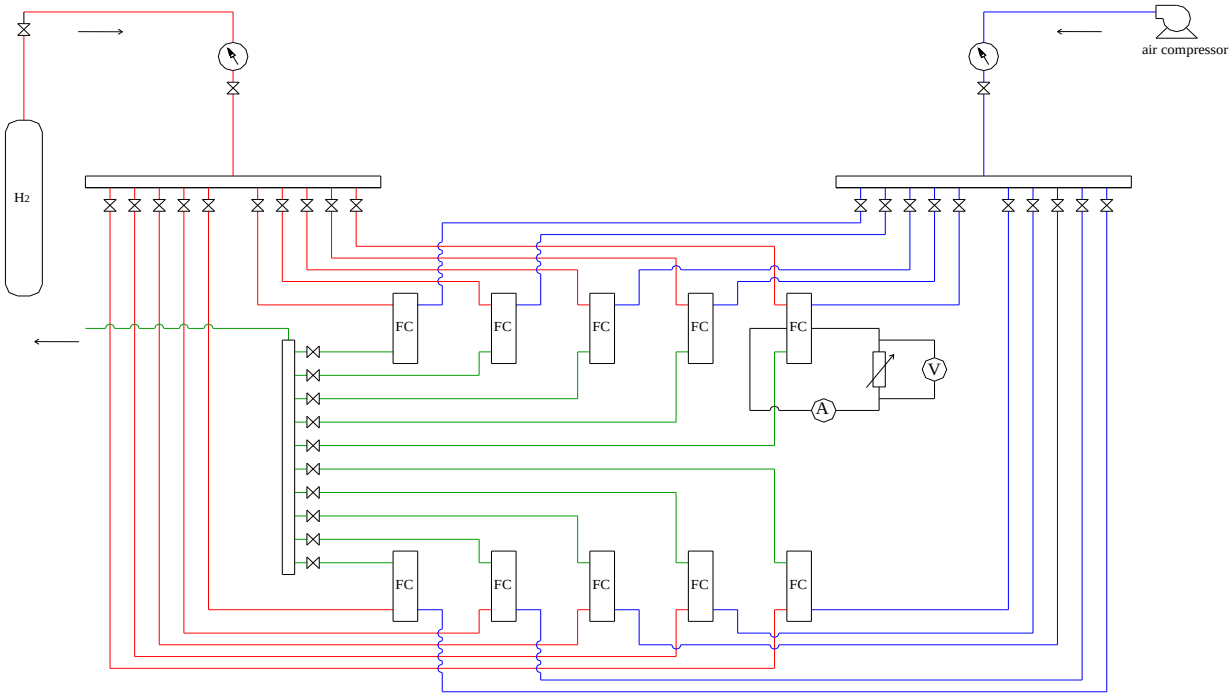

Figure 3.2: Schematic of the experimental set up for PEMFC.

3.1 Physical Properties

Besides the single PEMFC internal and external geometry, the mathematical model needs information on the actual physical properties of the manufacturing materials. For that, the Membrane Electrolyte Assembly (MEA) of one of the cells utilized in the experiments was characterized in the laboratory. The MEA is composed by the polymeric membrane (Nafion 117) coated with carbon, the two reaction layers and the two diffusive layers, according to the following procedures for the property to be determined.

a) density

The densities of the membrane and of the diffusive layer were measured using a 50 ml picnometer, with a nominal uncertainty of $\pm 0.019\%$. The experiments were carried out according to ASTM D-792-00 [65].

b) porosity

Porosity was evaluated following a gravimetrical study regarding solvent absorption. The material was dried at 75ºC overnight, then weighed to obtain its dry weight (w_{dry}), and immersed in distilled water for 24 hours to reach equilibrium. After that, the saturated membranes were carefully weighed to obtain the wet weight (w_{wet}). The scale utilized in the procedure had a 4 decimal digit precsion, with a nominal uncertainty of $\pm 0.02\%$.

Membrane porosity (ϕ) at room temperature was then calculated using the following equation [34,35].

$$\phi = \frac{(w_{wet} - w_{dry}) \cdot \rho_{dry}}{(w_{wet} - w_{dry}) \cdot \rho_{dry} + (w_{dry} \cdot \rho_{sol})} \tag{3.1}$$

where ρ_{dry} is the density of the material after drying and ρ_{sol} is the solution density. The tested materials were the membrane, the membrane covered with carbon and the diffusive layer.

c) specific heat

The specific heat was measured by power compensated differential scanning calorimetry (DSC) - TA Instruments Model 20-10 [68], with a sensitivity of $\pm 2.5\%$ from -100 to 500ºC and nominal uncertainty of $\pm 1\%$. DSC analysis was carried out with a 10-mg sample enclosed in an aluminum pan, with a heating and a cooling rate of 10ºC/min under Nitrogen atmosphere. The specific heat of the membrane is 1.6 J/gºC. The membrane specific heat (c_p) was evaluated using the output curve of the DSC (heat flow, temperature and time data – Fig. 3.3), based on the enthalpy gradient calculated at a certain temperature range, according to the equation below [81]

$$\Delta H = m_p \cdot c_p \cdot \Delta T \tag{3.2}$$

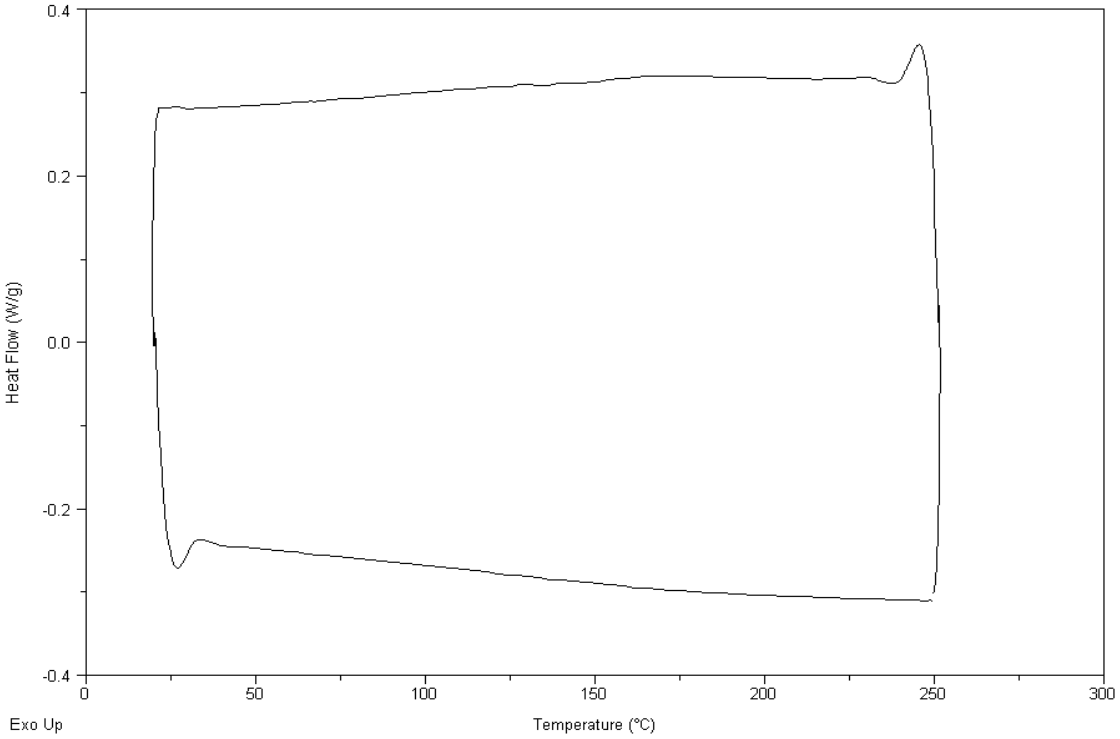

Figure 3.3: Differential scanning calorimetry (DSC) output curve for the tested 10-mg membrane sample.

d) *electrical conductivity*

The two-probe method was used to determine the area resistance of the sample with a multimeter ET 2082A. Then, taking into account 2nd Ohm's Law, the electrical conductivity of the diffusive layer at 17 ºC and 20 % of relative humidity was calculated. Electrical conductivity of the diffusive layer in the through-the-thickness direction was evaluated in a potentiostat with an impedance spectroscopy cell (Autolab PGSTAT 30), with a nominal uncertainty of $\pm 0.2\%$.

All the results obtained for the measured properties in the laboratory are shown in Table 3.1. Table 3.2 summarizes the geometric features and physical properties of the single PEMFC simulated in this study.

Table 3.1: Measure properties of SERC single PEMFC.

	Membrane (Nafion)	Membrane with carbon (reactive layer)	Diffusive layer
Density (ρ) Dry condition	3.28 g/cm^3	1.91 g/cm^3	0.58 g/cm^3
Porosity (ϕ)	0.285 or 28.5%	0.1802 or 18%	0.0085 or 0.85%
Electrical conductivity (σ)	Eq (2.31)		59.4 S/cm (2-point in-plane) 85.7 S/cm (through-the-thickness)

The remaining necessary data were taken from the technical literature [66, 71-75,82]. Since the values for the anode and cathode exchange current densities $(i_{0,a}, i_{0,c})$ are commonly reported in a wide range [75], the values adopted in this study were determined by the solution of an inverse problem of parameter estimation.

The single PEMFC net power output, defined by Eq. (2.39), depends on the internal structure and the external shape of the fuel cell. As soon as the physical values and a set of geometric internal and external parameters are known, the mathematical model allows the computation of the total net power of the fuel cell, $\tilde{W}_{net}$. In the case of the present study, such set is given by Table 3.2.

Table 3.2: Physical properties used in the experimental validation of the single PEMFC mathematical model.

$B = 0.156$	$R_{ox} = 0.2598$ kJ kg^{-1} K^{-1}
$c_{p,f} = 14.95$ kJ kg^{-1} K^{-1}	$T_f, T_{ox}, T_\infty = 298.15$ K
$c_{p,ox} = 0.91875$ kJ kg^{-1} K^{-1}	$U_{wi} = 50$ W m^{-2} K^{-1}, i = 1 to 7
$c_{v,f} = 10.8$ kJ kg^{-1} K^{-1}	$V_{ref} = 1$ V
$c_{v,ox} = 0.659375$kJ kg^{-1} K^{-1}	$V_T = 1.95867\times10^{-5}$ m^3
$(i_{0,a}, i_{0,c}) = (0.3, 0.003)$ A m^{-2}	$V_{T,ref} = 10^{-5}$ m^3
$I_{ref} = 1$ A	$\alpha_a, \alpha_c = 0.75$
$k_f = 0.2$ W m^{-1} K^{-1}	$\zeta_1, \zeta_7 = 2$
$k_{ox} = 0.033$ W m^{-1} K^{-1}	$(\lambda_a, \lambda_c) = (5, 7)$
$k_p = 0.21$ W m^{-1} K^{-1}	$\mu_1 = 10^{-5}$ Pa.s
$K_2, K_6 = 4 \times 10^{-14}$ m^2	$\mu_7 = 2.4\times10^{-5}$ Pa.s
$K_3, K_5 = 4 \times 10^{-16}$ m^2	$\sigma_1, \sigma_7 = 1.388\times10^{6}\ \Omega^{-1}$m^{-1}
$\dot{m}_{ref} = 10^{-4}$ kg s^{-1}	$\sigma_2, \sigma_6 = 8570\ \Omega^{-1}$m^{-1}
$p_f = 0.12$ MPa	$\phi_2, \phi_6 = 0.0085$
$p_{ox}, p_\infty = 0.1$ MPa	$\phi_3, \phi_5 = 0.1802$
$q = 1.5$	$\phi_4 = 0.285$
$R_f = 4.157$ kJ kg^{-1} K^{-1}	

3.2 Numerical Results and Experimental Validation

The numerical simulation of the single PEMFC is performed by solving Eqs. (2.7), (2.18), (2.20), (2.23), (2.25), (2.26), (2.27) and (2.28), which form a system of nine algebraic equations. The unknowns are θ_i and P_i, i.e., the temperatures in the seven control volumes, and the gas pressures in CV2 and CV6. Once the temperatures and pressures are known, the electrical potentials and power are calculated for any assumed current level.

Pressures are related to temperatures via Eq. (2.18). The system reduces to seven nonlinear algebraic equations, in which the unknowns are the temperatures of the seven control volumes. This system was solved with a Fortran code, using a quasi-Newton method [83], where a tolerance for the norm of the residual vector less or equal to 10^{-6} was considered to obtain a converged solution.

For obtaining the experimental results in the present study, the fuel cells were operated at a hydrogen pressure of 2.5 psi and at a very low flow of atmospheric air (compressed air from a dental oil-free compressor). The air-flow although not measured was high enough to maintain a steady current output but not too high as to dry out the interior of the cell (water condensation was visible). A variable electrical resistance made from high resistivity Ni-Cr resistance wire was used as variable electrical load (Fig. 3.1b). It was set as to render the current output needed to each experiment.

The experimental validation was based on direct measurements of the current and voltage produced by the fuel cell. In order to produce the cell polarization curve, the adjustable load resistance was reduced from open circuit $(\beta_{load} \to \infty, I = 0)$ to short circuit $(\beta_{load} = 0)$, where the measured current was approximately 3.1 A. Voltage and current measurements were performed for each of the ten cells with a digital multimeter ICEL-MD-6110.

Ten runs were conducted, the precision limit for each voltage and power point was computed as two times the standard deviation of the average value of the ten runs obtained, [84].

In the numerical simulations, the cells electrical and net power were calculated by starting from open circuit $(\tilde{I} = 0)$, and proceeding with increments of $(\Delta\tilde{I} = 0.1)$ until the electrical current reached 3.1 A, i.e., the highest value of current experimentally measured in the laboratory.

This procedure is illustrated in Fig. 3.4. According to the model, the actual open circuit voltage is equal to the reversible cell potential, because it has been assumed that no losses result from species crossover from one electrode through the electrolyte, and from internal currents. The total polarization is the sum of the electrical potential produced at the anode and cathode, $\tilde{V}_{i,a}$ and $\tilde{V}_{i,c}$. In a PEMFC, the electrical potential produced at the anode is negative. Conversely, the electrical potential produced at the cathode is positive. The sum of such potentials minus the potential losses the cell is the total fuel cell potential, $\tilde{V}_i$.

The change in the Gibbs free energy of reaction decreases as the temperature increases. Therefore, according to Eq. (2.35), the reversible electrical potential decreases as the temperature increases, and this happens when the current increases.

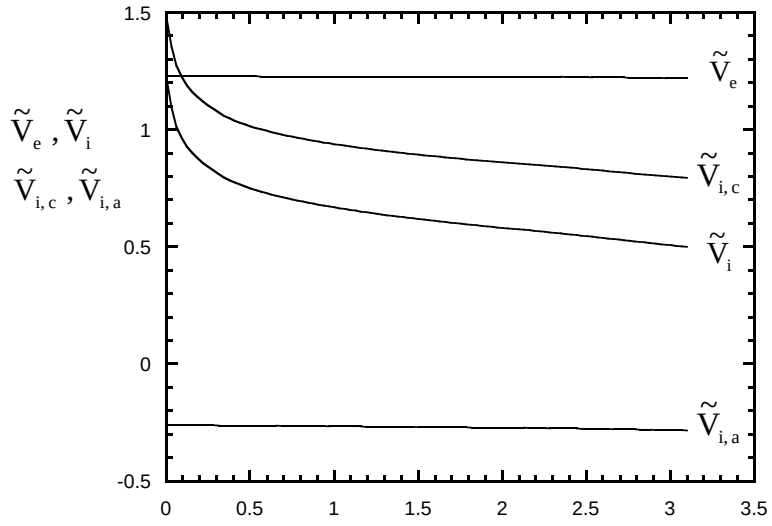

(a)

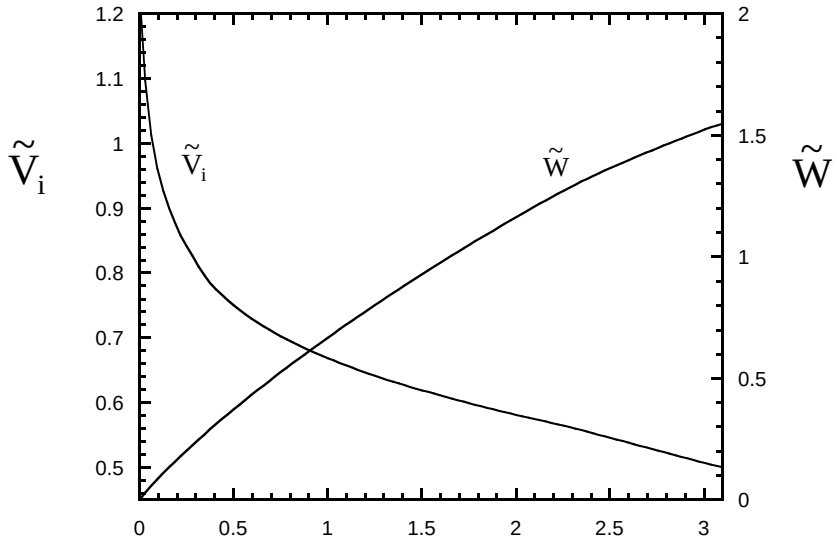

(b)

Figure 3.4: (a) Total cell reversible, total cell irreversible, cathode and anode numerically simulated potentials and (b) the numerically simulated total cell irreversible potential and output power.

Figure 3.4a shows the polarization curves and all those trends until the cells reach the maximum current measured experimentally $(I = 3.1\,A)$.

Figure 3.4b shows the simulation results for the irreversible cell potential output and the electrical power produced. Since the tested cells operate at low currents, pressure drops are negligible in the gas channels, therefore, in the tested cells, $\tilde{W} \cong \tilde{W}_{net}$.

The numerical voltage results are compared with the experimentally measured data in Fig. 3.5. Error bars were placed in the experimental points. The precision limit was computed as two times the standard deviation of the average value of the ten runs obtained. In this graph, it is possible to verify that the numerical simulation results are in good quantitative and qualitative agreement with the measured polarization curve. The numerical results are all within the range established by the error bars, except in the beginning of the current range $(\tilde{I} \le 0.6)$, because the losses from species crossover through the electrolyte, and from internal currents are not considered in the mathematical model. However, in practice, fuel cells are expected to operate at higher currents, where maximum power occurs; therefore the model is expected to provide accurate output voltage results at that current range of greater interest.

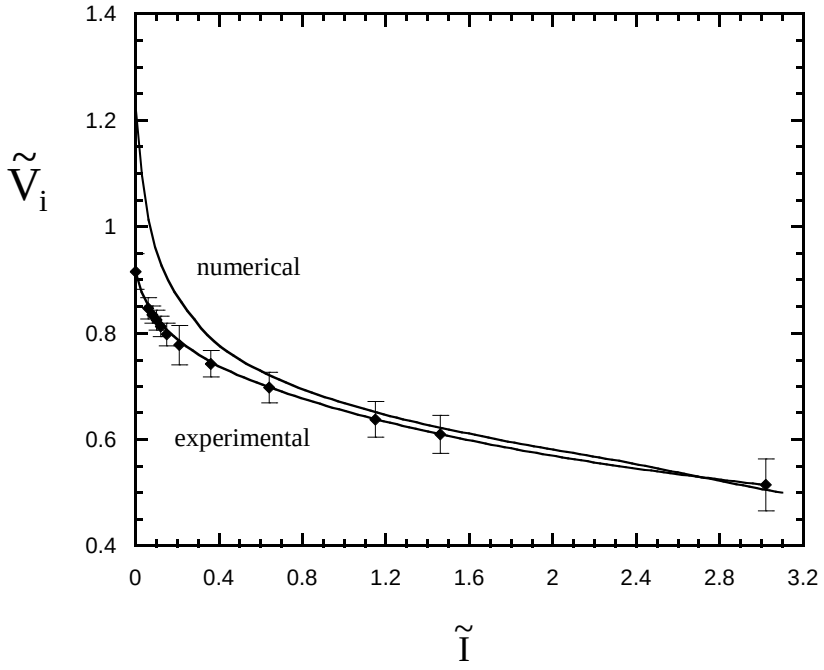

Figure 3.5: The comparison between the numerically and experimentally obtained total cell irreversible potential.

Figure 3.6 depicts the comparison of the cells output power between the obtained numerical and experimental results. It is observed that the numerical simulation results fall within the range established by the error bars in the entire current range analyzed in the experiments $(0 \le I \le 3.1\,A)$. This shows good quantitative and qualitative agreement between numerical and experimental results.

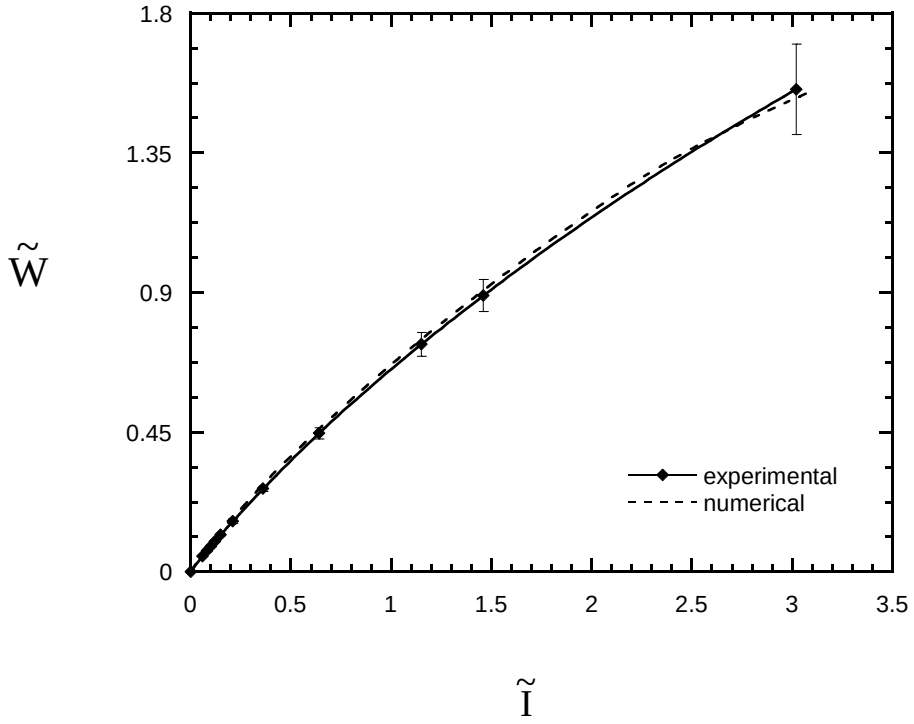

Figure 3.6: The comparison between the numerically and experimentally obtained total cell output power.

Since the ideal efficiency is proportional to Gibbs free energy, any decrement in the Gibbs free energy caused by the increment of the temperature will be expressed in the ideal efficiency. The Fig. 3.7 shows that the ideal efficiency decreases slightly as the current increases.

Both, the first law and the second law efficiency decreases monotonically as the current increases, but their maximum values ($\tilde{I} = 0$) are different. The maximum first law efficiency is equal the ideal efficiency at open circuit. The second law efficiency has its maximum equal to 1, meaning no losses (reversible case). The net efficiency is equal to the first law efficiency due to low current regime that this fuel cell operates. At low currents, the pressure drop in the gas channels is very low, making the pumping power be negligible, $\tilde{W}_p \cong 0$.

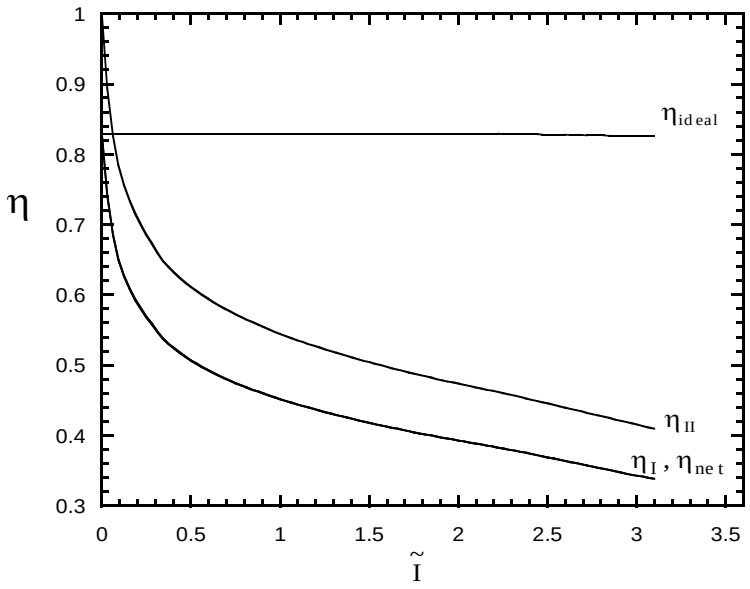

Figure 3.7: The ideal, first law, second law and net efficiencies for the SERC PEMFC.

CHAPTER FOUR

NUMERICAL RESULTS AND EXPERIMENTAL VALIDATION OF ALKALINE MEMBRANE FUEL CELL (AMFC) MODEL

The previous chapter shows the results and preliminary conclusions obtained from the development of a simulation model for PEMFC that contemplates variation of manufacturing materials physical properties, operation and design parameters. The simulation model was validated experimentally considering the temperature as space and current dependent. The experimental validation of the PEMFC model presented was considered a learning process that allowed for understating fuel cell physics concepts, components and operation. Once these first steps have been successfully accomplished we applied the acknowledge acquired on the development of a simulation model for AMFC.

In this chapter we will present the numerical results for AMFC and the experimental results obtained using a prototype of a single fuel cell built in our laboratory.

4.1 Alkaline Membrane Fuel Cell Prototype

The maturation of the knowledge on the subject allowed the development in the laboratory of an AMFC prototype using celluloses based membrane (which replaced the polymeric electrolyte membrane of the PEMFC), platinum-carbon electrodes and as electrolyte, alkaline solution of potassium hydroxide (KOH), as it will be described in the following sections. With respect to current alkaline fuel cells, the herein proposed alkaline membrane fuel cell has the advantage of a solid membrane made by cellulose instead of only a liquid electrolyte and does not require elaborated seals to operate or a pumping system to keep the electrolyte flowing through the fuel cell.

4.1.1 Bipolar Plate

The bipolar plates consist of two plates 120 mm x 120 mm made of brass with 34 channels with 1 mm width, 2 mm depth and 80 mm long each, as can be seen in the Fig. 4.1. The Fig. 4.2 is a picture of bipolar plates where its details and channels can be seen. Each

bipolar plate has a socket head cap screw that works as a positive pole when connected to the positive plate (cathode) or negative pole when connected to the negative plate (anode). These screws connect the fuel cell to the external circuit.

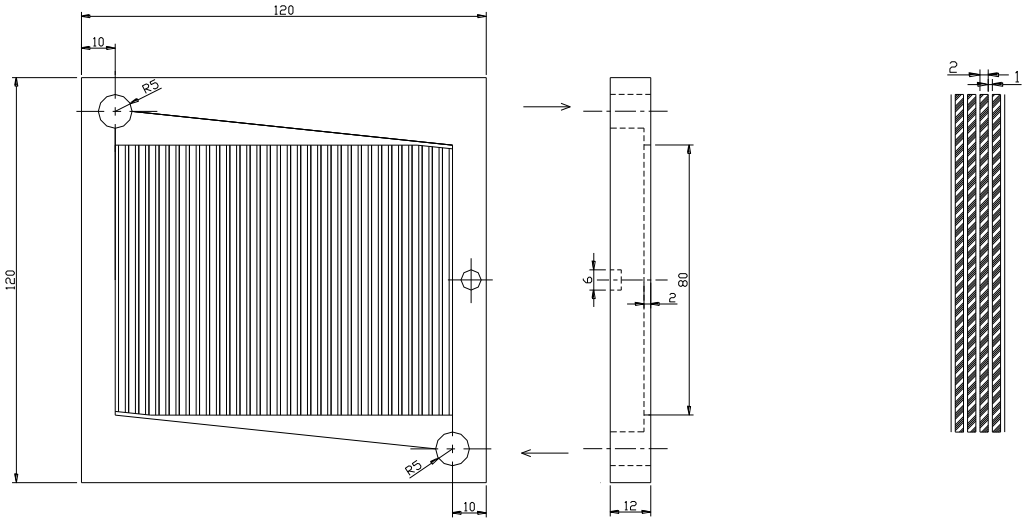

(a) (b)

Figure 4.1: Drawing of the alkaline fuel cell prototype. (a) front and side view of the fuel cell; (b) gas channels. (unit: mm)

4.1.2 Membrane

The membrane is the medium where the liquid electrolyte will be confined. In our prototype we used WHATMAN ® Chromatography paper 31ET Chr, purchased from BioAmerica Inc. Chromatography separates the components of a mixture by their distinctive attraction to a mobile phase (liquid solvent) and the stationary phase (paper). The affinity between the paper and the liquid is a very important property of the membrane since the liquid is supposed to be confined in the porous of the paper and not leave the fuel cell with the products of the electrochemical reactions. The paper provides mechanical strength to the electrolyte, minimizes the distance between the electrodes while preventing shorts circuits and prevents crossover of reactant gases through the electrolyte.

The thickness of the membrane is 0.50 mm. The specifications of the membrane given by the manufacturer are shown in Table 4.1.

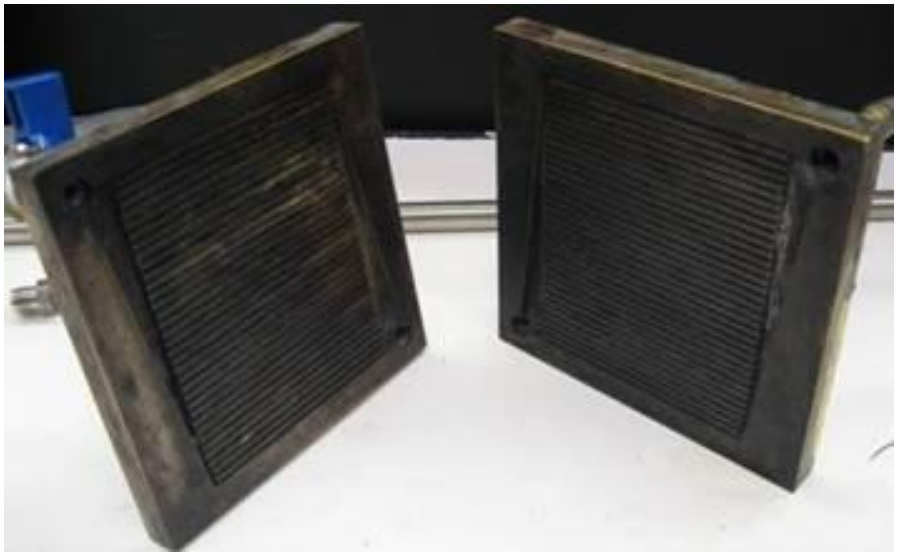

Figure 4.2: Picture of the bipolar plates.

Table 4.1: Specifications of the membrane. [1] Air flow rate determined with Gurley Densometer with 5 oz abd 1 in^2 test area. [2] Grammage defines weight per unit area, preferably of circular sheets of area 100 cm^2 . [3] Wet burst as well as dry burst is determined with filter test area of 1 in^2 which is made to burst by applying an increasing pressure.

Gurley[1] (s/300ml/in^2)	15
Grammage[2] (g/cm^2)	192
Wet burst [3] (ins H_2O)	12
Dry burst [3] (psi)	18

The Fig 4.3 shows pictures of dry and wet membrane with the alkaline solution after run an experiment and the Fig.4.4 and 4.5 show SEM (scanning electron microscope) images of the dry membrane.

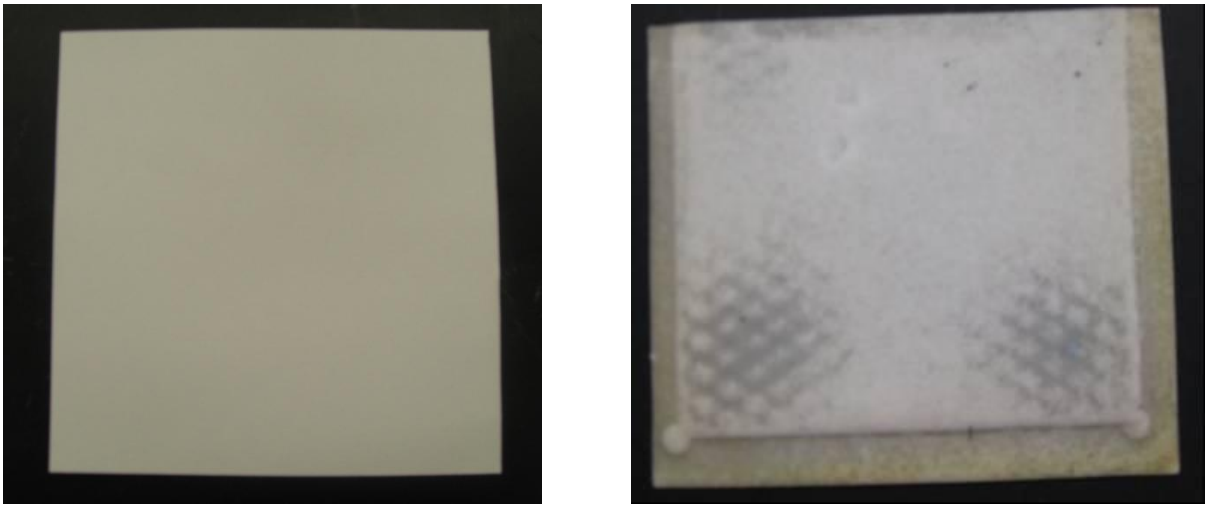

(a) (b)

Figure 4.3: (a) Dry membrane; (b) Membrane wet with alkaline solution.

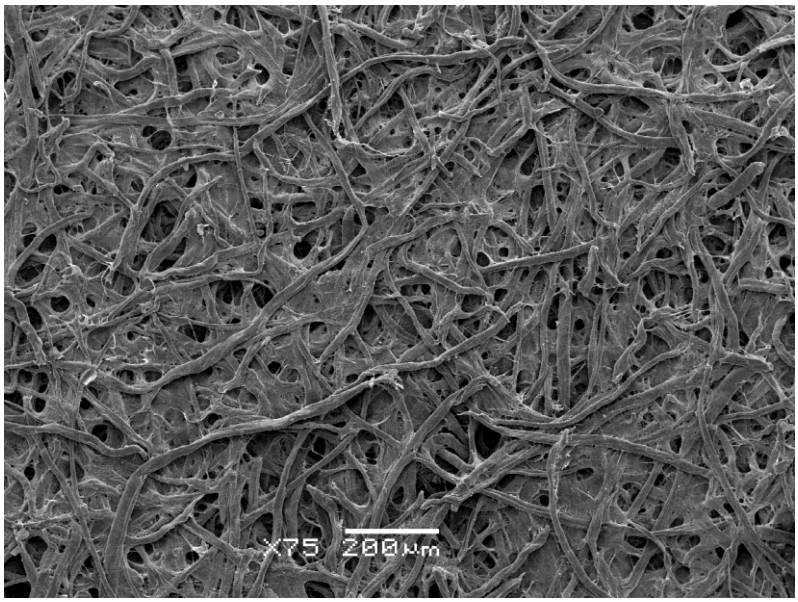

Figure 4.4: SEM image of the dry membrane.

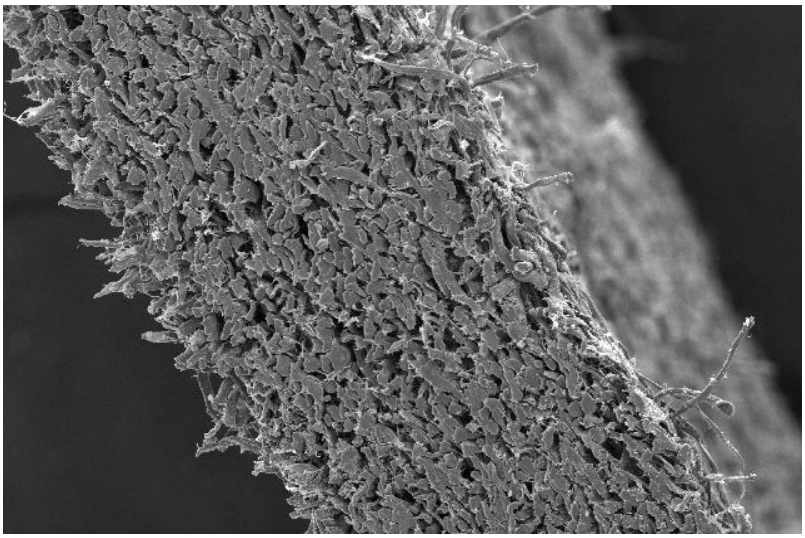

Figure 4.5: SEM image of a cross section of dry sample of the membrane.

4.1.3 Electrode

The electrode used to obtain experimental polarization curve was a low temperature ELAT ® GDE (Gas diffusion electrode) microporous layer including 5g/m^2 Pt electrode on woven web, with thin layer on backside, with standard ionomer application manufactured by BASF ®. The Fig.4.6 shows the electrode used.

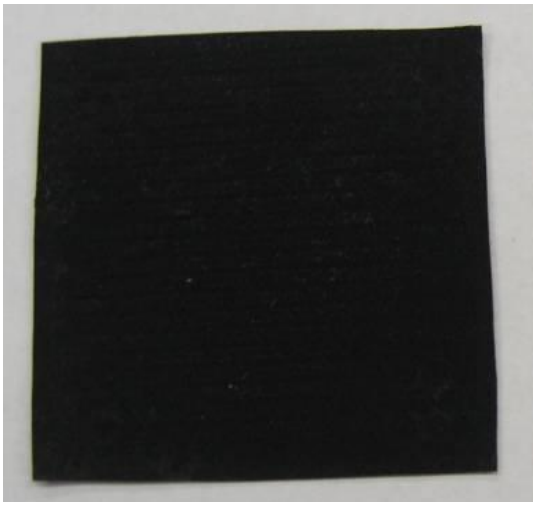

Figure 4.6: Platinum-Carbon based electrode.

The electrode has a hydrophobic and a hydrophilic side. The Fig. 4.7 shows a SEM image of the hydrophobic side, which is the gas diffusion layer (CV2 and CV6); this side of the electrode is in contact to the gas channels (bipolar plate). The Fig. 4.8 shows a SEM image of the hydrophilic side of the electrode, which is the reaction layer (CV3 and CV5), this side is in contact to the membrane. We can see that the hydrophobic and hydrophilic sides have different aspects. The hydrophobic side is rougher than the hydrophilic side. The morphology cracked mud surface of the hydrophilic side is due the catalyst coating (Platinum).

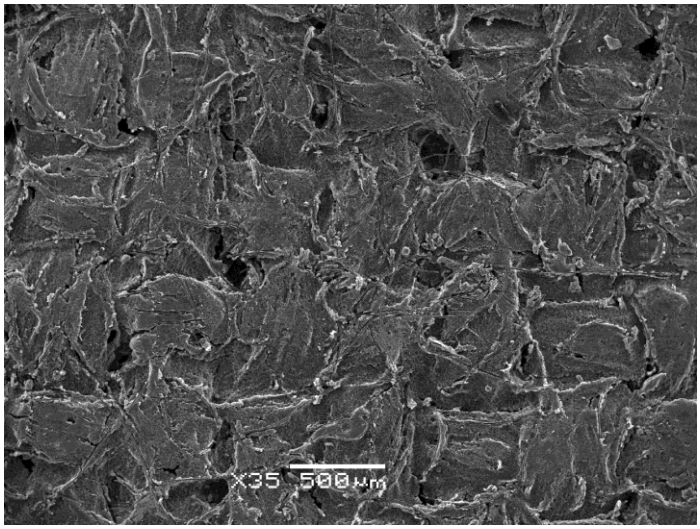

Figure 4.7: SEM image of the electrode – hydrophobic side (diffusion layer).

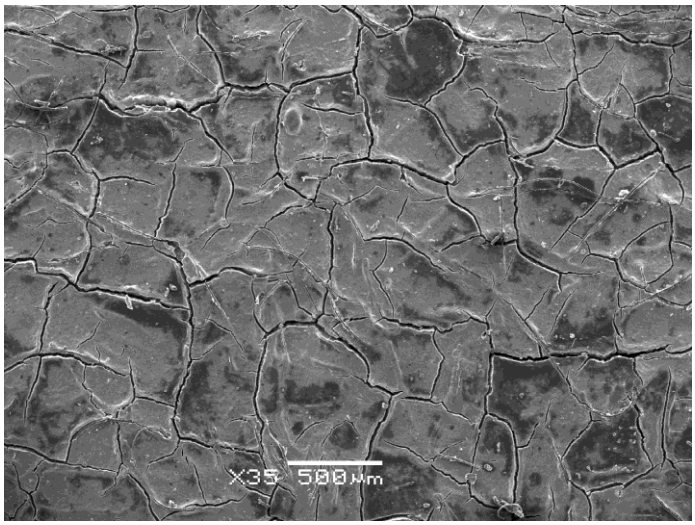

Figure 4.8: SEM image of the electrode – hydrophilic side (reactive layer).

The Figure 4.9 shows the cross section SEM image of the electrode, we can clearly see that it is composed of two distinct layers. The darker layer one on top is the reactive layer, where the catalyst is present and on the bottom is the diffusion layer. We can also see that the reactive layer is thinner that diffusion layer.

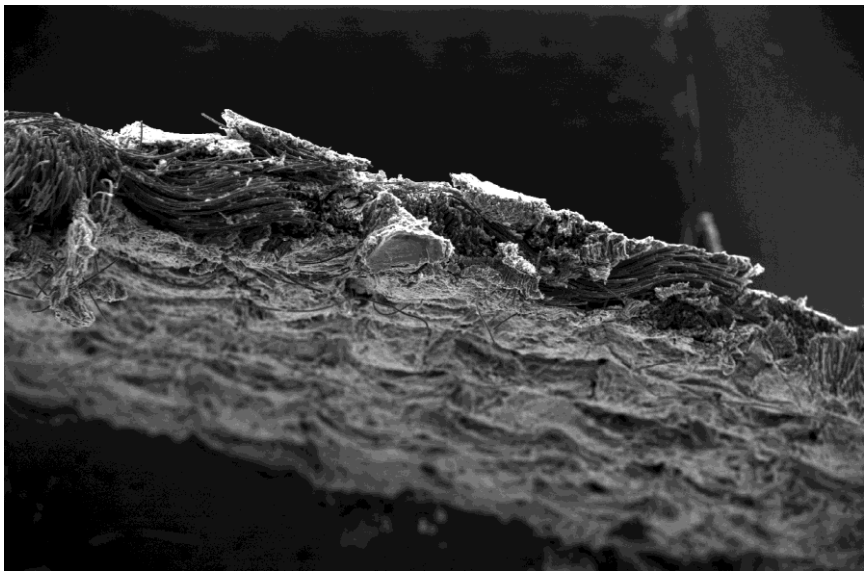

Figure 4.9: SEM image of a cross section of the electrode. On the bottom is the diffusion layer (hydrophobic) and on top is the reactive layer (hydrophilic).

4.1.4 Membrane Electrode Assembly (MEA)

The assembling procedure of the prototype was the following: the hydrophobic side of the electrode is placed facing the bipolar plate (gas channels). We can find out which side is hydrophobic or hydrophilic by the roughness of the faces of the electrode, the hydrophobic side is rougher than the hydrophilic side. Another way to do it is to put a drop of water on one of the faces. The water will slip more easily on the face that is hydrophobic.

After the membrane is immersed in the alkaline solution we remove the excess of the solution holding the membrane with tweezers for a few seconds and letting the excess to drip off through the edges of the membrane.

The wet membrane is put on top of the electrode (facing the hydrophilic side of the electrode) and on top of the membrane we put the other electrode, making sure that the hydrophilic side of the electrode is facing the membrane.

We have now a “sandwich”, electrode-membrane-electrode, what is called *membrane electrolyte assembly (MEA)*. The second bipolar plate is then placed on top of the whole structure. A bench vise was used to hold and supply sufficient pressure on the whole structure, as can be seen in the Fig. 4.10. To keep the pressure needed to maintain all the internal components connected without any leaking, the fuel cell was put between two “H” shape metal bars (one in each side) that were attached to each other with bolts. A thin piece of rubber was used as an electric insulation between the “H” bars and the bipolar plates. Fig. 4.11 shows the finished alkaline fuel cell.

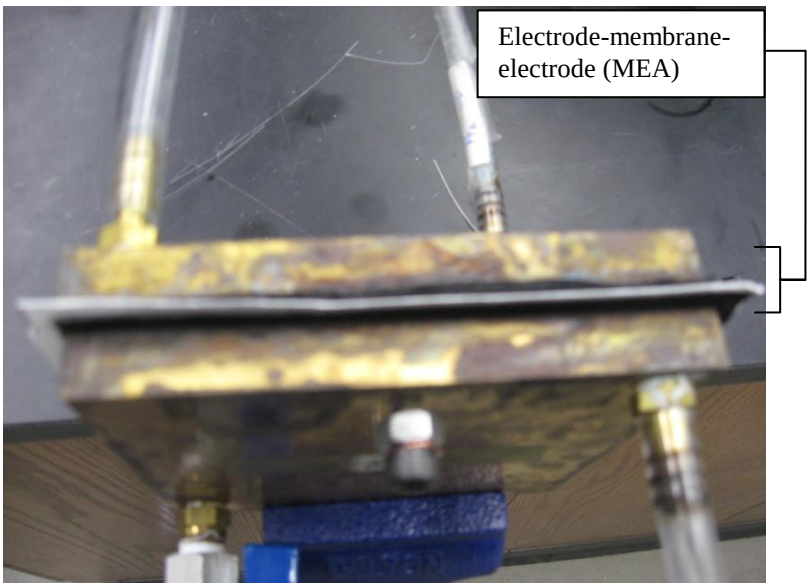

Figure 4.10. Bipolar plates and the MEA.

The AMFC internal structure was characterized through direct measurements of the length, width, and thickness of the internal parts. L_1 = 2 mm, L_2 = 0.273 mm, L_3 =0.146 mm, L_4 = 0.5 mm, L_5 = 0.146 mm, L_6 = 0.273 mm, L_7 = 2 mm. The dimensionless parameters were then calculated for the AMFC, obtaining $\xi_1/\xi_x = \xi_7/\xi_x = 0.374$, $\xi_2/\xi_x = \xi_6/\xi_x = 0.051$, $\xi_3/\xi_x = \xi_5/\xi_x = 0.027$, $\xi_4/\xi_x = 0.094$, $\xi_x = 0.125$, $\xi_y = \xi_z = 2.822$ and $\xi_t = 0.374$, $\xi_c = 0.187$, with $V_T = 7.69 \times 10^{-5}\ m^3$.

4.1.5 Fuel Cell Station

A test station was set up to run the experiments for the AMFC. The test station consists of a fume hood, hydrogen and oxygen tanks, gauges and pressure regulators. All the equipment is kept inside of a hood where any eventual leaking from the gas tanks or any line can be exhausted. The experiment set up is shown in Fig. 4.12, Fig. 4.13 and Fig. 4.14.

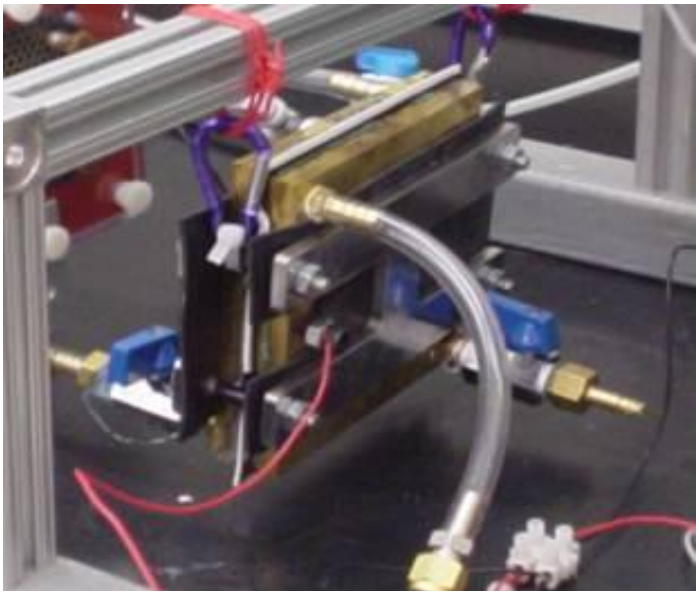

Figure 4.11: Photo of a finished alkaline membrane fuel cell using membrane made from cellulose.

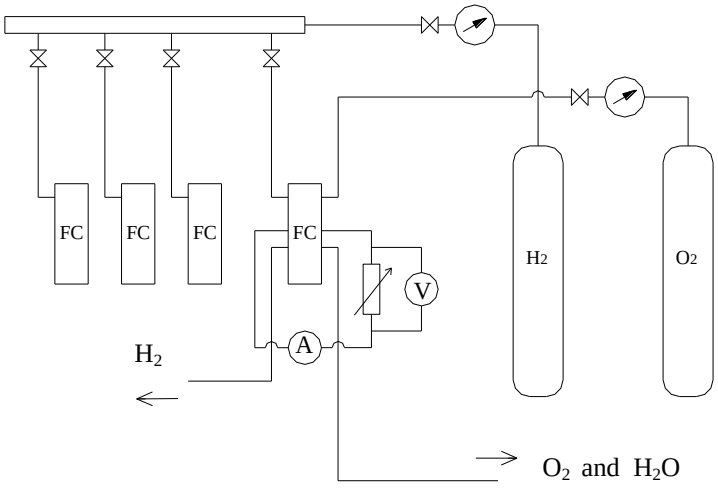

Figure 4.12: Schematic of the experimental set up for AMFC

Figure 4.13: Fuel cell test station.

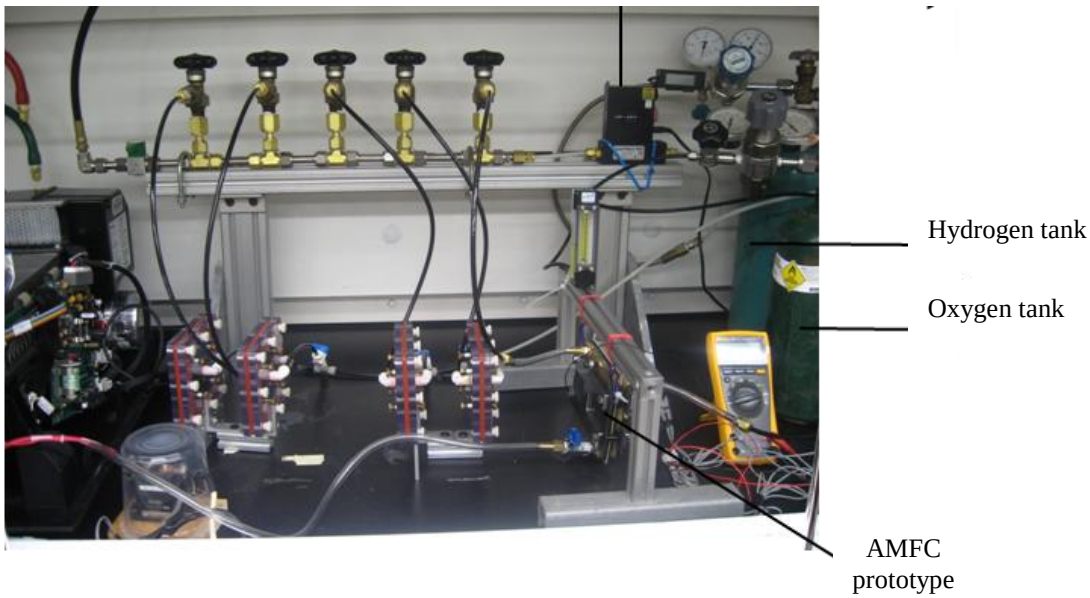

Figure 4.14: Alkaline fuel cell and all the components.

4.2 Numerical Results and Experimental Validation

The numerical simulation of the single AMFC is performed by solving the equations: Eqs. (2.49), (2.65), (2.67), (2.71), (2.80), (2.75), (2.68) and (2.52). The unknowns are θ_i and P_i , i.e., the temperatures in the seven control volumes, and the gas pressures in CV2 and CV6. The system is solved like the previous model, i.e. with a Fortran code, using a quasi-Newton method [83], where a tolerance for the norm of the residual vector less or equal to 10^{-6} .

The experimental results were obtained using hydrogen and pure oxygen as fuel and oxidant, respectively; both at the pressure of 1.5 psi . Due to possibility of the carbon monoxide present in the air to react with the hydroxyl (Eq.2.47), pure oxygen was used instead of air as oxidant. The gas flow was high enough to maintain a steady current output but not too high as to dry out the interior of the cell. A variable electrical resistance made of Ni-Cr wire was used as variable electrical load.

The experimental validation was based on direct measurements of the current and voltage produced by the fuel cell running with two different solution concentrations, 30wt% KOH and 45wt% KOH. In order to produce the cell polarization curve, the adjustable load resistance was reduced from open circuit $(I = 0)$ to short circuit (maximum current) where the maximum measured current was approximately 2.2 A for electrolyte concentration of 30% and 1.87 A for electrolyte concentration of 45wt%. Voltage and current measurements were performed for each of the ten cells with a digital multimeter ICEL-MD-6110.

Five runs were conducted for concentration of 30wt% and 45wt % KOH, the voltage and the current were measured from resistance equal zero to 8Ω. The Fig. 4.15 and 4.16 show the experimental results of voltage and current for the five runs for 30wt% KOH and the Fig. 4.17 and 4.18 show the experimental results of voltage and current for the five runs for 45wt% KOH. Where $\tilde{R} = \frac{R}{R_{ref}}$; $\tilde{R}$ is the dimensionless electrical resistance; R is the electrical resistance, Ω and $R_{ref} = 1\Omega$ is the reference electrical resistance.

The precision limit for each voltage and current point was computed as two times the standard deviation of the average value of the five runs obtained for each load, [70]. The Figs. 4.19-4.22 show the obtained experimental results for two electrolyte concentrations (30wt% and 45 wt% KHO).

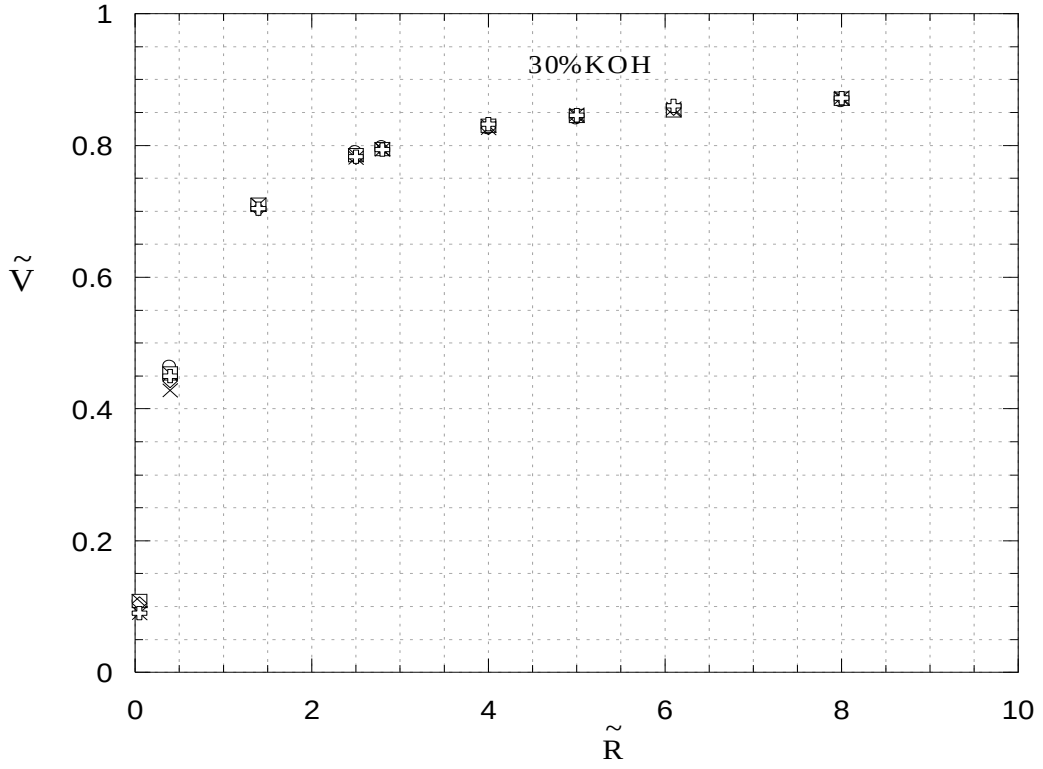

Figure 4.15: Experimental irreversible voltage measured for 30wt% KOH solution.

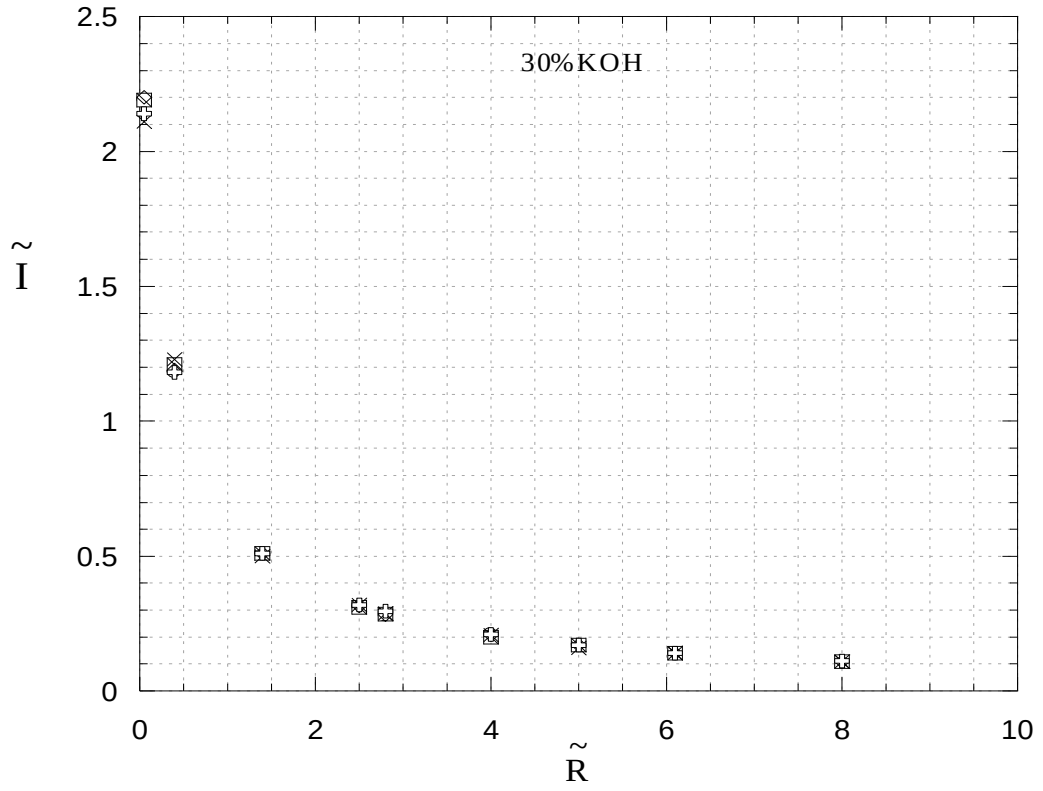

Figure 4.16: Experimental current measured for 30wt% KOH solution.

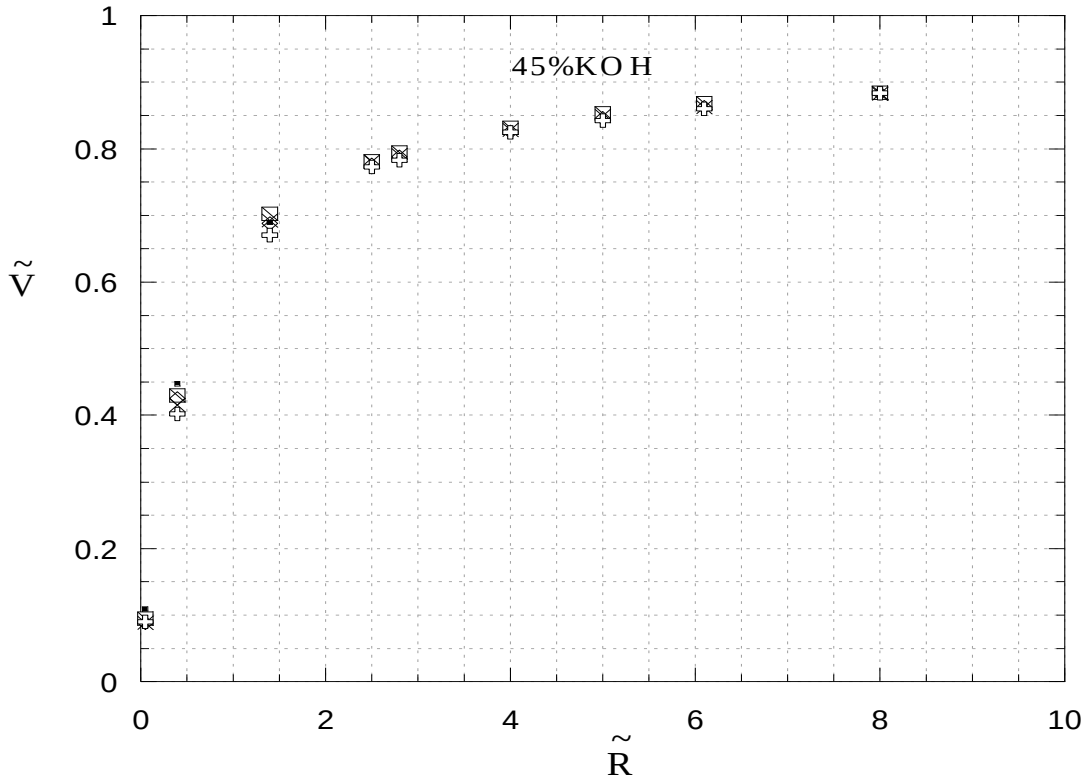

Figure 4.17: Experimental irreversible voltage measured for 45wt% KOH solution.

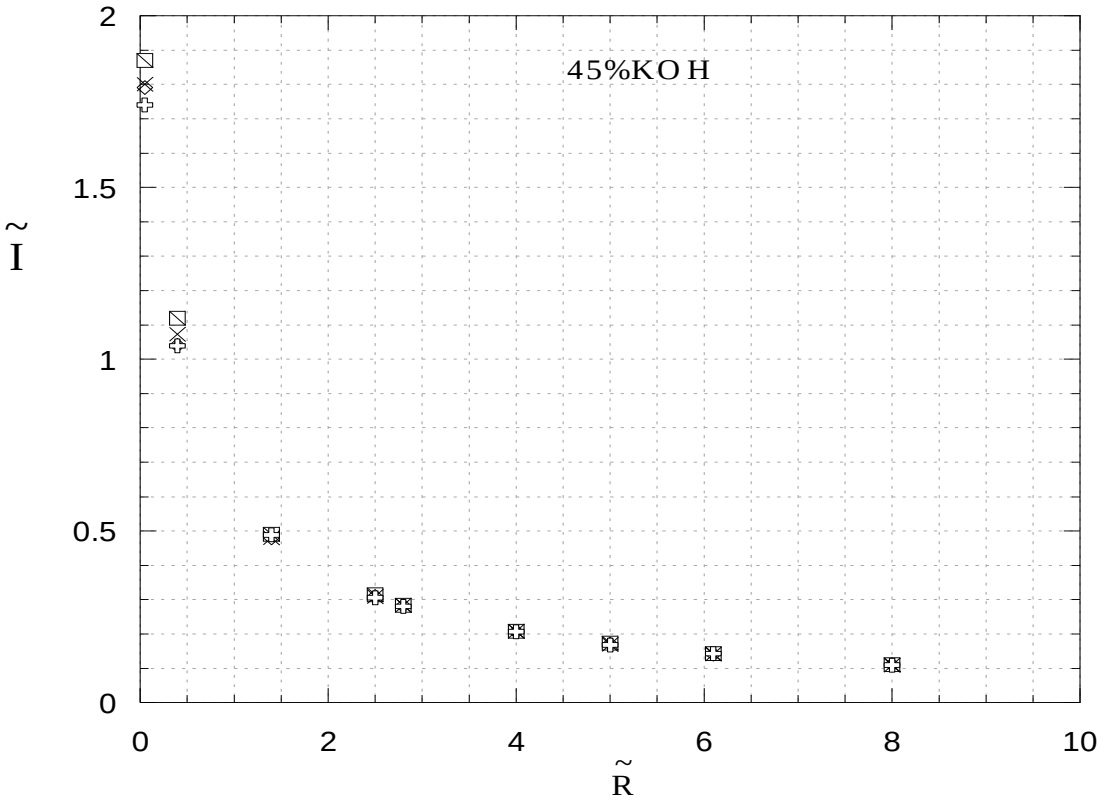

Figure 4.18: Experimental current measured for 45wt% KOH solution.

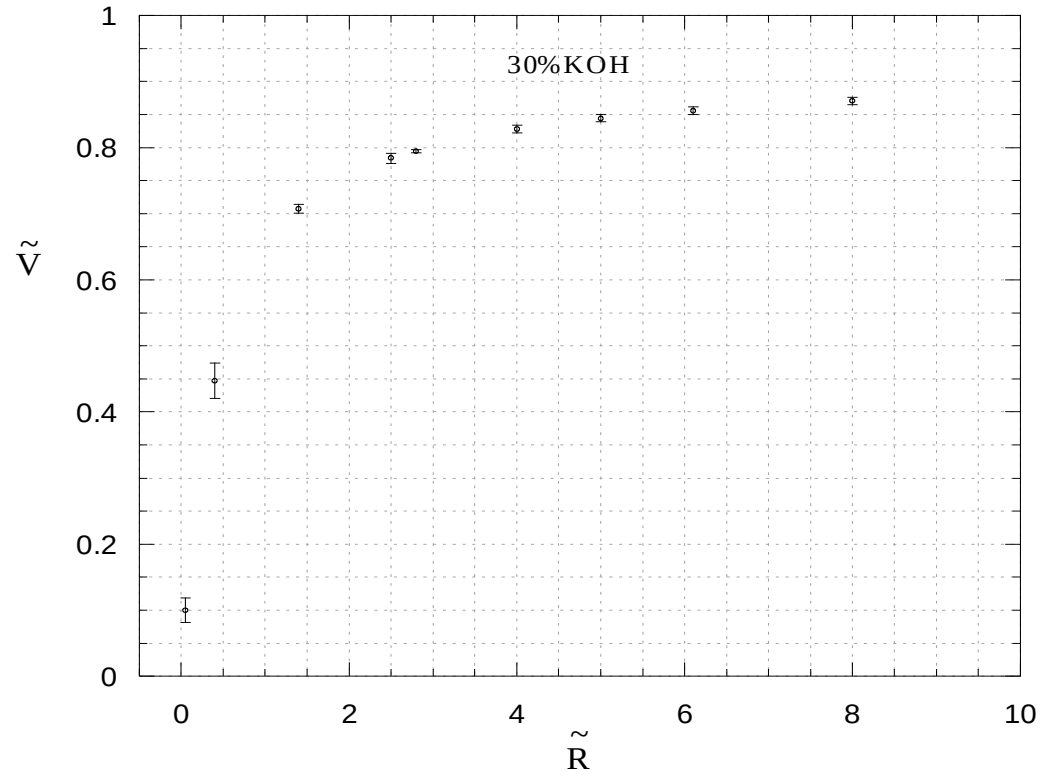

Figure 4.19: Precision limit for the experimental irreversible voltage for 30wt% KOH.

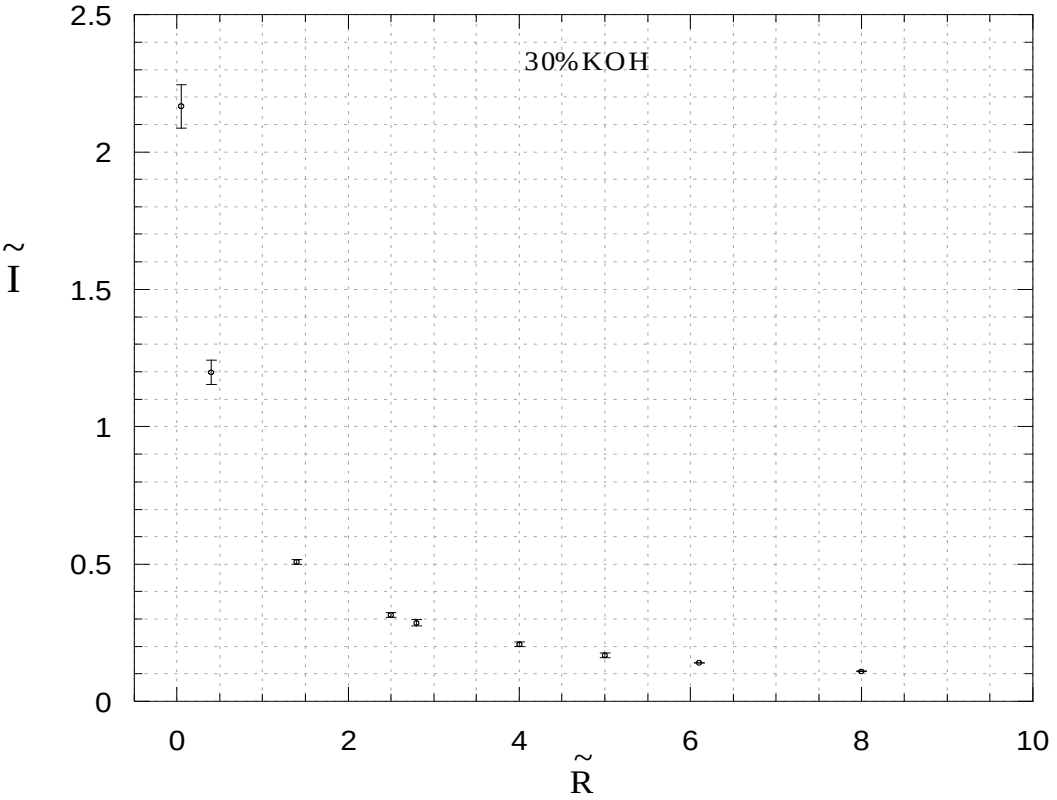

Figure 4.20: Precision limit for the experimental current for 30wt% KOH.

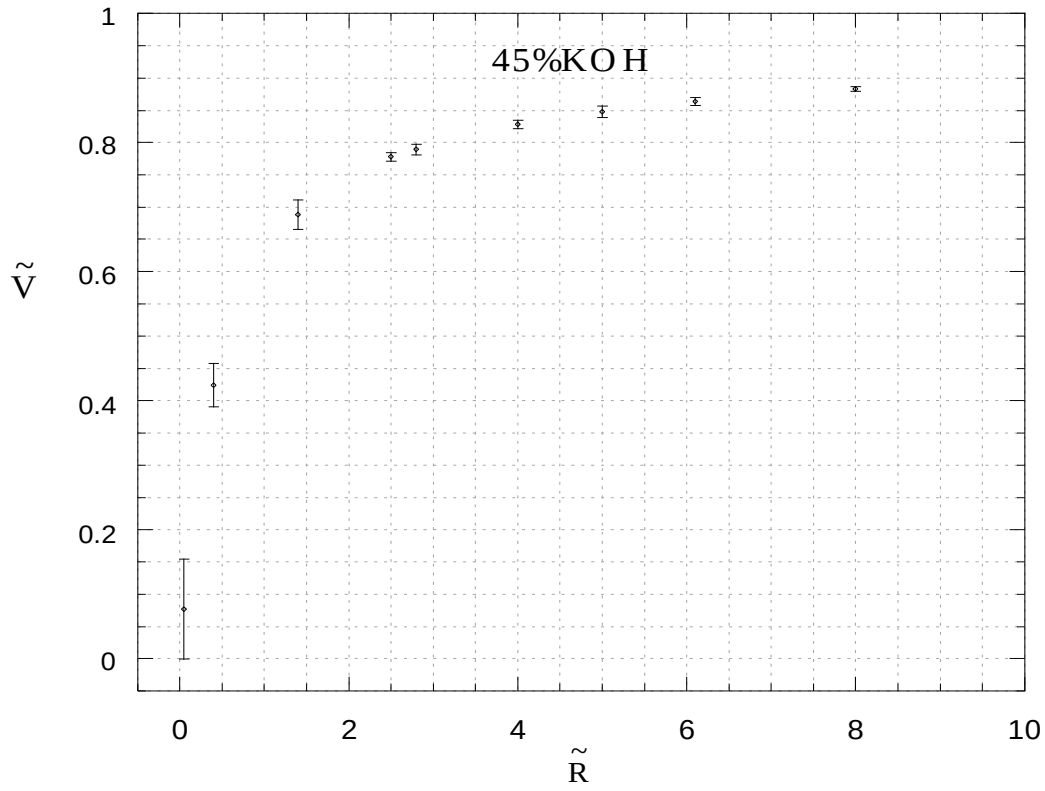

Figure 4.21: Precision limit for the experimental irreversible voltage for 45wt% KOH.

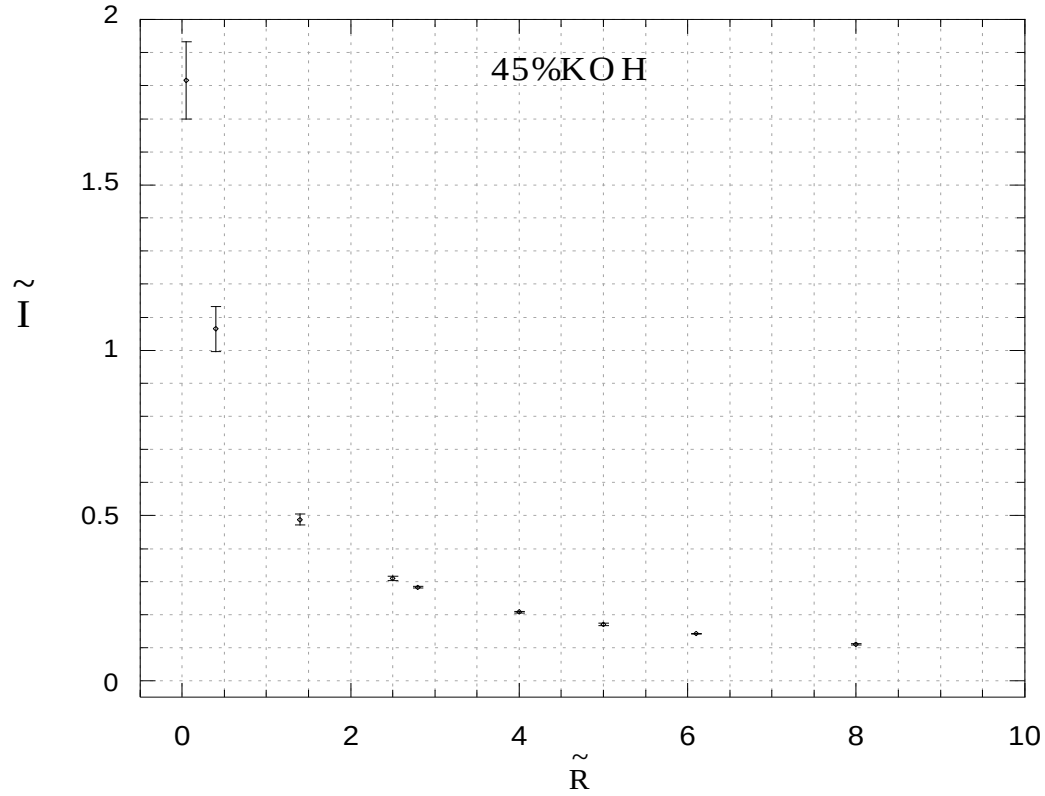

Figure 4.22: Precision limit for the experimental current for 45wt% KOH.

The electrical current is considered an independent variable in our model, meaning; it is an input value in the numerical code. The adjustment of parameters of the model was made such as the numerical voltage computed for the input electrical current would be in agreement with the voltage corresponding to the current measured experimentally, i.e, both, the numerical current and voltage would be in agreement with experimentally measured current and voltage. Such agreement can be seen in the Fig.4.24 and Fig.4.26. Comparing the Fig.4.15 – Fig. 4.22 we can see that the electrical current generated by the fuel cell decreases as the voltage and the load (electrical resistance) increases. The voltage and the current are inversely proportional quantities, meaning, high values of current correspond to low values of voltage, due voltage losses.

Once we have the experimental results, the next step for the experimental validation of the model is to compare them with the numerical solution of the governing equations. Some of the necessary data were either taken from technical literature [66,71-75,77,82,85] or measured. The remaining values were determined by the solution of an inverse problem of parameter estimation using as reference values the ones measured for the PEMFC model. The Table 4.2 and 4.3 bring the values of physical properties used in this study.

Table 4.2: Thermal conductivity, density and electrical conductivity of the electrolyte as function of concentration of the alkaline solution [77,85].

% wt	$k\,[W.m^{-1}K^{-1}]$	$\rho\,[kg.m^{-3}]$	$\sigma_{sol}\,[\Omega^{-1}m^{-1}]$
10	0.611	1091.876	36.90
30	0.59	1292.00	62.11
45	0.561	1475.35	48.74

The experiments were run using the same components under the same conditions just changing the concentration of the electrolyte; therefore the simulation model should be able to capture that change when just the parameters related to concentrations are altered.

For the case where the concentration of KOH is 30wt%, we assume $\tilde{V} = \tilde{V}_e$ when $\tilde{I} = 0.$ The cells electrical and net power were calculated by starting from $\tilde{I} = 0.1$, and proceeding with increments of ($\Delta\tilde{I} = 0.05$) until the limit current is reached.

The Figs. 4.23 – 4.26 bring the comparison between the numerical results for voltage and current and the experimentally results measured in laboratory for 30 and 45wt% KOH. Error bars were placed in the experimental points and the precision limit was computed as two times the standard deviation of the average value of the 5 runs obtained (Fig. 4.19-4.22).

According to the model, the actual open circuit voltage (when $\tilde{I} = 0$) is equal to the reversible cell potential, because it has been assumed that no losses result from species crossover from one electrode through the electrolyte, from internal currents or leakage.

Table 4.3: Physical properties used in the experimental validation of the single AMFC mathematical model.

$c_{p,f}$ = 14.95 kJ kg^{-1} K^{-1}	T_f, T_{ox}, T_∞ = 290.15 K = 17 ^{o}C
$c_{p,ox}$ = 0.91875 kJ kg^{-1} K^{-1}	U_{wi} = 50 W m^{-2} K^{-1}, i = 1 to 7
$c_{v,f}$ = 10.8 kJ kg^{-1} K^{-1}	V_{ref} = 1 V
$c_{v,ox}$ = 0.659375kJ kg^{-1} K^{-1}	$V_T = 7.69\times10^{-5}$ m^3
I_{ref} = 1 A	ϕ_4=0.442
($i_{0,a}$, $i_{0,c}$) = (0.11, 1.97) A m^{-2}	$c_{p,4}$=0.109 kJ kg^{-1}K^{-1}
k_f = 0.18 W m^{-1} K^{-1}	$\rho_4 = 461.8$ kg.m^{-3}
k_{ox} = 0.0266 W m^{-1} K^{-1}	$\sigma_2, \sigma_6 = 8570\,\Omega^{-1}$m^{-1}
k_p = 0.12 W m^{-1} K^{-1}	ϕ_2, ϕ_6 = 0.01
$\dot{m}_{ref} = 5.10^{-5}$ kg s^{-1}	ϕ_3, ϕ_5 = 0.003
p_f = p_{ox} = 0.01 MPa = 1.5 psi	α_a, α_c = 0.5
p_∞ = 0.1 MPa = 1 atm	$\mu_1 = 10^{-5}$ Pa.s
q = 2.45	$\mu_7 = 2.4\times10^{-5}$ Pa.s
R_f = 4.157 kJ kg^{-1} K^{-1}	$\sigma_1 = \sigma_7 = 2.91\,\Omega^{-1}$m^{-1}
R_{ox} = 0.2598 kJ kg^{-1} K^{-1}	$\sigma_3, \sigma_4, \sigma_5 = \sigma_{sol}$

The Fig. 4.23 and 4.25 show a good qualitative and quantitative agreement between the numerical and experimental results for low resistance ($\tilde{R} < 2.5$) for both concentrations studied and the Fig. 4.24 and 4.26 shows that the fuel cell generates low current at high resistance levels ($\tilde{R} > 2.5$).

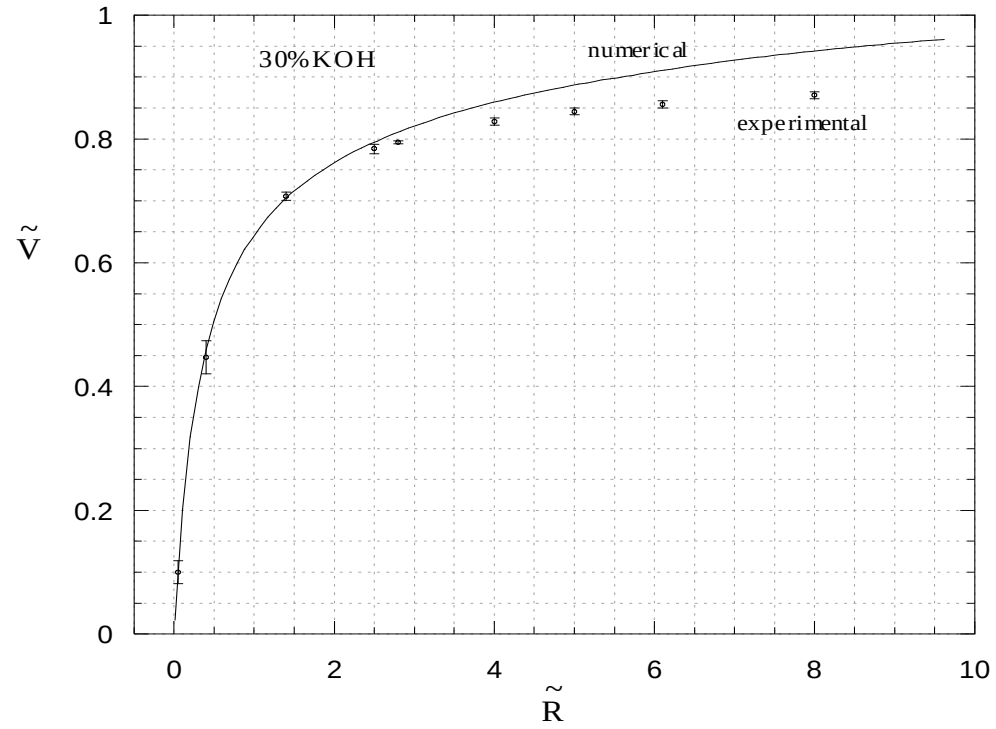

Figure 4.23: Comparison between the numerical and experimental results of voltage for 30wt % KOH.

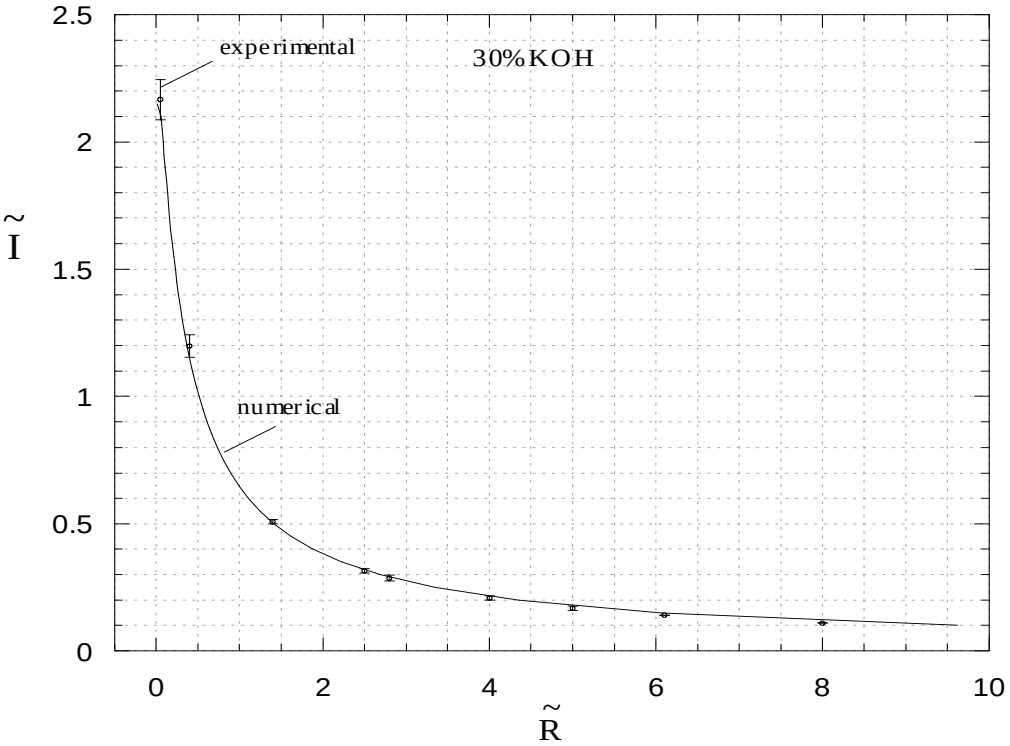

Figure 4.24: Comparison between the numerical and experimental results of current for 30wt %KOH.

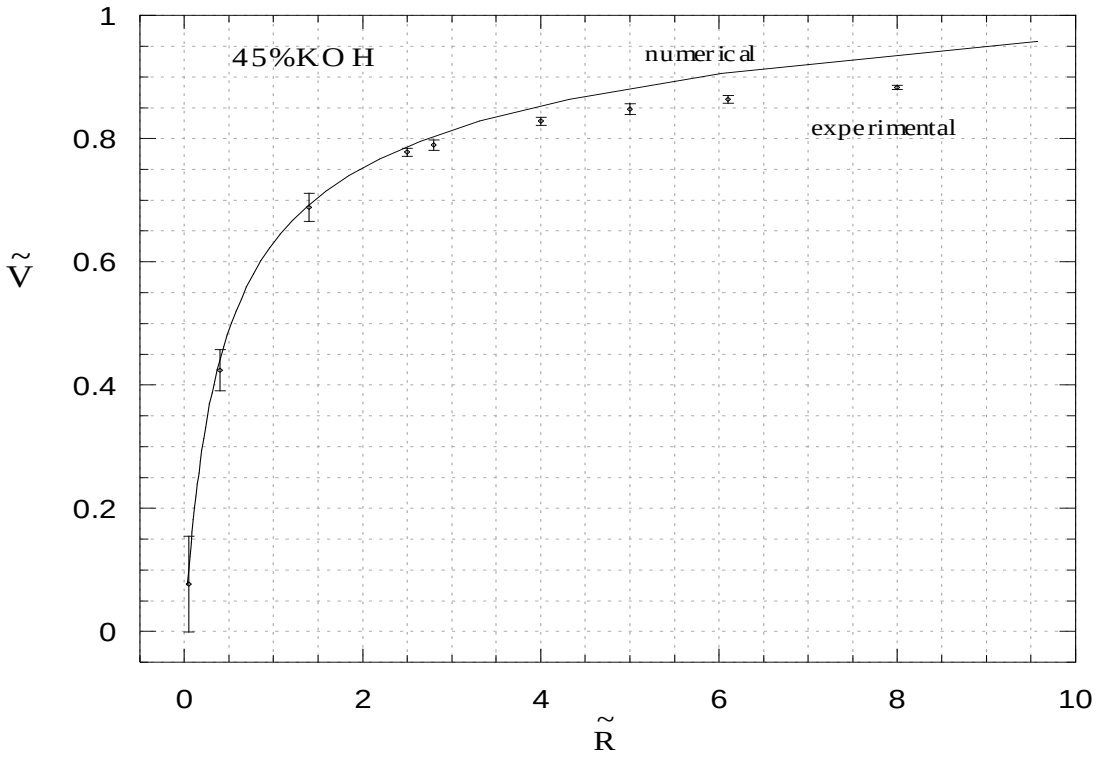

Figure 4.25: Comparison between the numerical and experimental results of voltage for 45wt % KOH.

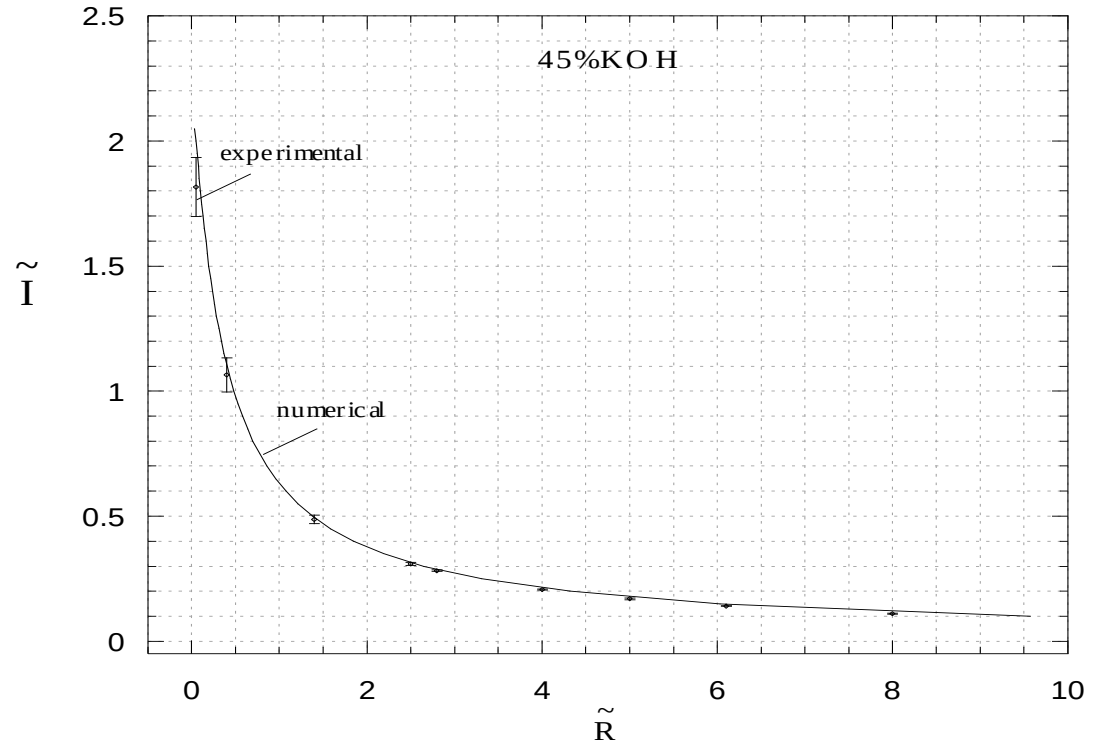

Figure 4.26: Comparison between the numerical and experimental results of current for 45wt %KOH.

The reason why we do not have a good quantitative agreement between the numerical and experimental results for high resistance levels ($0 \le \tilde{I} \le 0.3$) is that our model does not consider losses from species crossover through the electrolyte, internal currents and leakage. All these factors make the actual open circuit voltage (at $\tilde{I} = 0$) not to be equal to the reversible open circuit voltage (the Nernst thermodynamic equilibrium potential). This difference is expressed by the gap between the numerical and experimental results in the Fig. 4.23 and 4.25.

The Fig. 4.27 and 4.28 show the numerical results of current, voltage and power, which was computed multiplying the voltage by the current numerically obtained for 30wt% and 45wt%.

The point of greater interest is the maximum power point which occurs at higher current levels. Comparing the Fig. 4.27 and 4.28 to Fig. 4.23-4.26 we can conclude that the maximum power point lies in a region where there is a good qualitative and quantitative agreement between the numerical and experimental results for both concentrations. ($0 \le \tilde{R} \le 1.5$). We expect to present a model that gives accurate results at the current levels where the maximum power is achieved.

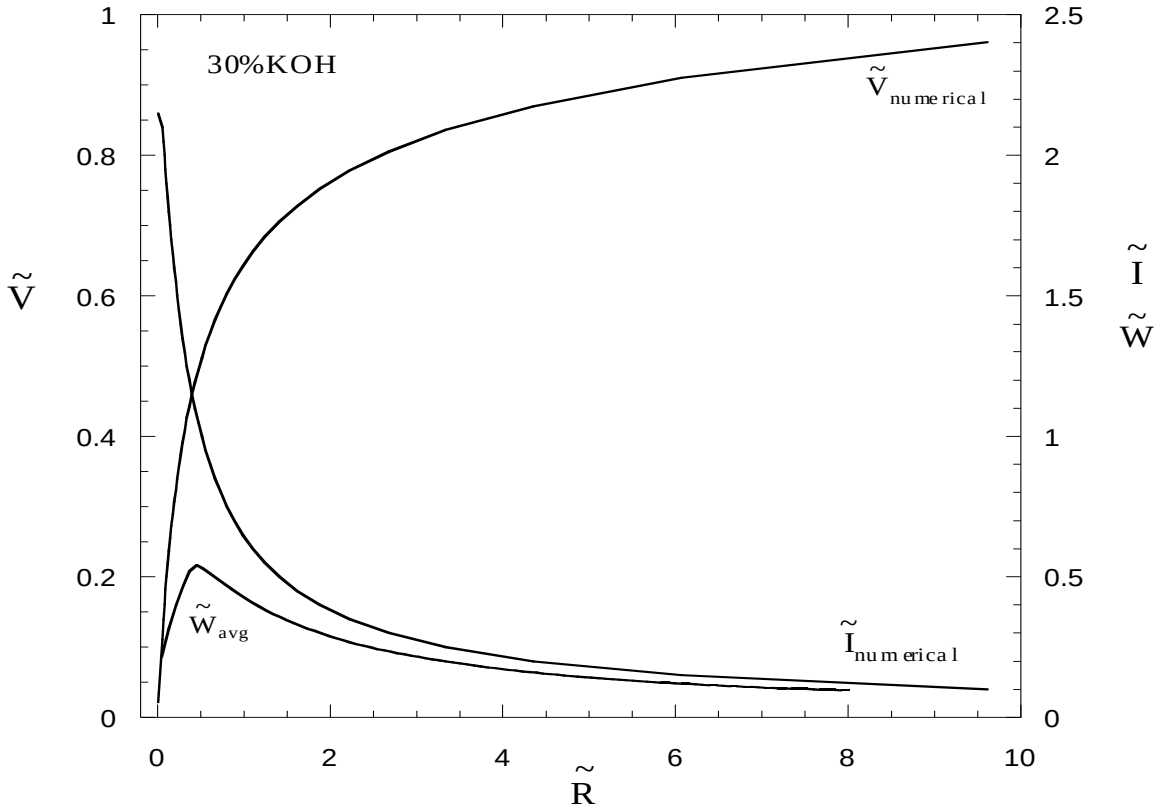

Figure 4.27: Numerical voltage and current curve and average power for 30wt% KOH.

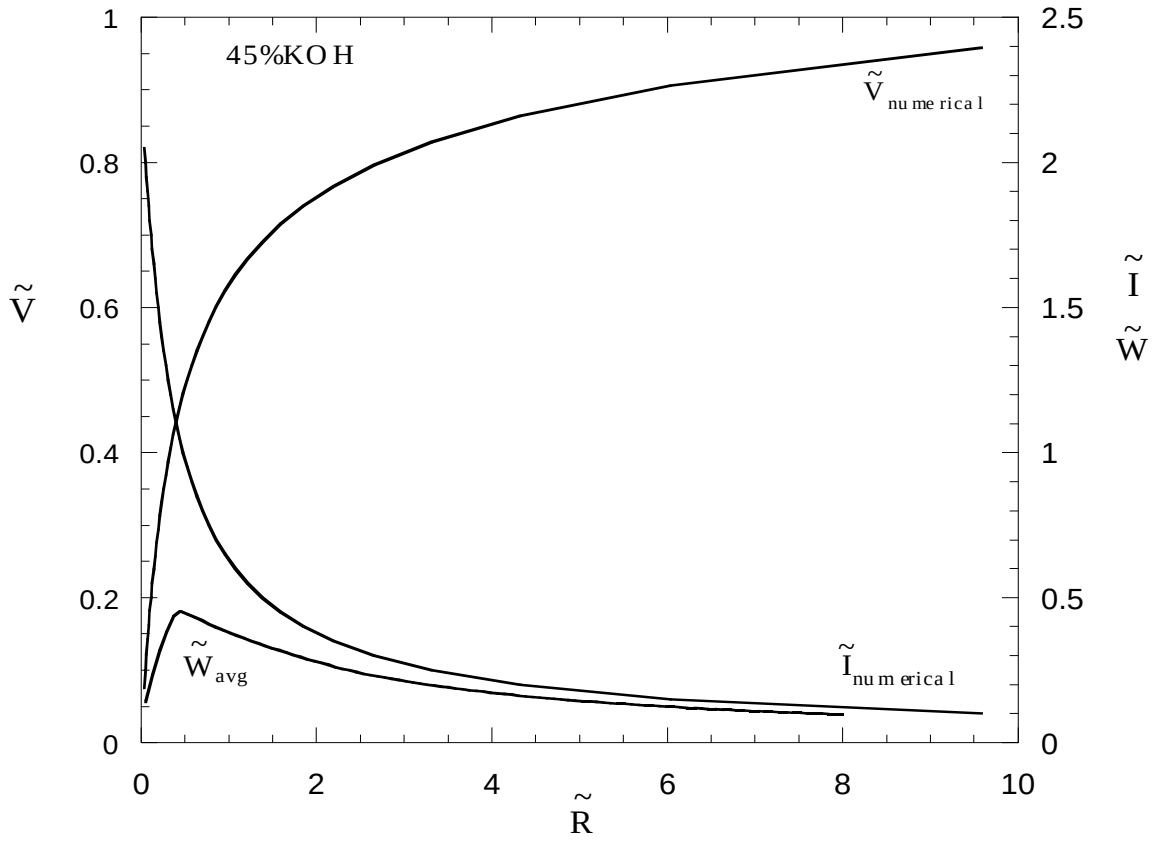

Figure 4.28: Numerical voltage and current curve and average power for 45wt% KOH.

The Fig. 4.29 and 4.30 show the numerical polarization and power curve for 30wt% and 45wt% respectively. Since the numerical and experimental results are in agreement, we used the numerical results to evaluate the polarization and the power curve, which means voltage and power versus current, respectively, from $\tilde{I} = 0$ when $\tilde{V} = \tilde{V}_e$ to a maximum current, when $\tilde{V} = 0$. Due the activation losses, we can see an accentuated potential drop at low current followed by a region where the ohmic losses are dominant and after $\tilde{I} = 2$ (for this prototype and electrolyte concentrations), the losses are mainly due concentration losses.

The total polarization is the sum of the electrical potential produced at the anode and cathode, $\tilde{V}_{i,a}$ and $\tilde{V}_{i,c}$. The sum of such potentials minus the potential losses the cell is the total fuel cell potential, $\tilde{V}_i$. The Fig. 4.31 and 4.32 shows the numerical electrical potential at the cathode and anode for the both concentration studied.

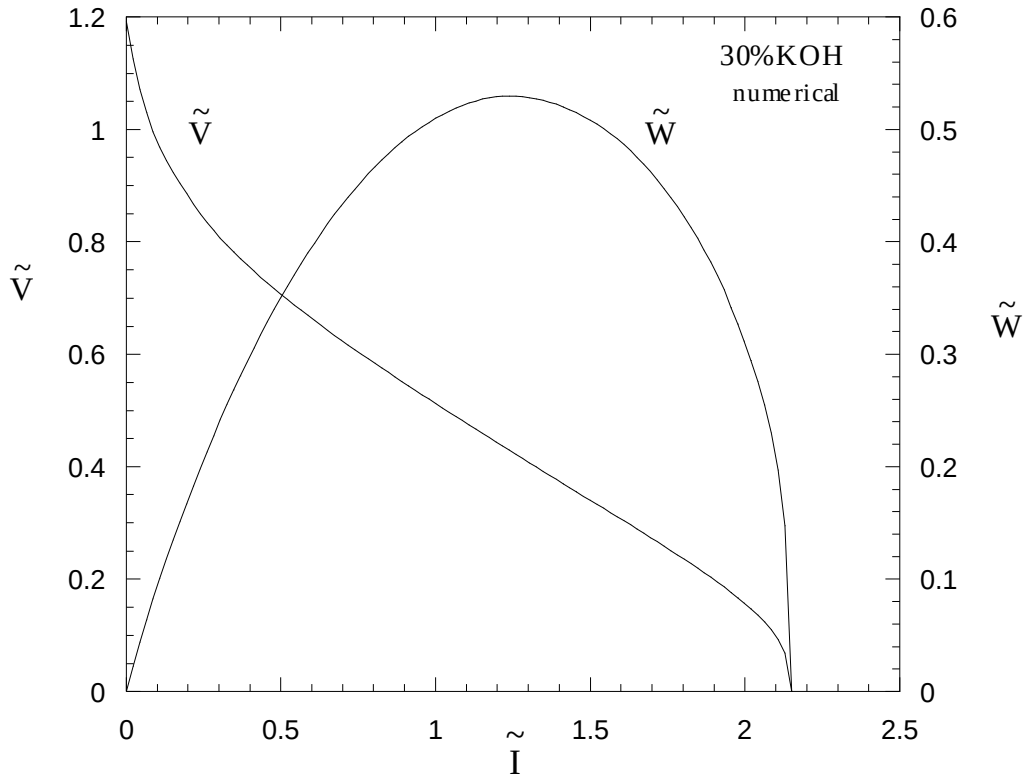

Figure 4.29: Total power and polarization curve numerically simulated for 30wt% KOH.

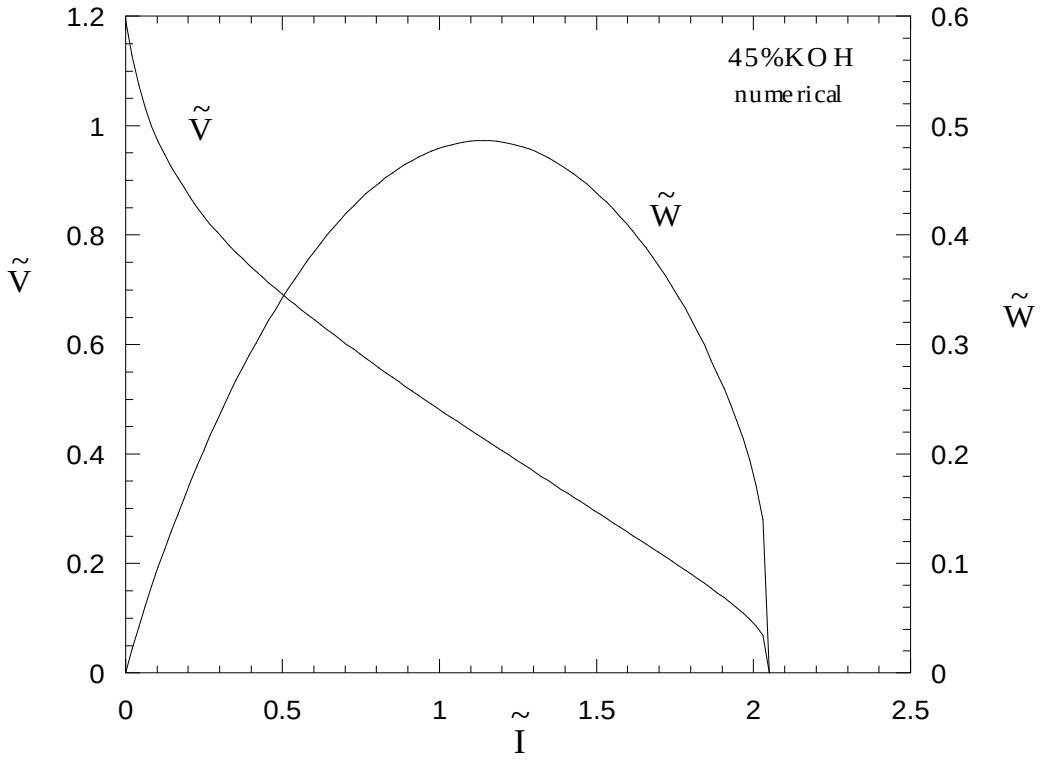

Figure 4.30: Total power and polarization curve numerically simulated for 45wt% KOH.

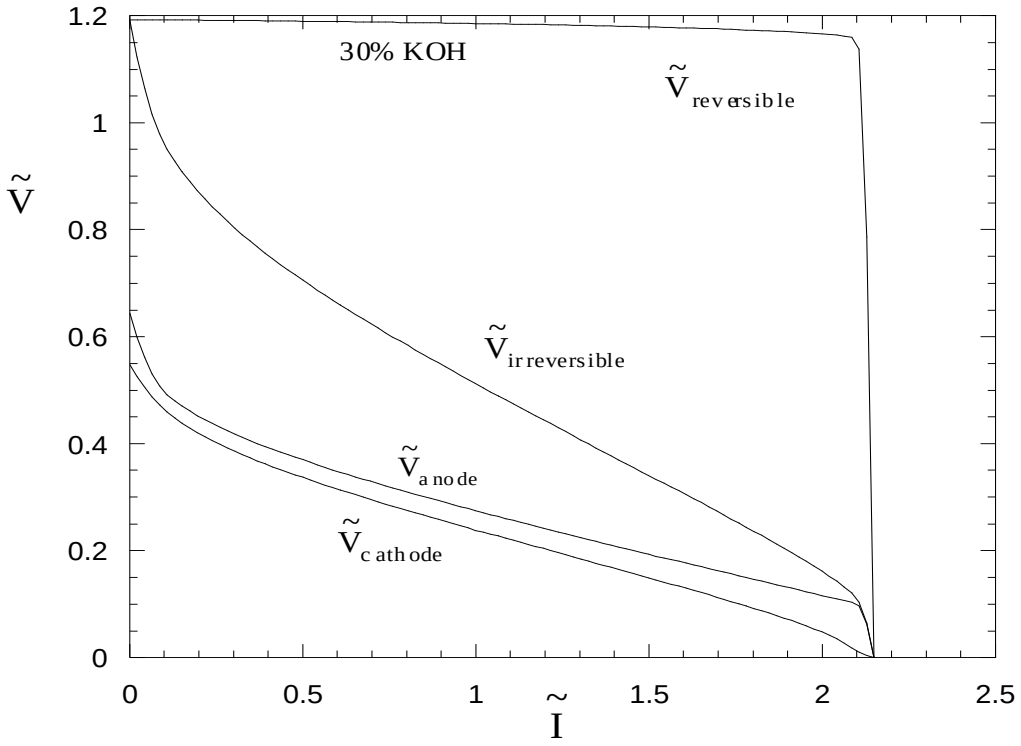

Figure 4.31: Total cell reversible, total cell irreversible, cathode and anode numerically simulated potentials for 30wt% KOH.

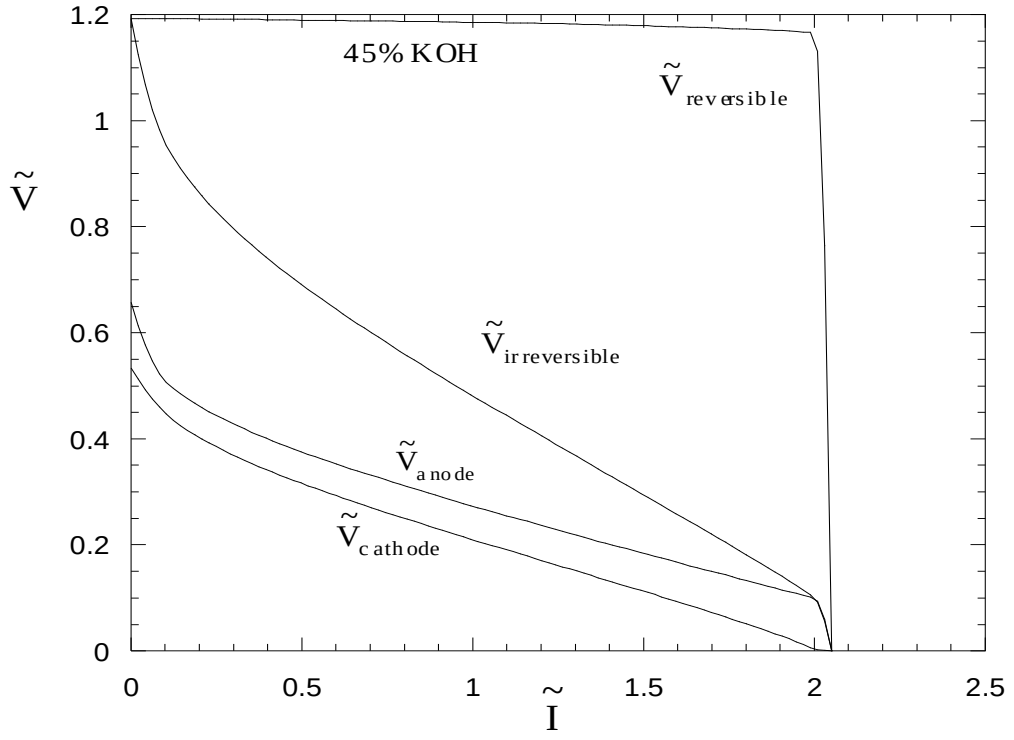

Figure 4.32: Total cell reversible, total cell irreversible, cathode and anode numerically simulated potentials for 45wt% KOH.

Since the temperature of the fuel cell increases as the current increases and the change in the Gibbs free energy of reaction decreases as the temperature increases, according to Eq. (2.85), the increase of temperature will cause the reversible electrical potential to decreases. As the current increases the partial pressure of hydrogen and oxygen at the catalyst layers decrease (Eq. 2.65) due the increase of reactant consumption, reaching the zero limit, where the voltage at the electrode also drops to zero. In this simulation, the partial pressure of the oxygen at the cathode drops to zero first, $\tilde{V}_{i,c} = 0$, i.e, the cathode controls the limiting fuel cell operating conditions.

The model is also able to evaluate efficiency of the fuel cell as function of the current being generated as is shown in the Fig. 4.33 and 4.34.

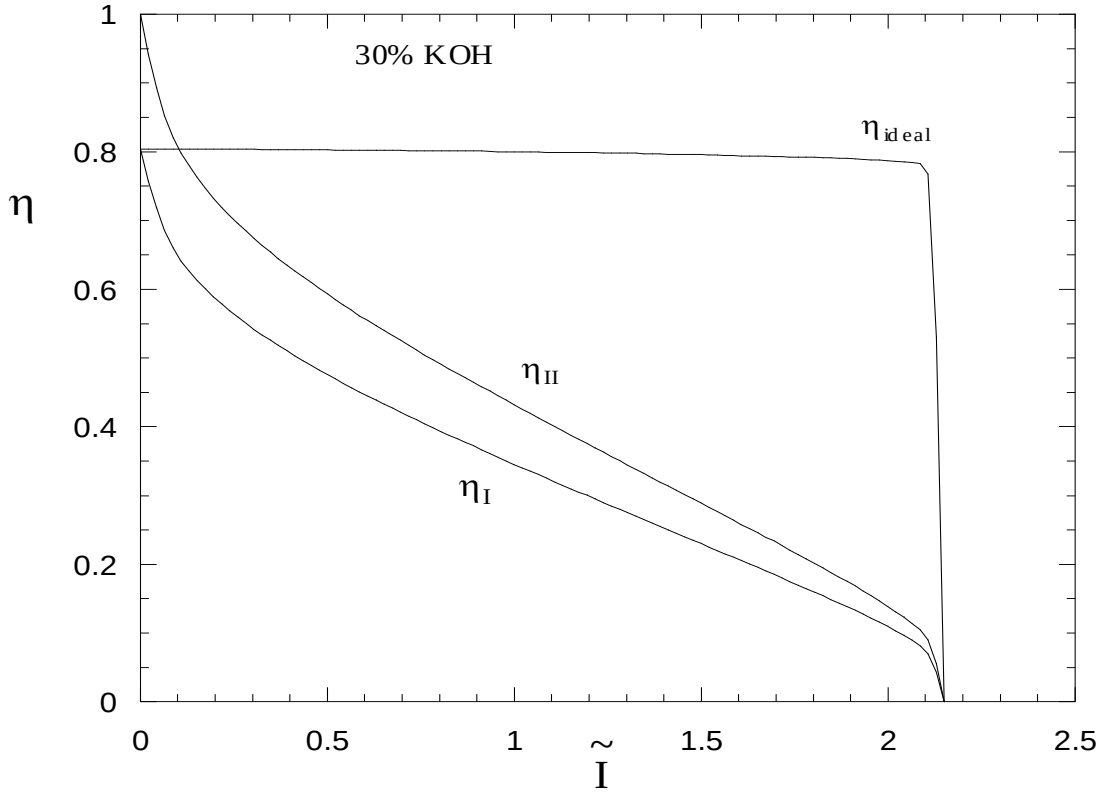

Figure 4.33: The ideal, first law, second law and net efficiencies for 30wt %KOH.

The Fig. 4.33 and 4.34 show a slight decrease in the ideal efficiency as the current increases. This is explained by the fact that the temperature also increases with the increase of the current. The first law efficiency is equal to the ideal efficiency for $\tilde{I} = 0$ and decreases as the current decreases. The second law efficiency is equal to 1 at $\tilde{I} = 0$, since at this current we

consider reversible operation (no losses). The simulation points out that the net efficiency is equal to the first law efficiency due the fact for this low range of current the work required to keep the reactant flow level are small (Eq. 2.89, 2.96).

The Fig. 4.35 and 4.36 show the comparison between power and polarization curve simulated numerically and efficiency between 30wt% and 45wt% KOH. We can see that the highest maximum power is reached at $\tilde{I} \approx 1.3$ for 30wt% KOH, which is the central point for performance evaluation. From this analysis we can demonstrate that the prototype using 30wt% KOH reaches higher maximum current and generates higher power at a higher current than 45wt% KOH and reaches higher efficiency as well (Fig. 4.36).

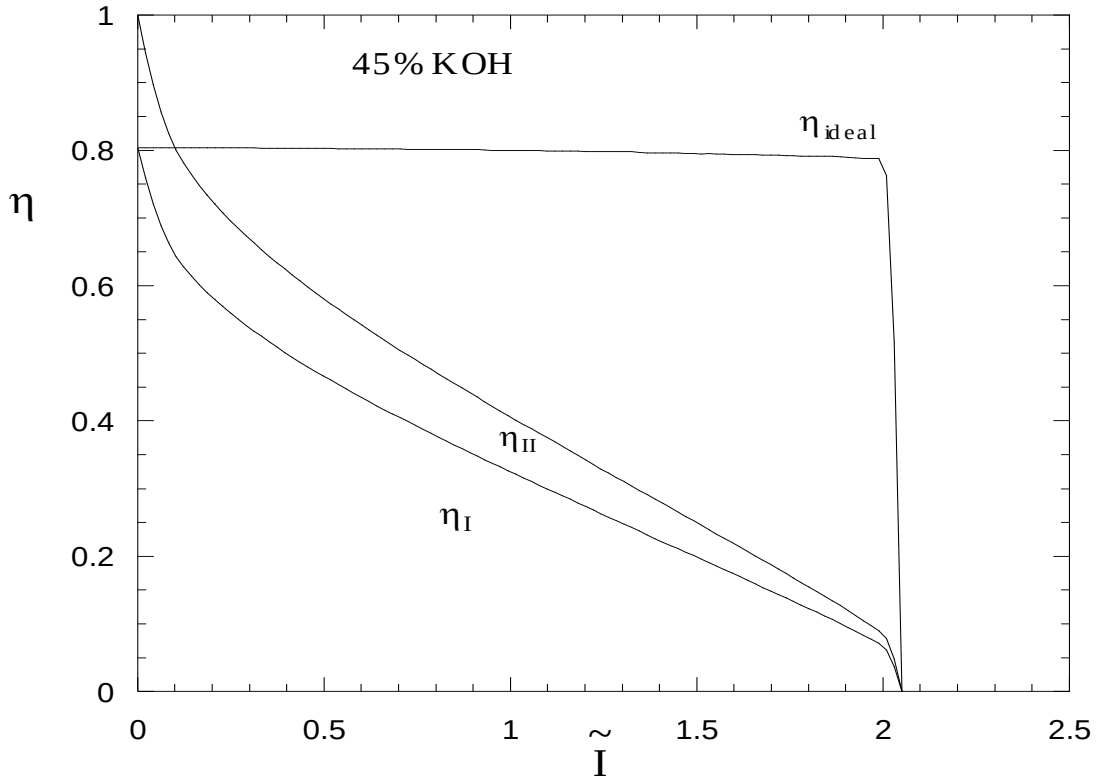

Figure 4.34: The ideal, first law, second law and net efficiencies for 45wt% KOH.

In other words, the fuel cell running with concentration of 35wt% KOH generates higher output power and efficiency for the entire range of operating current than running with concentration of 45wt% KOH.

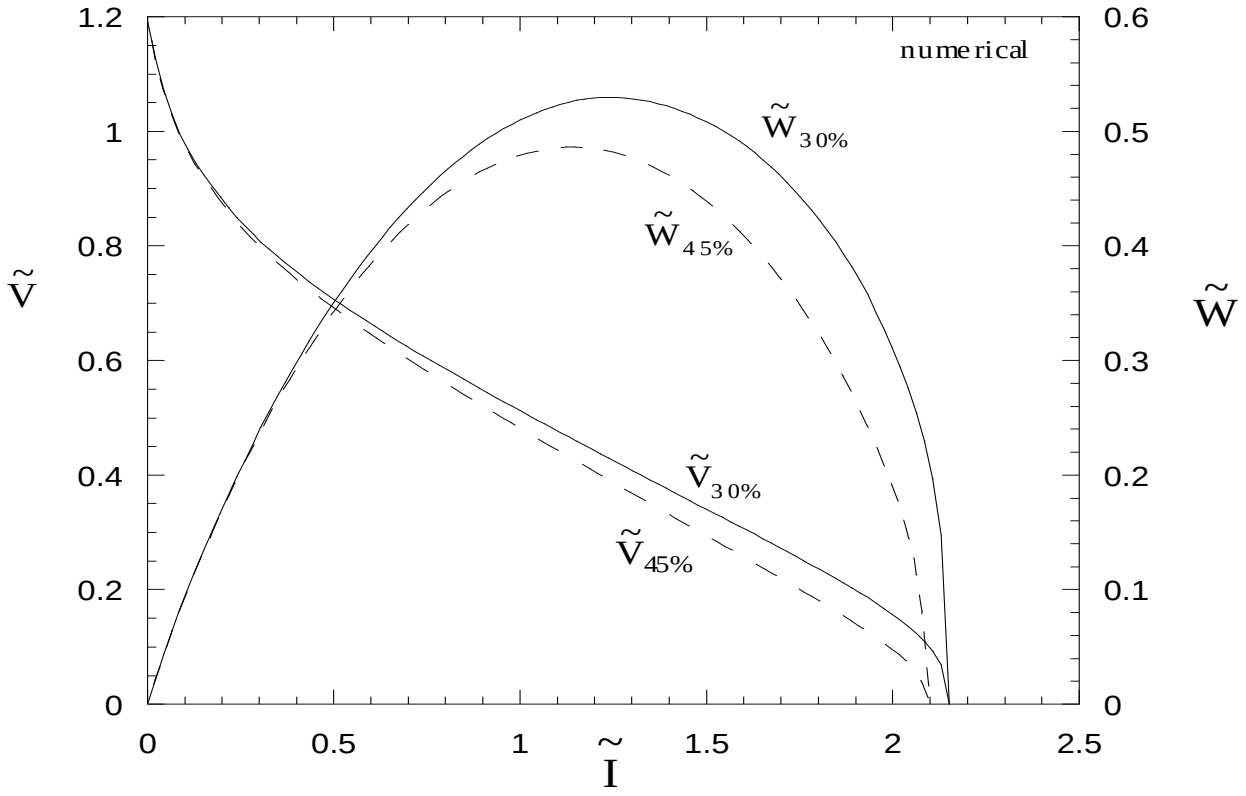

Figure 4.35: Comparison between total power for 30wt% and 45wt% KOH.

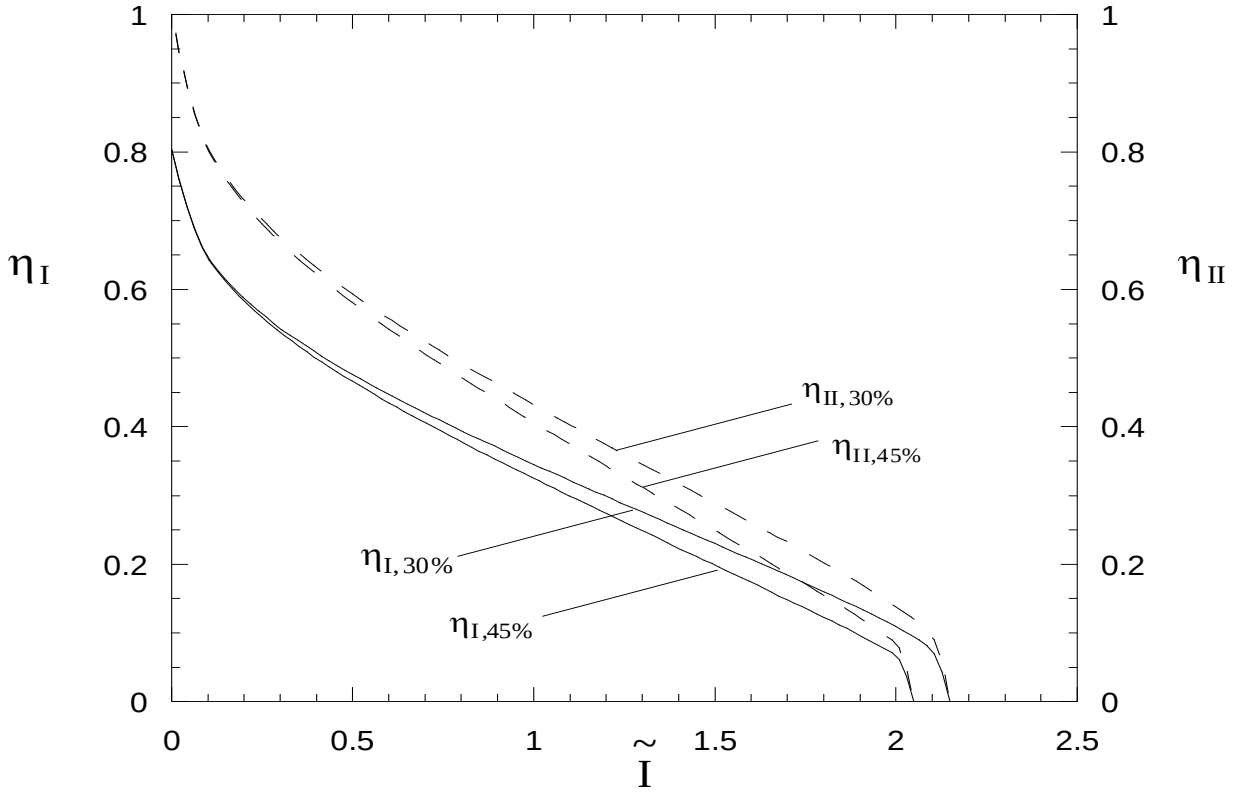

Figure 4.36: Comparison between first and second law efficiency for 30wt% and 45wt% KOH.

The measurement of temperature was made with the AMFC prototype at open circuit with electrolyte concentration of 10wt%KOH. High precision thermistors YSI 44004RC were used to measure the temperature of the electrodes and two Pipe-plug thermistor probes (TH-44004 Series, manufactured by Omega®) connected to the hydrogen and oxygen lines were used to measure the temperature of the reactant gas. The calibration was done in our laboratory using a thermal bath with crushed ice, where the resistance of the thermistors was measured every 21 seconds during 43 minutes using the software Labview data acquisition application 7 Express, from National Instruments [86].

The average and the standard deviation of the measured resistance were calculated and used to compute the coefficient γ of the thermistor according to the Eq. 4.1.

$$\gamma = \frac{\ln\left(\overline{\beta} / \beta_0\right)}{\frac{1}{T} - \frac{1}{T_0}} \tag{4.1}$$

where $\overline{\beta}$ is the average electrical resistance of the thermistor during the thermal bath with crushed ice, Ω; β_0 is the electrical resistance of the thermistor at T=25^{o}C (298.15 K) equals to 2252 Ω (value of resistance given by the manufacturer); T_0 = 0^{o}C is the temperature of the thermal bath.

The coefficient γ (Table 4.4) was calculated for each thermistor using the average of the resistance measured during the ice bath and then used to compute the temperatures related to the measured resistances according to the Eq. 4.2.

$$T = \frac{1}{\frac{1}{T_0} + \frac{1}{\gamma}\ln\left(\frac{R}{R_0}\right)} \tag{4.2}$$

The average and the standard deviation of the computed temperature were calculated and the bias limit, B_i, was determined. The bias limit was calculates as $B_i = 2\varepsilon$ [70].

The Table 4.5 shows the values of the average, standard deviation and bias limit for the resistance and temperature of the thermistors.

The B_i for resistance and temperature for the thermistors TH-44004 was much higher than the thermistors YSI-44004 however it was considered a good precision since it is not expected changes in temperature of the reactants in the gas lines.

A hole was made in the bipolar plate so the thermistor would be able to pass through the metal and electrode and to touch the membrane (Fig.4.37). We intended to measure the temperature at the interface between the membrane and electrode (membrane/cathode and membrane/anode) verifying that the temperatures are not equal and they are both higher than the temperature of the inlet gas flow, what would demonstrate that the fuel cell has a temperature gradient in the flow direction. It is also our goal to show that the present model is capable of capturing the temperature gradient measured experimentally.

Table 4.4: Average, standard deviation and bias limit for the resistance a thermistors.

	Thermistor resistance, (Ω)			
	YSI 44004RC		TH-44004	
	Cathode	Anode	H_2	O_2
Average	7388.915257	7389.134537	7267.232469	7288.887211
Standard deviation (ε)	0.179716	0.204970	8.026705	46.006100
Bias (B_i)	0.359432	0.409940	16.053412	92.012201
γ (K)	3870.541711	3870.638385	3816.448184	3826.140637

Table 4.5: Average, standard deviation and bias limit for temperature of the thermistors.

	Thermistor temperature (K)			
	YSI 44004RC		TH-44004	
	Cathode	Anode	H_2	O_2
Average	273.150000	273.149303	273.150013	273.150444
Standard deviation (ε)	0.000469	0.000535	0.021582	0.122989
Bias (B_i)	0.000938	0.001069	0.0431614	0.245978

The materials used for the measurement of temperature of the AMFC were all the same used in the previous experiments run to generate polarization the polarization curves for 30 and

45wt% KOH except the electrode. The electrode used for this experiment was the Gas Diffusion Electrode (SGL 25BC) with 0.5 mg Pt/cm^2, 120 mm x 120 mm, manufactured by IRD-Fuel Cell Technology. The Fig. 4.38 is a schematic of the cross section of the IRD electrode given by the manufacturer. The reactive side of the electrode is more darker than the diffusive side as can be seen in the Fig. 4.39.

The AMFC internal structure was characterized through direct measurements of the length, width, and thickness of the internal parts. $L_1 = L_7 = 2$ mm, $L_2 = L_6 = 0.235$ mm, $L_3 = L_5 = 0.015$ mm, $L_4 = 0.5$ mm.

The dimensionless parameters for this configuration were then calculated: $\xi_1/\xi_x = \xi_7/\xi_x = 0.4$, $\xi_2/\xi_x = \xi_6/\xi_x = 0.047$, $\xi_3/\xi_x = \xi_5/\xi_x = 0.003$, $\xi_4/\xi_x = 0.1$, $\xi_x = 0.1202$, $\xi_y = 2.8845$ and $\xi_z = 2.8845$, $\xi_t = 0.4$, $\xi_c = 0.2$, with $V_T = 7.2\times10^{-5}$ m^3.

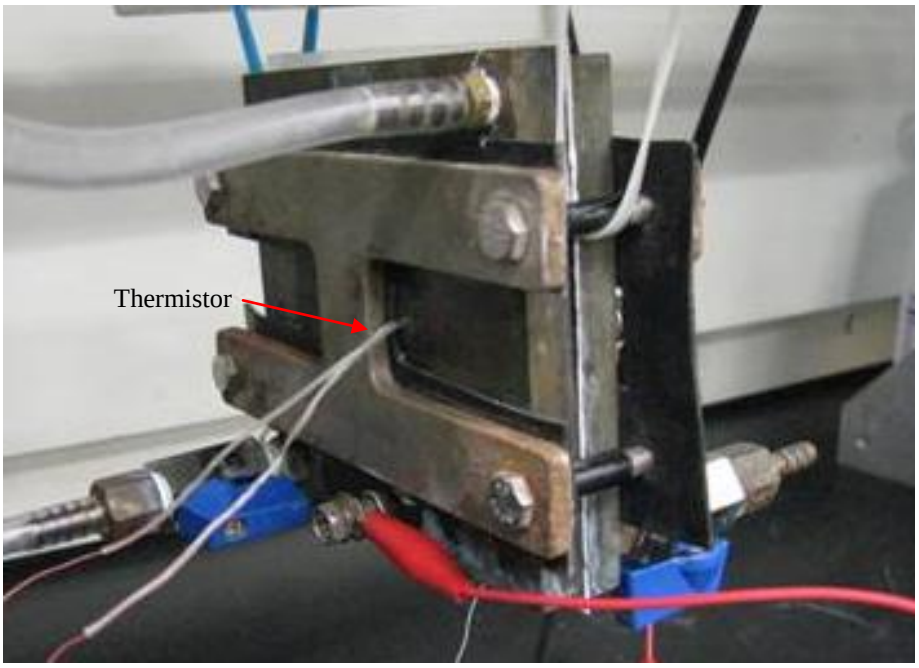

Figure 4.37: AMFC prototype with the thermistor passing through the bipolar plate.

Figure 4.38: Cross section of the IRD electrode.

To be sure that the reactant gases were at constant temperature when entering the fuel cell, we made the gases to pass through a serpentine inside of a container full of water. For safety reasons, we needed to run all the experiment in the fume hood, the container with water was left there for 36h before the experiment, so it could reach thermal equilibrium with the ambient; the Fig. 4.40 shows the apparatus.

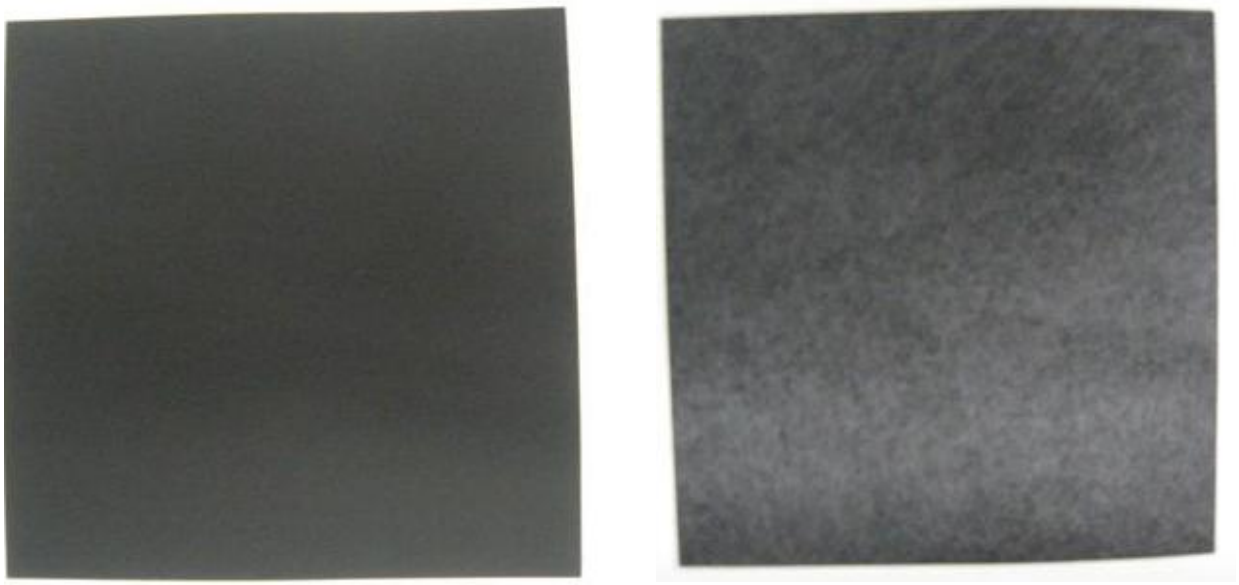

(a) (b)

Figure 4.39: (a) Reactive side of the electrode; (b) Diffusive side of the electrode

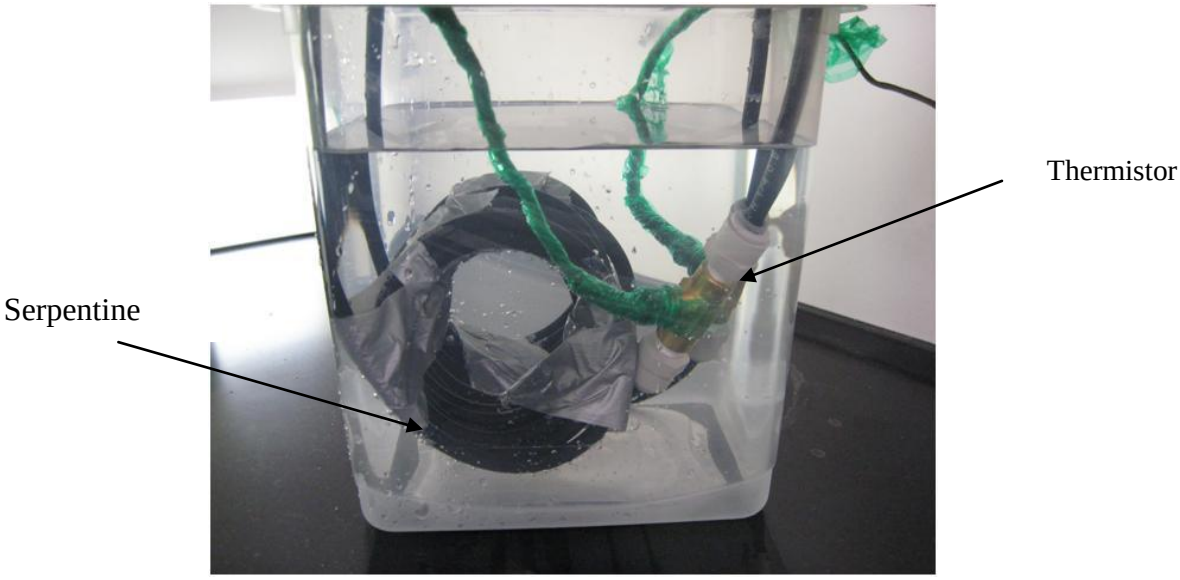

Figure 4.40: Picture of the container with the gas line and the thermistor TH-44004.

The Fig. 4.41 shows the temperature of the cathode, anode, reactants and the voltage of the fuel monitored for 210 s.

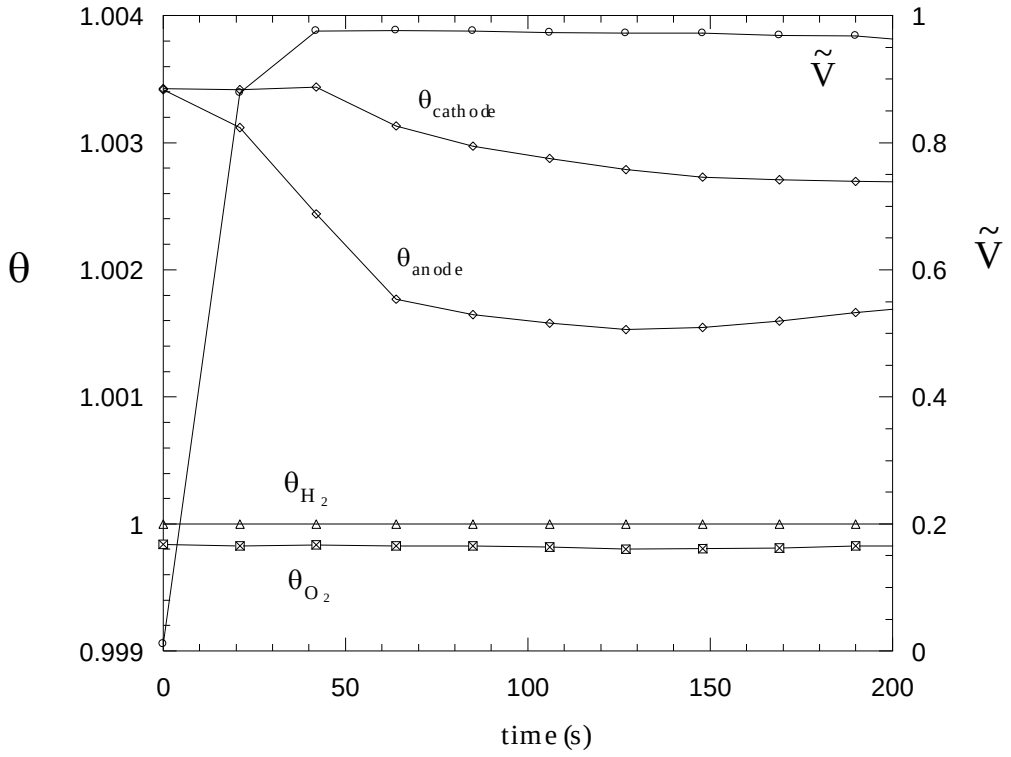

Figure 4.41: Voltage, reactant gases and internal temperature of fuel cell measured for the fuel running with electrolyte concentration of 10wt%KOH.

Since we did not use the same electrode used to validate the voltage and power output, a new set of input data with the appropriated physical properties of the new electrode is necessary to obtain numerical results. Most of the properties are the same used before, since we are still using the same membrane and reactant gases, the remaining values were determined by the solution of an inverse problem of parameters estimation; in this case such set is given by Table 4.6.

The AMFC was assembled following the same procedure described previously for the experimental validation of voltage and power output, with the darker face of the electrode (reactive layer) facing the membrane.

Table 4.6: Physical properties used in the experimental validation of the temperature for the single AMFC mathematical model.

$c_{p,f}$ = 14.95 kJ kg^{-1} K^{-1}	R_{ox} = 0.2598 kJ kg^{-1} K^{-1}
$c_{p,ox}$ = 0.91875 kJ kg^{-1} K^{-1}	V_{ref} = 1 V
$c_{v,f}$ = 10.8 kJ kg^{-1} K^{-1}	$V_T = 7.2 \times 10^{-5}$ m^3
$c_{v,ox}$ = 0.659375kJ kg^{-1} K^{-1}	$c_{p,4}$=0.109 kJ kg^{-1}K^{-1}
I_{ref} = 1 A	$\rho_4 = 461.8\,kg.m^{-3}$
($i_{0,a}$, $i_{0,c}$) = (0.0085, 0.0075) A m^{-2}	ϕ_4=0.442
k_f = 0.18 W m^{-1} K^{-1}	ϕ_2, ϕ_6 = 0.8
k_{ox} = 0.0266 W m^{-1} K^{-1}	ϕ_3, ϕ_5 = 0.53
k_p = 0.12 W m^{-1} K^{-1}	α_a, α_c = 0.5
$\dot{m}_{ref} = 5.10^{-5}$ kg s^{-1}	$\mu_1 = 10^{-5}$ Pa.s
$p_f = p_{ox}$ = 0.01 MPa = 1.5 psi	$\mu_7 = 2.4 \times 10^{-5}$ Pa.s
p_∞ = 0.1 MPa = 1 atm	$\sigma_1 = \sigma_7 = 1.6 \times 10^7\,\Omega^{-1}m^{-1}$
q = 2.18	$\sigma_2 = \sigma_3 = \sigma_4 = \sigma_5 = \sigma_6 = 36.90\,\Omega^{-1}m^{-1}$
R_f = 4.157 kJ kg^{-1} K^{-1}	

Since the simulation model presents a steady state analysis, the numerical voltage and the dimensionless cathode and anode temperature for this condition were plotted and compared

to the average of the experimental values measured after the steady state was reached (see Fig. 4.40).

The Table 4.7 shows the average, standard deviation (σ) and limit error (3σ) of experimental measurements of temperature and voltage after the steady state was reached. The experimental measurements were taken while the fuel cell was running at open circuit ($\tilde{I} = 0$) and even under that condition the thermistors were capable of reading a small temperature difference between the electrodes, due to the electrochemical reactions that are taking place to generate the open circuit voltage.

To simulate the open circuit condition we run the computational code considering a very small current ($I \leq 0.1\,A$) and performed the solution of an inverse problem of parameters estimation to determine the values of physical properties that were not measured (exchange current density, tortuosity and porosity).

Table 4.7: Numerical results and error analysis for voltage and dimensionless cathode and anode temperature for 10wt% KOH.

	$\tilde{V}$	$\theta_{cathode}$	θ_{anode}
Average	0.971111	1.002789	1.001619
σ	0.005856	0.000254	0.000281
3σ	$\pm$ 0.017570	$\pm$ 0.000076	$\pm$ 0.000840
Upper Limit	0.988978	1.003551	1.002460
Lower Limit	0.953543	1.002026	1.000779
Numerical Result	**0.974847**	**1.002417**	**1.002365**

Comparing the experimental measurements with the numerical results, we can see that the numerical results are within the error limits, showing a good quantitative agreement.

CHAPTER FIVE

CONCLUSIONS AND SUGGESTIONS

In this study, a mathematical model and simulation for PEMFC with temperature dependence on space and current was proposed and experimentally validated by direct comparison with output voltage and power measurements performed in PEMFC's in the laboratory. A set of 10 single commercial PEMFC's were used to obtain experimentally the voltage and power output; the simulation model was able to generate voltage and power output results that demonstrate good qualitative and quantitative agreement with the measured experimental data.

The validated mathematical model for PEMFC was modified to generate a mathematical model for AMFC respecting the conceptual differences between both fuel cells. Experimental validation was also conducted for the last model, at this time using an AMFC prototype built in laboratory. The goal was to obtain a reliable model able to capture the influence of the concentration of the electrolyte in the fuel cell voltage and power output. The comparison between the experimental and numerical results demonstrated that the model was able to represent the experimental trends with good qualitative and quantitative agreement for points of maximum power.

Based on the results we can verify that:

1. Temperature and pressure spatial gradients in the flow direction are important and must be accounted for fuel cell design, modeling and simulation;
2. Gas supply causes pressure drops that induce considerable power consumption that need to be taken into account in fuel cell design, becoming increasingly important as operating current increases;
3. Conceptually, the model allows for the investigation of trade-offs that determine the internal structure - the relative sizes and spacings - in fuel cell flow systems for minimum thermodynamic losses;
4. The control volumes approach eliminated the spatial dependency in the mathematical equations, therefore spatial dependence was obtained through the known position of the fuel cell internal components. Hence, solutions were obtained with a system of algebraic equations with low computational time, instead of a computational time demanding partial differential equations system with respect to space;

5. It is reasonable to state that the combination of accuracy and low computational time allow for future utilization of the models as reliable tool for PEMFC and AMFC simulation, control, design and optimization purposes.

The model was able to capture the temperature difference between the electrodes and the reactant gases even for low concentration of electrolyte and low current. The temperature measured using high performance thermistors showed good agreement with the numerical result demonstrating that the temperature is not uniform in an operating AMFC even in small current level and low electrolyte concentration.

Both models presented in this research account for temperature gradients in the flow direction and dependence on operating current. The combination of accuracy and low computational time allow for future utilization of the models as a reliable tool for PEMFC and AMFC simulation, control, design and optimization purposes.

The following research topics were not addressed by this author in this dissertation but would be important and interesting for future work:

1. Adapt the model for transient analysis of PEMFC and AMFC. The transient time would be important for transport application for example, where the external load is changing in time.

2. Improve the robustness of the numerical model considering changes in the operating parameters as pressure and temperature of the hydrogen and oxygen.

3. Use the developed mathematical model to optimizations of internal and external structure of fuel cells.

4. Adapt the developed mathematical model for fuel cell stacks.

REFERENCES

[1] M. M. Mench, C. Wang, S. T. Thynell, An introduction to fuel cells and related transport phenomena, Int. J. Trans. Phenom. 3 (2001) 151–176.

[2] P. F. Howard, C. J. Greenhill, Ballard PEM fuel cell powered ZEV bus, Society of Automotive Engineers, SAE, 1993, Paper 931817.

[3] U. Cantoni, Alternative fuels utilization in fuel cells for transportation, Society of Automotive Engineers, SAE, 1993, Paper 931816.

[4] D. Linden, Handbook of Batteries and Fuel Cells, McGraw-Hill, New York, 1984.

[5] P. Corbo, F.E. Corcione, F. Migliardini, O. Veneri, Energy management in fuel cell power trains, Energy Conversion and Management, 47 (2006) 3255-3271.

[6] B. D. McNicol, D. A. J. Rand, K. R. Williams, Fuel cells for road transportation purposes—yes or no? J. Power Sources 100 (2001) 47–59.

[7] T. Grube, B. Hohlein, R. Menzer, Assessment of fuel-cell-based passenger cars. Fuel Cells 4(3) (2004) 231–235.

[8] J. Wishart, Z. Dong, M. Secanell, Optimization of a PEM fuel cell system based on empirical data and a generalized electrochemical semi-empirical model, J. Power Sources 161 (2006)1041-1055.

[9] G. Inoue, T. Yoshimoto, Y. Matsukuma, M. Minemoto, H. Itoh, S. Tsurumaki, Numerical analysis of relative humidity distribution in polymer electrolyte fuel cell stack including cooling water, J. Power Sources 162 (2006) 81-93.

[10] J. V. C. Vargas, J. C. Ordonez, A. Bejan, Constructal flow structure for a PEM fuel cell, International Journal of heat and Mass Transfer 47 (2004) 4177–4193. [11] R.S. Jr, E. R. Gonzalez, Mathematical modeling of polymer electrolyte fuel cells, Journal of Power Sources, 147 (2005) 32–45.

[11] J. Larmine, A. Dicks, Fuel Cell Systems Explained, second ed., Wiley, 2003.

[12] A. Rowe, X. Li, Mathematical modeling of proton exchange membrane fuel cell, Journal of Power Sources 102 (2001) 82-96.

[13] Q. Wang, D. Song, T. Navessin, S. Holdcroft, Z. Liu, A mathematical model and optimization of the cathode catalyst layer structure in PEM fuel cells, Electrochimica Acta 50 (2004) 725–730.

[14] A. Ferguson, V. I. Ugursal, Fuel cell modelling for building cogeneration applications, Journal of Power Sources 137 (2004) 30–42.

[15] A. Bıyıkoglu, Reviewof proton exchange membrane fuel cell models, International Journal of Hydrogen Energy 30 (2005) 1181 – 1212.

[16] R.F. Mann, J.C. Amphlett, B.A. Peppley, C.P. Thurgood, Application of Butler–Volmer equations in the modelling of activation polarization for PEM fuel cells, Journal of Power Sources 161 (2006) 775–781.

[17] Q. Yan, J. Wub, Modeling of single catalyst particle in cathode of PEM fuel cells, Energy Conversion and Ma*nagem*ent 49 (2008) 2425–2433.

[18] J.J. Baschuk, X. Li, A comprehensive, consistent and systematic mathematical model of PEM fuel cells, Applied Energy 86 (2009) 181–193.

[19] J. Larmine, A. Dicks, Fuel Cell Systems Explained, second ed., Wiley, 2003.

[20] W. Vieslstich, A. Lamm, and H. A. Gasteiger. Handbook of Fuel Cells, vol. 2. John Wiley and Sons, New York, 2003.

[21] T. Burchardt, P. Gonerec, E. Sanchez-Cortezon, Z. Karichev, J.H. Miners, Alkaline fuel cells: contemporary advancement and limitations, Fuel 81 (2002) 2151-2155.

[22] A. Tewari, V. Sambhy, M.U. Macdonald, A. Sen, Quantification of carbon dioxide poisoning in air breathing alkaline fuel cells, J. Power Sources 153 (2006) 1-10.

[23] A. Verma, A. K. Jha and S. Basu, Manganese dioxide as a cathode catalyst for a direct alcohol or sodium borohydride fuel cell with a flowing alkaline electrolyte, Journal of Power Sources 141 (205) 30-34.

[24] M. Chatenet, F. Micoud, I. Roche and E. Chainet, Kinetic of sodium borohydride direct oxidation and oxygen reduction in sodium hydroxide electrolyte. Part I. BH_4^- electro-oxidation on Au and Ag catalysts, Electrochimica Acta 51 (2006) 5459-5467.

[25] C. Berger (Ed.). Handbook of Fuel Cells Technology. Prentice Hall, Englewood Cliffs, NJ, 1968.

[26] E. Gulzow, M. Schulze, U. Gerke, Bipolar concept for alkaline fuel cells, J. Power Sources 156 (2006)1-7.

[27] R. O'Hayre, S. Cha, W. Colella and F. Prinz, Fuel Cell Fundamentals, Second ed, Hoboken, New Jersey, 2009.

[28] D. Stoica, L. Ogier, L. Akrour, F. Alloin, J-F. Fauvarque, Anionic membrane based on polyepichlorhydrin matrix foa alkaline fuel cell: Synthesis, physical and electrochemical properties, Electrochimica Acta 53 (2007) 1596-1603.

[29] C. Sollogoub, A. Guinault, C. Bonnebat, M. Bennjima, L. Akrout, J.F. Fauvarque, L. Ogier, Formation and characterization of crosslinked membranes for alkaline fuel cells, Journal of Membrane Science, 335 (2009) 37-42.

[30] J. Park, S. Park, S. Yim, Y. Yoon, W. Lee, C. Kim, Performance of solid alkaline fuel cells employing anion-exchange membranes, Journal of Power Sources, 178 (2008) 620-626.

[31] F. Bidault, D.J.L. Breet, P.H. Middleton, N. Abson, N.P. Brandon, A new application for nickel foam in alkaline fuel cells, International Journal of Hydrogen Energy 34 (2009) 6977-6808.

[32] Y. Wan, K. A. Creber, B. Peppley, V.T. Bui , E. Halliop, New solid polymer electrolyte membranes for alkaline fuel cells, Polymer International, 54 (2005) 5-10.

[33] G. Li, P. G. Pickup, Ionic conductivity of PEMFC electrodes, J. Electrochem. Soc. 150 (11) (2003) C745-C752.

[34] D. Sangeetha, Conductivity and solvent uptake of proto exchange membrane based on polystyrene (ethylene-butylene) polystyrene triblock polymer. European Polymer Journal, 41 (11) (2005) 2644-2652.

[35] Y. Elabd, E. Napadensky, Sulfonation and characterization of poly(styrene-isobutylene-styrene) triblock copolymers at high ion-exchange capacities. Polymer, 45 (2004) 3037-3043.

[36] J. Morikawa, A. Kobayahi, T. Hashimoto, Thermal diffusivity in a binary mixture of poly (phenylene oxide) and polystyrene. Thermochimica Acta, 267 (1) (2005) 289-296.

[37] E. Gülzow, M. Schulze, G. Steinhilber and K. Bolwin, Carbon dioxide tolerance of gas diffusion electrodes for alkaline fuel cells, Proceedings of the Fuel Cell Seminar San Diego (1994), p. 319.

[38] D. Valade, F. Boschet, S. Roualdes, B. Ameduri, Preparation of solid alkaline fuel cell binders based on fluorinated poly(diallydldimethylammonium chloride)s [poly(DADMAC)] or Poly(chlorotrifluoroethylene-co-DADMAC) Copolymers, Journal of Polymer Science, 47 (2009)2043-2058.

[39] J.Varcoe, R.C.T. Slade, G.L.Wright, Y., Chen, Steady-state dc and impedance investigations of H_2/O_2 alkaline membrane fuel cells with commercial Pt/C, Ag/C, and Au/C Cathodes, Journal of Phys. Chem. B, 110 (2006)21041-21049.

[40] T. Xu, Ion exchange membranes: State of their development and perpective, Jounal of Membrane Science, 263 (2005)1-29.

[41] E. Agel, J. Bouet, J. F. Fauvarque, Characterization and use of anionic membranes for alkaline fuel cells, Journal of Power Sources, 101 (2001) 267-274.

[42] J. R. Varcoe, R. C.,Slade, Prospects for alkaline anion-exchange membranes in low temperature fuel cells, Fuel cells, 5 (2005) 187-200.

[43] B., Smitha, S. Sridhar, A.A. Khan, Solid polymer electrolyte membranes for fuel cell, Journal of Membrane Science,259 (2005) 10-26.

[44] E. Gulzow, M. Schulze, Long-term operation of AFC electrodes with CO_2 containing gases, J. Power Sources 127 (1–2) (2004) 243-251.

[45] K. Kordesch and G. Simader, Fuel Cells and their Applications, VCH-Verlag, Weinheim (1996).

[46] E. Gülzow, N. Wagner and M. Schulze, Fuel Cells **3** (2003), p. 67.

[47] W. Ostwald, Elektrische eigenschaften halbdurchlassiger schedewande, S. Phys. Chem. 6 (1890) 71.

[48] T. Nishiwaki, Concentration of electrolytes prior to evaporation with an electro-membrane process, in: R.F. Lacey, S. Loch(Eds.), Industrial Process with Membranes, Wiley-interscience, New York, 1972.

[49]J.Shin, Y. Park, H. Lee, J. Lee, Hydrogen oxidation characteristics of Raney nickel electrodes with carbon black n an alkaline fuel cell, Journal of Power Sources 74 (1998) 151-154.

[50] L.M. Appelman, W.F. ten Barge, P.G.J. Reuzel, Acute inhalation toxicity study of ammonia in rats with variable exposure periods, Am Ind Hyg Assoc J 43 (1982) 662-665.

[51] American Industrial Hygiene Association (AIHA) in: Hygienic guide series. Anhydrous ammonia, Am Ind Hyg Assoc J 32 (1971) 139-142.

[52] S. Toyokuni S, Mechanisms of asbestos-induced carcinogenesis, Nagoya J. Med. Sci. 71 (1–2) (2009) 1-10.

[53] J.V.C. Vargas, J.E.F.C. Gardolinski, J.C. Ordonez, R. Hovsapian, Alkaline Membrane Fuel Cell– Provisional Patent Application – US 61/363,689 filed on July 13, 2010.

[54] R. Souza, E.R. Gonzalez, Mathematical modeling of polymer electrolyte fuel cells, Journal of Power Sources 147 (1-2) (2005) 32-45.

[55] L.S. Martins, J.E.F.C. Gardolinski, J.V.C. Vargas, J.C. Ordonez, S.C. Amico, M.M.C. Forte, The experimental validation of a simplified PEMFC simulation model for design and optimizations purposes, Applied Thermal Engineering 29 (2009) 3036-3048.

[56] J.V.C. Vargas, A. Bejan, Thermodynamic optimization of internal structure in a fuel cell, International Journal of Energy Research 28 (2004) 319-339.

[57] J.B. Young, Thermal fluid modeling of fuel cells, Annu. Rev. Fluid Mech. 39 (2007) 193-215.

[58] L. Ma, D.B. Ingham, M. Pourkashanian, E. Carcadea, Review of the computatuional fluid dynamics modeling of fuel cells, J. Fuel Cell Sci. Technol. 2 (2005) 246-257.

[59] I. Verhaert, M. Paepe, G. Mulder, Thermodynamic model for an alkaline fuel cell Journal of Power Sources 193 (1) (2009) 233-240.

[60] M. Duerr, S. Gair, A. Cruden, J. McDonald, Dynamic electrochemical model of an alkaline fuel cell stack, Journal of Power Sources 171 (2007) 1023-1032.

[61] S. Mohan, S.O.B. Shrestha, Evaluation of the performance characteristics and modeling of an alkaline fuel cell Journal of Fuel Cell, Science and Technology 7 (4) (2010) 122-127.

[62] H. Weydahl, A.M. Svensson, S. Sundea, Transient model of an alkaline fuel cell cathode,Journal of the Electrochemical Society 156 (3) (2009) A225-A237.

[63] R. K. Shah, A. L. London, Laminar Flow Forced Convection in Ducts, Supplement 1 to Advances in Heat Transfer, Academic Press, New York, 1978.

[64] A. Bejan, Convection Heat Transfer, second ed., Wiley, 988 New York, 1995.

[65] R. B. Bird, W. E. Stewart, E. N. Lightfoot, Transport Phenomena, second ed., Wiley, New York, 2002.

[66] M. R. Tarasevich, A. Sadkowski, E. Yeager, in: B. E. Coway, J. O'M. Bockris, E. Yeager, S. U. M. Khan, R. E. White (eds.), Comprehensive Treatise of Electrochemistry, Vol. 7, Plenum, New York. 1983, 310-398.

[67] J. S. Newman, Electrochemical Systems, second ed., Prentice Hall, Englewood Cliffs, NJ, 1991, pp. 255, 299, 461.

[68] J. A. Wesselingh, P. Vonk, G. Kraaijeveld, Exploring the Maxwell–Stefan description of ion-exchange, Chem. Eng. J. Biochem. Eng. J. 57 (1995) 75–89.

[69] M. J. Moran, R. Shapiro , Fundamentals of Engineering Thermodynamics (3rd ed), 1993 Wiley: New York.

[70] W. L. Masterton, C. N. Hurley, Chemistry Principles & Reactions (3rd ed), 1997. Saunders College Publishing: Orlando, FL.

[71] T. E. Springer, T. A. Zawodzinski, S. Gottesfeld, Polymer electrolyte fuel cell model, J. Electrochem. Soc. 138 (1991) 2334-2341.

[72] A. A. Kulikovsky, J. Divisek, A. A. Kornyshev, Two-dimensional simulation of direct methanol fuel cells –a new (embedded) type of current collector, J. Electrochem. Soc. (147) (2000) 953-959.

[73] V. Gurau, F. Barbir, H. Liu, An analitical solution of a half-cell model for PEM fuel cells, J. Electrochem. Soc. 147 (2000) 2468-2477.

[74] J. O'M. Bockris, D. M. Drazic, Electro-chemical Science, Taylor and Francis, London, 1972.

[75] A. J. Bard, L. R. Faulkner, Electrochemical Methods – Fundamentals and Applications, second ed., Wiley, New York, 2001.

[76] R. Bove, S. Ubertini, Modeling solid oxide fuel cell operation: Approaches, techniques and results, J. Power Sources 159 (2006) 543-559.

[77] R. J. Gilliam, J. W. Graydon, D. W. Kirk, S. J. Thorpe, A review of specific conductivities of potassium hydroxide solutions for various concentrations and temperatures, International Journal of Hydrogen Energy 32 (2007)359-364.

[78] R. H. Perry, D. W. Green, J. O. Maloney, Perry's, Chemical Engineer's Handbook (6th ed), 1984. McGraw-Hill: New York.

[79] Schatz Energy Research Center, Operation and Maintainance Manual – SERC Single Cell Fuel Cell Kit, Humboldt State University, Arcata, CA, USA, 2004.

[80] ASTM - D792-00 Standard Test Methods for Density and Specific Gravity (Relative Density) of Plastics by Displacement, ASTM International, 2000.

[81] C. M. A. Lopes, M. I. Felisberti, Thermal conductivity of PET/ (LDOE/AI) composites determined by MDSC. Polymer Testing, 23 (2004) 637-643.

[82] D. R. Lide (Ed.), CRC Handbook of Chemistry and Physics, 83rd ed., CRC Press, Boca Raton, FL, 2002/2003.

[83] D. Kincaid, W. Cheney, Numerical Analysis Mathematics of Scientific Computing, first ed., Wadsworth, Belmont, CA, 1991.

[84] Editorial, Journal of Heat Transfer policy on reporting uncertainties in experimental measurements and results, ASME Journal of Heat Transfer, 115 (1993) 5-6.

[85] I.D. Zaytsev, G.G. Aseyev, Properties of Aquous solutions of electrolytes, CRC press, Boca Raton,Fl, 1992.

[86] LabVIEW 7 Express, 2003, User Manual, National Isntruments™, LabVIEW help, April, 320999E-01.

BIOGRAPHICAL SKETCH

Lauber de Souza Martins

Lauber Martins received his Bachelors degree in Mechanical Engineering from Universidade Federal do Parana in Brazil in 2003, with several papers published in conferences organized for undergraduate mechanical engineering students. In 2005, he received his Master in Mechanical Engineering in Thermal and Chemical Processes under the advisement of Dr. Jose Viriato Coelho Vargas.

In 2007, he started to work as Research Assistant at Center for Advanced Power Systems – Florida State University under supervision of Dr. Juan Carlos Ordonez. In 2008 he enrolled in the doctoral program at Florida State University under the advisement of Dr. Juan Carlos Ordonez in thermal management of energy systems working with mathematical modeling and simulation Polymer Electrolyte Fuel Cells and Alkaline Fuel Cells aiming the development of computational tools for optimization.

Since 2009 he has served the Mechanical Engineering Department as Teaching Assistant of Advanced Engineering Thermodynamics and Thermal Fluids I and II. On spring of 2012, he was appointed as Instructor of Mechanics and Materials I.